Spatial Reconstruction of Quantum States of Light

Charris Gabaldon

Williamsburg, Virginia

Master of Science, College of William & Mary, 2022
Bachelor of Science, California State University, 2017

A Dissertation presented to the Graduate Faculty
of The College of William & Mary in Candidacy for the Degree of
Doctor of Philosophy

Department of Physics

College of William & Mary
August 2025

APPROVAL PAGE

This Dissertation is submitted in partial fulfillment of
the requirements for the degree of

Doctor of Philosophy

Charris Gabaldon

Approved by the Committee May 2025

Committee Chair
Eugeniy E. Mikhailov, Professor, Physics
College of William & Mary

Irina Novikova, Professor, Physics
College of William & Mary

Seth Aubin, Associate Professor, Physics
College of William & Mary

Ebubechukwu Ilo-Okeke, Assistant Professor, Physics
College of William & Mary

Hwang Lee, Associate Professor, Physics
Louisiana State University

ABSTRACT

In optical measurements, quantum noise arises from inherent fluctuations in the amplitude and phase of a light field, setting a fundamental limit to detection sensitivity. Although this type of noise is unavoidable, it can be addressed by engineering special quantum states known as quadrature-squeezed states. These states allow noise to be reduced in either the amplitude or phase quadrature, although this comes at the cost of increased noise in the conjugate parameter.

Using a generalized reconstruction method, it is possible to separate the squeezed modes through their unique squeezing parameters, even when these modes are spatially overlapped. This study discusses noise tolerance in realistic measurement environments and determines the resolution limits for extracting squeezed state parameters. The framework developed here may be used across a range of applications, including quantum-enhanced metrology for improved precision and imaging techniques.

TABLE OF CONTENTS

ACKNOWLEDGMENTS

Dedicated to

LIST OF FIGURES

SPATIAL RECONSTRUCTION OF QUANTUM STATES OF LIGHT

CHAPTER 1

Introduction

1.1 Noise Sources

In experimental setups, both classical and quantum noise sources introduce uncertainties that affect measurement precision. These phenomena represent significant challenges in achieving accurate results, necessitating a thorough understanding of their origins and mitigation strategies.

Classical noise arises from environmental and technical factors inherent to the experimental apparatus. Common examples include apparatus vibrations, laser frequency drifting, thermal drifts, and laser intensity fluctuations. Such disturbances often stem from external mechanical oscillations, temperature variations, or instability in laser output. To address these issues, researchers employ suppression techniques such as locking systems, which stabilize components by actively compensating for detected deviations. While these methods effectively reduce classical noise, they cannot eliminate uncertainty entirely due to the presence of intrinsic quantum effects.

The principle of quantum effect establishes a lower bound on the uncertainty between

two conjugate variables, expressed as $\Delta q \Delta p \geq \frac{\hbar}{2}$ [3]. This is known as Heisenberg's uncertainty principle. Here, q (position) and p (momentum) exemplify conjugate pairs, though in optical contexts, quadratures q and p often serve as the relevant quadrature variables in phase space. For a coherent state (a quantum state of which there is a close classical approximation) the uncertainties in these conjugate quantities are equal. However, advancements in quantum optics enable the creation of squeezed states, where one variable's uncertainty is reduced below the standard quantum limit.

Squeezed states represent a pivotal innovation for precision measurements, particularly in fields like gravitational wave detection and quantum communication. By redistributing uncertainty between conjugate variables, these states "squeeze" noise out of a desired parameter, enhancing sensitivity in specific measurements.

In this work, we systematically characterize individual squeezed modes by their distinct squeezing parameters, which allows us to precisely determine the spatial structure associated with each mode. We review the squeezing parameter and its significance in quantum state characterization, as well as the historical development of the analytical tools and decomposition techniques used to uncover the spatial structure of these modes.

1.2 History of Squeezing

Although classical methods can solve many optics experimental challenges, there is a fundamental noise limit from the photons of laser light that cannot be further reduced. This is called the shot noise, or the lowest noise floor limit classical techniques can reach as lasers follow Poissonian statistics [4]. Squeezed light states, by definition, have one quadrature measurement with noise levels below shot noise.

The uncertainty principle was formulated in 1927 when Heisenberg introduced matrix mechanics, revealing that measuring a particle's position inevitably disturbs its momen-

tum, and vice versa [5]. However, since the field of modern optics only emerged in the 1960's with the advent of the laser, it took several decades before the terminology and foundational concepts commonly used today became established.

In 1963, Glauber introduced coherent states (laser-like states) as minimum uncertainty product states for quadratures. These states saturate the uncertainty inequality, with equal variances in both quadratures. Glauber's coherence theory formalized quadrature-phase measurements [6]. Coherent states were also independently developed by Klauder in 1960 (as over-complete basis states) and Sudarshan in 1963 (who linked classical and quantum descriptions) [7, 8, 9].

The 1970's saw the invention of the tunable laser and through the theoretical study of photon statistics by Walls et al., Carmichael et al., Cohen-Tannoudji et al., Mandel and Kimble, the foundation of non-classical light was laid [9, 10, 11].

Squeezed states of the optical field were first proposed theoretically by Stoler et al. in 1970 [12, 13]. However, the field of quantum nonlinear optics began with the work of Burnham et al. and Weinberg et al. in 1970 [14]. Up until the 1980's, nearly all studied light fields exhibited phase-independent noise. This situation changed with the advent of squeezed light sources, which possess phase-sensitive noise characteristics. The development of these sources made it possible to explore the Heisenberg uncertainty relations in optical fields [9]. The 1970's and 1980's witnessed groundbreaking theoretical progress in squeezed-state research. Yuen et al. pioneered methods for producing two-photon coherent states via four-wave mixing in 1979 [15]. Subsequent work by Caves et al. revealed how squeezed light could reduce quantum noise in interferometers, while Walls later compiled a seminal review synthesizing these advancements [16, 17, 18].

Experimental demonstrations and results began to emerge in the 1980's. In 1987 Slusher et al. produced squeezed states via four-wave mixing in a cavity [19], while Shelby achieved similar results using optical fibers in 1986 [20]. Wu et al. recorded significant early

squeezing levels (-4 dB below shot noise) through an optical parametric oscillator (OPO) system in 1987 [21]. Pereira et al., who came from the same group as Wu, demonstrated enhanced interferometric performance with squeezed states a year later [18, 22].

Squeezing methods involving atomic material also came about in the 1980's, with Slusher et al. implementing 4WM in sodium [23]. Subsequent decades witnessed continued progress [24, 25, 26, 27], culminating in record squeezing levels reaching $-15\ dB$ below shot noise using an OPO driven system [28]. McCormick et al. and Lett extended the 4WM squeezing approach to rubidium vapors in 2007 and 2008, respectively [29, 30].

Polarization self-rotation (PSR) emerged as a significant nonlinear optical phenomenon to produce squeezing through foundational work by Novikova, Matsko, and colleagues [31, 32, 33, 34, 35]. Their early studies established that elliptically polarized light propagating through resonant atomic media undergoes polarization ellipse rotation due to differential AC Stark shifts between circular polarization components, without requiring external magnetic fields. This effect was linked to quantum noise suppression, with their 2002 model predicting vacuum squeezing via cross-phase modulation between pump and vacuum fields [34]. Practical implementations required accounting for atomic hyperfine structure and ground-state decoherence such as mitigating noise in hot Rb vapors by tuning laser detuning and power [36].

The framework expanded to ultracold atomic systems, where Horrom et al. observed PSR-Faraday rotation interplay in rubidium, showing how residual magnetic fields modify ellipticity-dependent rotation angles in 2011 [37]. These studies validated Novikova and Matsko's predictions while highlighting system-specific constraints. Their collective work remains pivotal for quantum metrology applications, particularly in developing squeezed-light sources via atomic nonlinearities.

In magnetometry, Horrom et al. demonstrated enhanced sensitivity by generating squeezed light via polarization self-rotation in rubidium vapor [38]. Kong et al. optimized

this approach using polarization-squeezed light resonant with the Rb D1 line, suppressing photon shot noise by 2 dB and improving high-frequency sensitivity without degrading low-frequency performance [39, 40]. For absorption measurements, Marino developed on-resonance two-mode squeezed states via four-wave mixing in Rb vapor, enabling efficient atomic interactions through feedforward techniques that transferred squeezing to single-mode configurations [41]. The most impactful application lies in gravitational wave detection, where LIGO's implementation of squeezed vacuum states reduced quantum noise by manipulating vacuum fluctuations, achieving record sensitivity above 200 Hz and validating compatibility with large-scale interferometer operations [42, 43].

More recently, Zhao et al. and Yu et al. from East China Normal University experimentally produced 4.3 dB of squeezing via polarization self-rotation (PSR) [44], the same squeezing process we use in this work. Using an additional magnetic field and an artificial intelligence optimization scheme, they improved their total squeezing which originally was 1.5 dB [45]. PSR will further be discussed in Sec. 5.1 as that is also the squeezing mechanism we use in this work.

Past efforts of this work include spatially tailoring multimode Gaussian squeezing to mode-match with a reference beam, or local oscillator [46, 47]. As PSR produces squeezing without any prior information of what type of modes or how many are present, we have a large search space to go through. Even without full mode-matching schemes, the mixed mode squeezed light has been demonstrated to improve the detection sensitivity of an atomic magnetometer [48].

As we have so thoroughly discussed squeezed light, which is characterized by its squeezing parameter, we are additionally interested in the spatial mode shape of individual squeezed light modes, which calls for specialized decomposition methods, which we discuss next.

1.3 Decompositions

The spatial shape of squeezed modes are considered Gaussian in nature and maintain certain characteristics as they propagate, mix, and are detected [49]. The relationship between Gaussian modes and Singular Value Decomposition (SVD) arises in contexts where systems exhibit Gaussian behavior or noise, and SVD provides a mathematical framework to analyze their structure, or decompose multimode Gaussian systems into individual modes.

Singular Value Decomposition (SVD) is a foundational matrix factorization technique commonly used in physics, offering insights into complex systems by distilling data into interpretable components. At its core, SVD decomposes any m by n matrix, A, into three matrices: W (left singular vectors), Σ (diagonal singular values), and V (right singular vectors), such that $A = W\Sigma V$. This decomposition is unique up to the ordering of singular values, which are non-negative and hierarchically arranged, reflecting the relative significance of each component. Furthermore, if A is real with a positive determinant, W and V are real orthogonal matrices [50].

Singular Value Decomposition (SVD) is a general-purpose matrix factorization tool, but Williamson and Bloch-Messiah Decompositions are specialized for symplectic matrices in physics, preserving critical structures in classical and quantum Hamiltonian systems. Thus, we utilize the more specific decomposition processes in Sec. 4.2. Symplectic matrices preserve linear transformations the fields experience as they propagate through common optical elements.

1.3.1 Williamson Decomposition

In 1936, John Williamson demonstrated that any positive-definite symmetric matrix can be diagonalized via some symplectic matrix so long as the initial matrix is real and even

in size [51]. Today this method is an important factorization tool in continuous variable (CV) quantum optics and has found uses in pure state decompositions and mixed Gaussian states, which are of particular interest for our purposes [52]. As discussed in Sec. 4.2 we use Williamson Decomposition as an initial factorization process to obtain a symmetric matrix that maintains the physical meaning of thermal modes present in the system, which next feeds into another decomposition process, Bloch-Messiah Decomposition, which is discussed below.

1.3.2 Bloch Messiah Decomposition

In Section 4.2 we utilize a special singular value (SVD) decomposition form to break down experimental measurements into more meaningful physical components. This is known as Bloch-Messiah Decomposition, named after C. Bloch and A. Messiah [53]. The two physicists initially developed a similar method for fermions in 1962 that was later modified for bosons by Braunstein, who introduced the name 'Bloch-Messiah' [54]. Bloch-Messiah follows a similar recipe as it linearly rotates (O_1), nonlinearly squeezes (Z), then linearly rotates (O_2) a square matrix. The Bloch-Messiah Decomposition has been described as "nothing but the singular value decomposition of a symplectic matrix" by Serafini in 2017 [50]. This reduction process essentially utilized SVD on the resulting matrices from the Bogoliubov transformation, assuming we started with a Gaussian unitary, U [55].

As of 2018, this method has been applied to broadband squeezed light to decompose multimode systems into individual squeezed modes [56] and initial attempts to generalize to multimode squeezing have been ongoing [57] as researchers continue to refine its implementations in quantum optics.

Overall, Bloch-Messiah Decomposition reduces continuous variable quantum information (or more specifically, complex Gaussian unitary operators, U) into its irreducible

sources by identifying input and output modes of optical squeezers [52]. This is conveniently what we are aiming to achieve.

CHAPTER 2

Gaussian States

Gaussian quantum states hold fundamental importance in quantum optics as they are preserved under all processes generated by Hamiltonians, up through the second-order, or lower in the field operators. This includes operations such as linear optics and quadrature squeezing. An effective way to analyze and calculate properties of these states is through the use of phase-space variables and symplectic transformations. By employing phase-space methods, we can identify the symplectic transformations associated with commonly used optical operations, such as displacements, beam splitters, and squeezing. These methods also provide systematic procedures for tracing out modes, handling homodyne measurements, and determining squeezing parameters in experimental settings [50].

2.1 Classical Electric Field

The classical electric field equation can be approximated as a monochromatic plane wave as follows:

$$\vec{E}(\vec{r},t) = \vec{\mathcal{E}}_x e^{i\phi_x}\hat{x} + \vec{\mathcal{E}}_y e^{i\phi_y}\hat{y} \tag{2.1}$$

where the plane moves along $\hat{z}$ and is shown in its spatial linear components $\hat{x}$ and $\hat{y}$. The electric field at any point can be described as the sum of two perpendicular components, each oscillating independently in the transverse plane. The amplitudes $\mathcal{E}_x$ and $\mathcal{E}_y$, along with their respective phases ϕ_x and ϕ_y, completely characterize the orientation and temporal evolution of the electric field vector. The relative magnitudes and phases of these orthogonal components determine the way the electric field vector traces out a path in the plane perpendicular to the direction of propagation, or describes the polarization of the field.

2.2 Polarization

Natural light sources emit unpolarized light because their transverse electromagnetic waves propagate with equal probability across all oscillation planes. Polarization refers to the orientation of the electric field's (Eq. 2.1) oscillations within these waves. In a laboratory setting, it is possible to manipulate a light source to produce specific polarization states. For instance, if light consists of one plane wave, we call this linearly polarized light (Fig. 2.1a). If light consists of two plane waves with equal amplitude and a phase difference of 90°, the resulting light is circularly polarized (Fig. 2.1b). On the other hand, if the two waves have unequal amplitudes and are still separated by a 90° phase difference, or if the phase difference is any angle other than 90°, the light becomes elliptically polarized (Fig. 2.1c). This ability to control polarization is essential for various experimental and practical applications, including our work.

Linearly polarized light can be decomposed into right-handed circularly (RHC) polarized components and left-handed circularly (LHC) polarized components, of equal strength and is described as

$$E_{linear} = E_{RHC} + E_{LHC} \tag{2.2}$$

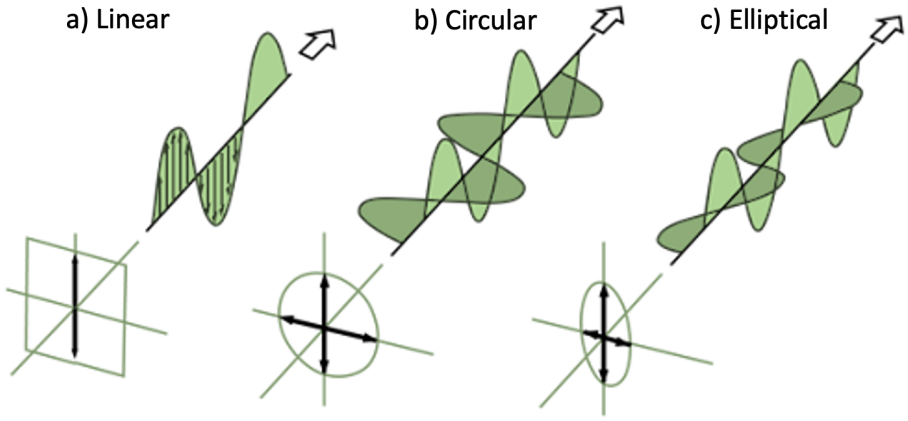

FIG. 2.1: Types of light polarizations a) Linearly polarized light b) Circularly polarized light c) Elliptically polarized light. *Adapted from "Hyperphysics," by C. R. Nave, 1998, hyperphysics.phy-astr.gsu.edu. Accessed 6 Sept 2024.*

where RHC (LHC) polarized light has the same amplitude of the electric field (E_{linear}), or constant magnitude but with some (counter)clockwise rotation of the electric field vector $\phi_{RHC(LHC)}$. Maintaining clean linear polarization is a key experimental requirement for our method of squeezing production.

2.3 Quantization of the Electric Field

As we will soon see, working in phase space (instead of 3D human space) enables a strong visualization and intuition about the states of light (Sec. 2.8) we are interested in. Phase space combines ordinary space and momentum space, forming a six-dimensional space where the state of a particle can be described. [58, 59]. Classical physics allows for the exact determination of a particle's spatial position and momentum, enabling its state to be depicted as a point in the phase space. However, we do not have the luxury of certainty as we move into the quantum realm. To expand the classical point measurement, we first must quantize the electric field while maintaining the Gaussian state form.

The quantized Hamiltonian, ($\mathcal{H}$), of the electromagnetic field can be described as:

$$\mathcal{H} = \hbar\omega \left(\hat{a}^\dagger \hat{a} + \frac{1}{2} \right) \tag{2.3}$$

where $\hbar$ is the reduced Planck constant, $\hat{a}^\dagger$ is the creation operator, and $\hat{a}$ is the annihilation operator [9]. The creation operator adds a photon to the system while the annihilation operator removes a photon. The operators hold bosonic commutation relationships as $[\hat{a}^\dagger, \hat{a}] = 1$ [60].

We next introduce the number state $\hat{n}$ to represent a quantum state of light with a precisely defined number of photons. Number states are fundamental in quantum mechanics, providing a particle-like description of electromagnetic fields and satisfy

$$N \left| n \right\rangle = n \left| n \right\rangle , \ n \in \{0, 1, 2, \ldots\} \tag{2.4}$$

where $N = \hat{a}^\dagger \hat{a}$ is the number operator and n is the photon count [9]. Note, number states do not have any uncertainty in their photon count.

Creation and annihilation operators can be applied to a number state as

$$\hat{a}^\dagger |n\rangle = \sqrt{n+1} \, |n+1\rangle \tag{2.5a}$$

$$\hat{a} |n\rangle = \sqrt{n} \, |n-1\rangle. \tag{2.5b}$$

As the Hamiltonian describes the total energy of the system, and $|n\rangle$ is an energy eigenstate of a single state we see

$$\hat{H}|n\rangle = \frac{1}{2}\hbar\omega(\hat{a}^\dagger \hat{a})|n\rangle = E_n|n\rangle, \tag{2.6a}$$

$$E_n = \hbar\omega(n + \frac{1}{2}), n \in \mathbb{Z}^+ \tag{2.6b}$$

where the lowest energy, or vacuum, is described as $n = 0$ such that $E_0 = \frac{\hbar\omega}{2}$. In this text, we focus on vacuum states, or the lowest-energy configuration of a quantized electromagnetic field, characterized by the absence of photons and normalize the lowest energy to 1, $E_0 \approx 1$ for convenience. Further details are provided in Sec. 2.8. Later on, we use this lowest energy to physically verify our reconstruction results.

2.4 Quadrature Basis

Similarly to position and momentum operators, we define new quadratures in phase space, $\hat{q}$ and $\hat{p}$, as

$$\hat{q} = (\hat{a}^\dagger + \hat{a}), \tag{2.7a}$$

$$\hat{p} = i(\hat{a}^\dagger - \hat{a}). \tag{2.7b}$$

Quadrature operator q is the real part of the electric field and operator p is the imaginary component of the field [4].

We introduce an operation transformation matrix from the creation and annihilation operators to quadratures as

$$\begin{pmatrix} q \\ p \end{pmatrix} = Q \begin{pmatrix} \hat{a}^\dagger \\ \hat{a} \end{pmatrix} \tag{2.8a}$$

$$\begin{pmatrix} q \\ p \end{pmatrix} = \frac{1}{\sqrt{2}} \begin{pmatrix} 1 & 1 \\ i & -i \end{pmatrix} \begin{pmatrix} \hat{a}^\dagger \\ \hat{a} \end{pmatrix} \tag{2.8b}$$

where a $\frac{1}{\sqrt{2}}$ normalization factor is inserted in our definition of Q as basis transformations are unitary, or physically reversible.

Quadratures q and p commute as $[\hat{q}, \hat{p}] = 2i$ such that they can never yield zero, and

thus the Heisenberg Uncertainty Principle arises fundamentally from this non-commutativity. Explicitly, the uncertainty principle claims

$$\left\langle (\Delta\hat{q})^2 \right\rangle \left\langle (\Delta\hat{p})^2 \right\rangle \geq 1 \tag{2.9}$$

where the product of each quadrature's variance cannot be further reduced [9, 4]. Thus there is a minimum amount of noise that will always exist in the field, intrinsic to the quantum characteristics of light. Eq. 2.9 is often called the standard quantum limit (SQL) when the quadratures' product of uncertainty is at its lowest, 1. The SQL is a highly critical point as it is a fundamental boundary in precision measurements imposed by quantum mechanics. Without employing techniques, such as producing squeezed light, this limit defines the minimum level of quantum noise achievable.

2.5 Wigner Function

Wigner distributions were first introduced by Eugene Wigner in 1932 [61]. Every Gaussian state has a Gaussian Wigner function, or a quasi-probability density function which yields all mode information. "Quasi" simply indicates that it is possible for the distributions to include negative values, or that they are non-classical [60]. However, for linear canonical transformations, the Wigner function exhibits precisely the same behavior as a classical probability distribution in phase space and is thus only positive [62].

The Wigner function aims to tie the wavefunction from Schrödinger's equation to a probability distribution in phase space and fully describes the physical mode(s) present in the system. From the experimentalists' point of view, the Wigner function acts as a visualization aid for the complex mode structure as our view of the mode in phase space is just a projection, or segment, of the Wigner function [4]. In short, if we know the Wigner

function, we have all the mode information needed.

2.5.1 Wigner Function of a Gaussian State

Although a general description, the Wigner function can be simplified for Gaussian states and shares many properties with a classical Gaussian distribution, such as being positive everywhere and having a form that is symmetric in phase space. This point is highly critical as it permits all classical Gaussian calculations to remain true, even as we quantize the system. The Gaussian Wigner function is defined as:

$$W(q,p) = \frac{1}{(2\pi)^N \sqrt{det\Sigma}} \exp\left[-\frac{1}{2}(\hat{q} - \langle\hat{q}\rangle)^T \Sigma^{-1} (\hat{p} - \langle\hat{p}\rangle)\right] \tag{2.10}$$

where N is the number of modes in the system, $\langle\rangle$ is the phase space mean, and Σ is the covariance for the desired spatial modes [60, 63, 64, 65].

2.6 Measurement Tool: Covariance Matrix

Decomposing quantum multimodes into individual single states first requires the use of the covariance matrix summarizes the statistical properties as it permits us to compare quadrature variance measurements and determine which are correlated with each other.

The concept of a covariance is simply a statistical tool that generalizes the concept of variances and means. The diagonal elements of the matrix represent the variances of individual variables ($v = \sigma^2$), while the off-diagonal elements represent covariances between pairs of variables (v_j,v_k). If the correlation of two independent variables is non-zero, there is some relationship between the variables. In our case, these variables are the q and p quadrature variances per measurement.

Recall we need the first two moments of the Gaussian state (mean and variance) to

fully describe its Wigner function (Eq.2.10). However, as we are working with a squeezed vacuum, the mean is zero which just leaves the variance.

To understand how the covariance matrix is built up, we first start by defining the expectation value. The first probability moment is known as the expectation value, or weighted mean, defined as $\mathbb{E} = \langle q \rangle = \int \int qP(q,p)\, dq\, dp$ for our quadrature q.

This feeds directly into the second statistical moment, variance (v), which measures the averaged squared difference from the mean. Variance is defined as $v(q) = \mathbb{E}(q^2) - (\mathbb{E}(q))^2$ for quadrature q. Experimentally, we make variance measurements under specialized conditions, discussed in Sec. 5.4.

The covariance of quadratures q and p is defined as the average of the products of the deviations of each quadrature from its mean, which is zero in our case and is described as

$$\Sigma(q,p) = \iint qpP(q,p)dqdp. \tag{2.11}$$

The covariance takes the experimental form

$$\Sigma_{jk} = \frac{1}{2}\left\langle \left\{ (\hat{x}_j - \langle \hat{x} \rangle_j), (\hat{x}_k - \langle \hat{x} \rangle_k) \right\} \right\rangle, \tag{2.12}$$

for the j^{th} row and k^{th} column of the covariance matrix where $\hat{x} = (\hat{q}_1, \hat{p}_1, ...\hat{q}_n, \hat{p}_n)$ represents the quadrature operators [65]. Taking into account the mean of our measurements

are zero, we see the covariance explicitly as

$$\Sigma = \begin{pmatrix} v(q_1) & c(q_1,p_1) & c(q_1,q_2) & c(q_1,p_2) & \dots & c(q_1,q_n) & c(q_1,p_n) \\ c(p_1,q_1) & v(p_1) & c(p_1,q_2) & c(p_1,p_2) & \dots & c(p_1,q_n) & c(p_1,p_n) \\ c(q_2,q_1) & c(q_2,p_1) & v(q_2) & c(q_2,p_2) & \dots & c(q_2,q_n) & c(q_2,p_n) \\ c(p_2,q_1) & c(p_2,p_1) & c(p_2,q_2) & v(p_2) & \dots & c(p_2,q_n) & c(p_2,p_n) \\ \vdots & \vdots & \vdots & \vdots & \ddots & \vdots & \vdots \\ c(q_n,q_1) & c(q_n,p_1) & c(q_n,q_2) & c(q_n,p_2) & \dots & v(q_n) & c(q_n,p_n) \\ c(p_n,q_1) & c(p_n,p_1) & c(p_n,q_2) & c(p_n,p_2) & \dots & c(p_n,q_n) & v(p_n) \end{pmatrix} \tag{2.13}$$

for n modes. Each c off diagonal element takes the general form

$$2c(a,b) = v(a+b) - v(a) - v(b) \tag{2.14}$$

for arbitrary variables a and b. Note the order of the covariance matrix is equally valid for a reshuffling of the quadratures such as $\hat{x} = (\hat{q}_1, \hat{q}_2, \dots, \hat{q}_n, \hat{p}_1, \hat{p}_2, \dots, \hat{p}_n)$.

As our goal is to separate out all independent modes from one another, we anticipate all off-diagonal covariance elements (c) to be zero as there should be no correlation between q and p quadratures of different measurements. However, this is not the case as any propagation features that the system may have undergone as we will discuss in Sec. 2.10.

Should the mode not have undergone any propagation transformations, as has been our assumption thus far, the determinant of the variance and covariance are equivalent as the covariance can be written as $\Sigma = \begin{pmatrix} v(q_1) & 0 \\ 0 & v(p_1) \end{pmatrix}$ for one mode. Otherwise, the general covariance of a single mode needs to be used, $\Sigma = \begin{pmatrix} v(q_1) & c(q_1,p_1) \\ c(q_1,p_1) & v(p_1) \end{pmatrix}$. We will return to this formalism through a few examples in Ch. 3.

A key takeaway from this description is that there are only two unknown variables, the mean and variance (v). These are also known as the first and second statistical moments of the Gaussian state, respectively. Thus if the first two moments of the Gaussian distribution are known, the Wigner function is known, and all information about the states is known. This text focuses on the second Gaussian moment, variance.

2.7 Noiseball

The noiseball, or "ball of uncertainty" as Scully calls it [66], is the cross-section of the Wigner function. The noiseball is limited in function, but provides a helpful visual of several specialized states. Quadratures relate to electric field amplitude ($|d|$), often referred to as the "stick" of the noiseball and field phase (θ) as shown in Fig. 2.2.

Several examples are shown in Fig. 2.2. In Fig. 2.2a, a noiseball of a thermal state is shown in orange, a noiseball of a vacuum state is shown in black, and a noiseball of a squeezed state is shown in blue. Thermal states are statistical mixtures of number states and will be further discussed in Subsec. 2.8.4

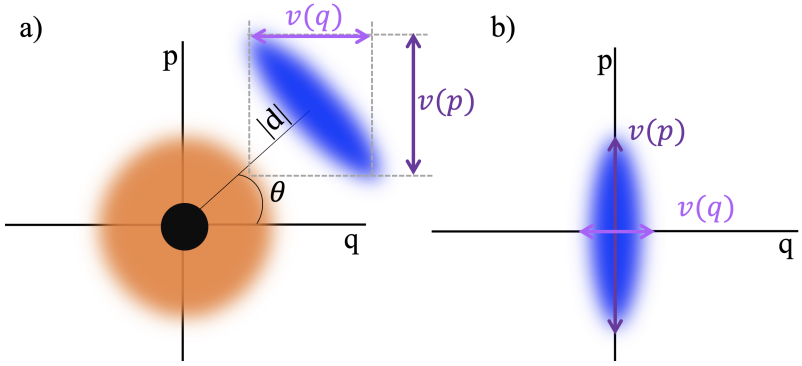

FIG. 2.2: a) A single thermal noiseball (orange), a single vacuum noiseball (black), and a squeezed noiseball (blue) projected in phase space onto quadratures q and p. $|d|$ is the displacement (i.e. amplitude) of the squeezed mode. θ is the noiseball rotation angle compared to the quadrature q axis (i.e. phase of the electromagnetic wave). b) A squeezed vacuum mode projected onto quadratures q and p with a smaller q quadrature projection, or variance ($v(q)$) than p variance ($v(p)$).

The vacuum state is centered at the origin and has equal length, or projection, across quadratures q and p. q can be approximated as the real portion of the electric field while p is approximated to be the imaginary portion of the electric field. The thermal state has a similar symmetry to the vacuum state, but is much larger in diameter. We see a non-circular shape in the squeezed state's noiseball, which could be described as a 'squished' or 'pulled' version of a coherent state (which will be discussed in Subsec. 2.8.1). In our setup, the squeezed state is still centered at the origin, as is thus a squeezed vacuum state as shown in Fig. 2.2b. For convenience, the squeezed state is initially shown with some displacement ($|d|$) in Fig. 2.2a. Note the difference in length of the cross-sections of $v(q)$ and $v(p)$ for the squeezed noiseball, a defining feature that permits us to go below shot noise limits under certain circumstances.

2.8 Types of Gaussian States

2.8.1 Coherent Spatial Mode

Optics commonly uses an approximation of real light states, including coherent states which are eigenstates of the annihilation operator [9]. Coherent states ($|\alpha\rangle$) refer to specific quantum states of light that classical oscillations most closely resemble as they have a well-defined amplitude and phase relation. In fact, Gerry and Knight call coherent modes "the 'most classical' quantum states of a harmonic oscillator" [9]. This is shortly summarized to indicate a coherent mode's electric field expectation value (Sec. 2.6) has a classical form and fluctuations are the same as a vacuum state (Subsec. 2.8.2).

Thus we note $\hat{a}\,|\alpha\rangle = \alpha\,|\alpha\rangle$. We recall states $|n\rangle$ from Eq.2.6a, as they form a complete set, and following the procedure outlined by Gerry and Knight [9], define coherent states as

$$|\alpha\rangle = \exp\left(-\frac{1}{2}|\alpha|^2\right)\sum_{n=0}^{\infty}\frac{\alpha^n}{\sqrt{n!}}|n\rangle \tag{2.15}$$

where quadrature measurements of the coherent state are equal to the classical shot noise limit. The coherent state is shown to be at the origin in Fig. 2.2a, and is a special case known as a vacuum state where the average photon number is zero. We will discuss vacuum states in the next section. Coherent states are created by applying the displacement operator, **D**, onto a vacuum state.

$$\mathbf{D}(\alpha) = exp(\alpha\hat{a}^\dagger - \alpha^*\hat{a}) \tag{2.16}$$

where $|\alpha\rangle = \hat{D}(\alpha)|0\rangle$ yields a coherent state. The distance (d) or displacement of a state from the origin is shown in Fig. 2.2a's squeezed noiseball as an example.

2.8.2 Vacuum State

Vacuum states ($|0\rangle$) are coherent as they maintain the coherent state properties. By definition, vacuum sits at the quadrature origin, which is not a requirement of coherent states in general, but permits the simplest covariance form:

$$\Sigma_{vac} = I = \begin{pmatrix} 1 & 0 \\ 0 & 1 \end{pmatrix} \tag{2.17}$$

for a single vacuum state. Should the average photon count in the system yield zero, we still expect a diagonalized covariance.

The vacuum state has the lowest possible energy level that a quantum mechanical physical system may have, permitting the quantum nature of light to become relevant. Quantum fluctuations, or vacuum fluctuations, are temporary random changes in the

amount of energy at a point in space, as dictated by Heisenberg's uncertainty principle [9]. These fluctuations mean that pairs of virtual particles are continually created and annihilated, even in "empty" space. While these particles are not directly detectable, their cumulative effects are observable.

This work primarily focuses on measuring these fluctuations, which we visualize with the noiseball of the state, as shown in Fig. 2.2.

2.8.3 Squeezed Vacuum State

Coherent states have equal uncertainty in orthogonal cross-section projections, however, this relationship does not always hold. It is possible to have a state with one quadrature with less noise than the shot noise limit by depressing the fluctuations in one quadrature such that $\langle (q)^2 \rangle \neq \langle (p)^2 \rangle$ but Eq. 2.9 still remains true and a squeezed state is produced.

A squeezed state is generated by the squeezing operator ($\mathbf{S}$)

$$\mathbf{S}(\xi) = \exp \frac{1}{2} \left(\xi^* \hat{a}^2 - \hat{a}^{\dagger 2} \right) \tag{2.18}$$

where we again see the creation (Eq.2.5a) and annihilation (Eq.2.5b) operators and ξ is

$$\xi = re^{i\theta} \tag{2.19}$$

where r is squeezing parameter which determines the degree of squeezing, and θ is the squeezing angle. The squeezing operator acting on a vacuum state yields

$$|0, \xi\rangle = S(\xi)|0\rangle \tag{2.20}$$

compared to the squeezing operator acting on a displaced vacuum state, or coherent state,

$$|\alpha, \xi\rangle = D(\alpha)S(\xi)|0\rangle \tag{2.21}$$

which yields a state where $|\alpha|$ is the amplitude and the elliptical uncertainty represents the noise in the amplitude and phase of the squeezed state.

The average photon count of the squeezed state is expressed as

$$\langle \alpha, \xi|\hat{n}|\alpha, \xi\rangle = |\alpha|^2 + \sinh^2(r) \tag{2.22}$$

when the field phase is set to $\theta = 0$ for convenience [18]. Note the hyperbolic $sinh(r)$ function is proportional to $e^r - e^{-r}$ where e^{-r} corresponds to q quadrature fluctuations and e^r corresponds to p quadrature fluctuations [18].

Should there be only one single squeezed mode in the system, the expected covariance takes the form

$$\Sigma_{sqz} = \begin{pmatrix} e^r \cos^2\theta + e^{-r}\sin^2\theta & 0 \\ 0 & e^r \sin^2\theta + e^{-r}\cos^2\theta, \end{pmatrix} \tag{2.23}$$

where r and θ are the squeezing parameter and squeezing angle, respectively [65].

2.8.4 Thermal State

We next consider thermal states as they can contaminate the squeezed states we are interested in. Thermal states are noisier than shot noise, or the noise limit, as they are a statistical mixture of number states. Thermal states are one of the most common states encountered in experiments involving light at finite temperatures. Thus, it is highly likely our system contains thermal states. Due to thermal states' increased noise, any

quantum fluctuations are overshadowed. Thermal modes maintain equal uncertainty in all projection measurements, but they lack the phase stability of coherent modes as they emit photons with random phases and amplitudes [67].

As a quantum mechanical mixed state, the thermal state can be expressed as a summation across all possible photon-number states, weighted with their occurrence probability:

$P(n)$ can be explicitly expressed as

$$P_n = \langle n|\hat{\rho}_{\mathrm{Th}}|n\rangle = \frac{\exp(-\hbar\omega/2k_BT)}{1-\exp(-\hbar\omega/k_BT)}\exp(-E_n/k_BT). \tag{2.24}$$

where k_B is the Boltzmann constant, T is the average kinetic energy of the mode's particles, ω is angular frequency, $P(n)$ is the probability of finding n photons in the i^{th} mode of the thermal state and ρ is the density matrix operator, which we do not cover in this work but is thoroughly covered in various quantum optics and mechanics textbooks [9, 3, 68].

From here we can find the average photon number of a thermal mode as

$$\bar{n} = \langle\hat{n}\rangle = Tr(\hat{n}\rho_{th}) = \frac{1}{\exp\left(\frac{\hbar\omega}{k_BT}\right)-1}. \tag{2.25}$$

Here we see the photon energy of $\hbar\omega$ along with the thermal energy components of k_BT. If the average photon number of a thermal state is zero, we are returned to a vacuum state, similarly to a coherent state without displacement.

The variance of a thermal state is generally described as

$$\langle(\Delta n_{th})^2\rangle = \langle\hat{n}^2\rangle + \langle\hat{n}\rangle^2 \tag{2.26}$$

where the fluctuations of $\hat{n}$ are larger than the average $\bar{n}$ [9, 69]. Thermal modes are indistinguishable from one another (see Subsec. 3.1) such that we can claim the covariance

matrix of a single thermal state is:

$$\Sigma_{th} = (2\bar{n} + 1)I = \begin{pmatrix} 2n_{th} + 1 & 0 \\ 0 & 2n_{th} + 1 \end{pmatrix} \tag{2.27}$$

where I is the identity matrix [70]. It should become apparent that even when there is an absence of photons, or $\bar{n} = 0$, the covariance matrix with the presence of thermal modes cannot be less than 1 as a thermal state covariance matrix is simply the addition of $2n_{th,k}$ to all diagonal terms of a vacuum state [65].

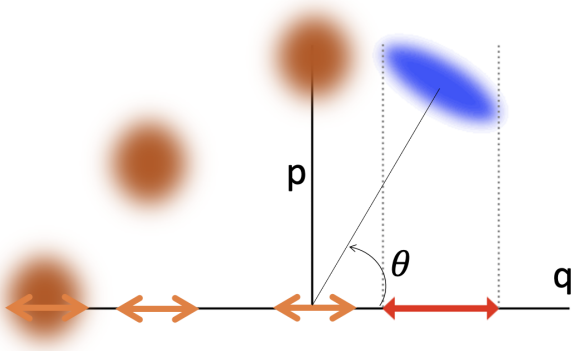

FIG. 2.3: In phase space thermal noiseballs' (orange) projection measurements are noted with orange arrows, compared to a squeezed noiseball's (blue) projection measurement shown with a red arrow.

Examples of thermal states' projections are shown in Fig. 2.3. Thermal noiseballs (orange) are shown at various rotation angles (θ), but regardless of the rotation, the projections (orange arrows) are the same. In contrast, a squeezed noiseball (blue) is shown with a projection measurement (red arrow) at some rotation angle. Note that the rotation of the squeezed noiseball will change the projection measurement, unlike with the thermal noiseball.

2.9 Gaussian State Covariances

Now that we have discussed Gaussian states of interest, the Wigner function, and first two moments, below are the results of several single states' first and second moments [70].

Gaussian Mode	Covariance	Displacement
vacuum	$\Sigma = I$	$d = (0, 0)$
thermal	$\Sigma = I(2n_{th} + 1)$	$d = (0, 0)$
coherent	$\Sigma = I$	$d = \sqrt{2}(Re(d), Im(d))$
squeezed vacuum	$\Sigma = \begin{bmatrix} e^{-r} & 0 \\ 0 & e^{r} \end{bmatrix}$	$d = (0, 0)$

The coherent state is a vacuum state displaced by d, and r in the squeezed state is the squeezing parameter.

We can also simplify each modes' Wigner function by plugging in the first two moments into Eq.2.10. This yields the following Wigner functions for the specialized Gaussian modes previously discussed [60, 71, 72].

Gaussian Mode	Wigner Function
vacuum	$W_{\|0\rangle}(q, p) = \frac{1}{\pi} e^{-q^2 - p^2}$
thermal	$W_{\|th\rangle}(q, p) = \frac{1}{\pi(2nth+1)} e^{\frac{-q^2-p^2}{2n_{th}+1}}$
coherent	$W_{\|\alpha\rangle}(q, p) = \frac{1}{\pi} e^{-(q-\sqrt{2}\|d\|\cos\theta)^2 - (p-\sqrt{2}\|d\|\sin\theta)^2}$
squeezed vacuum	$W_{\|0\rangle}(q, p) = \frac{2}{\pi} \exp\left[-\frac{2\,\mathrm{Im}^2(d)}{\exp(2r)}\right] \exp\left[-\frac{2\,\mathrm{Re}^2(d)}{\exp(-2r)}\right]$

2.10 Linear Transformations

We are not reconstructing stationary modes in a cavity, contrary to our initial electric field descriptions, but propagating field modes and measuring them with photo-detection methods (Sec. 5.2). By following the Heisenberg picture, where the mode observable

operator, A, is modified by propagation U as

$$A' = U^{\dagger} A U. \tag{2.28}$$

The general state transformation equation yields symplectic matrices, or matrices that preserve linear transformations as modes propagate [4]. This does not inherently infer that the matrix is symplectic, but as we are working in that space, we later will assume operator $A = A'$ such that symplectic form is preserved $A = U^T A U$. Mode propagation through time independent elements can generally be described as

$$U = e^{i\mathcal{H}\tau/\hbar} \tag{2.29}$$

where $\mathcal{H}$ is the interaction Hamiltonian and τ characterizes the interaction strength. Due to canonical quantization, the Heisenberg picture is very similar to classical principles and the annihilation operator $\hat{a}$'s equations of motion are the same as the classical electromagnetic field amplitude d [4]. This highlights the intuition we can have about our spatial modes, as they maintain Gaussian distributions, and many classical characteristics remain true so long as we do not extend to higher orders of moments.

An input Gaussian state will remain Gaussian, regardless of the unitary transformation performed at the lower orders which we are working at. Recall it is a requirement of quantum mechanics that all transformations be unitary to preserve probability, and thus be reversible [73].

Experimentally in the lab, we are unable to directly detect the state immediately after creation, thus we need to account for any changes the state(s) may have undergone during propagation. Luckily, propagation transformations are well-studied and understood for Gaussian states [74].

More so, we can limit propagation to linear transformations as we are limited to phase shifts, or rotations, (R as in Eq.2.30) and beam splitters (B as in Eq.2.31) in the lab. The phase shifter rotates the optical phase of an electromagnetic wave. The beam splitter mixes two states together, though the second state may be vacuum.

Both beam splitters and rotation matrices represent unitary transformations. Unitary transformations are characterized by their ability to preserve the inner product of vectors in a Hilbert space, which means they conserve energy and are invertible. Beam splitters, in particular, are unitary because they ensure that the total energy of the input states is conserved in the output states. Rotation matrices, which represent rotations in Euclidean space, are also unitary (or more specifically, orthogonal in the real case) because they preserve lengths and angles between vectors.

Gaussian states undergoing linear transformations will remain Gaussian [75]. This preservation comes from a 'free' Hamiltonian matrix in a continuous variable (CV) system [50]. In other words, these transformations preserve energy and are known as 'Passive Transformations'. Passive transformations, by definition, do not change the photon number in a state as it propagates through linear optical elements.

The rotation matrix generally takes the form $R = e^{\theta J}$ where $J = \begin{pmatrix} 0 & 1 \\ -1 & 0 \end{pmatrix}$ and θ is the angle of rotation between the initial state $z = \begin{pmatrix} q \\ p \end{pmatrix}$ and the detected state $z' = \begin{pmatrix} q' \\ p' \end{pmatrix}$ after propagation. We next move from an exponential map to a trigonometric map in order to generalize phase shift transformations and permit them to be more in line with what we see in the laboratory optical elements. If we Taylor expand the exponential such that $e^{\theta J} = J + Jsin(\theta) + J^2(1 - cos\theta)$, we can simplify to a trigonometric expression, shown in Eq. 2.30.

2.10.1 Experimental Linear Transformations

Transformation matrices are written in the $(q_1, p_1, \ldots, q_n, p_n)$ basis order. Later on in Section 4.2 we will reshuffle the basis ordering to $(q_1, \ldots, q_n, p_1, \ldots, p_n)$. But for now it is easier to build up an intuition when mode components are ordered together. The rotation transformation (R) of a basis is equivalent to a phase shift of an electric field due to propagation. In (q,p) quadrature basis, the rotation of state z is described by

$$z' = R_{n=1} z \tag{2.30a}$$

$$\begin{pmatrix} q' \\ p' \end{pmatrix} = \begin{pmatrix} \cos\theta & \sin\theta \\ -\sin\theta & \cos\theta \end{pmatrix} \begin{pmatrix} q \\ p \end{pmatrix} \tag{2.30b}$$

where θ is the angle of rotation between the initial state (z) and the detected state (z') after propagation, and there is one mode in the system, $n = 1$. The beam splitter transformation mixes two modes ($n = 2$) together such that in (q,p) quadrature basis

$$z' = B_{n=2} z \tag{2.31a}$$

$$\begin{pmatrix} q'_{n=1} \\ p'_{n=1} \\ q'_{n=2} \\ p'_{n=2} \end{pmatrix} = \begin{pmatrix} \sqrt{1-T} & 0 & \sqrt{T} & 0 \\ 0 & \sqrt{1-T} & 0 & \sqrt{T} \\ \sqrt{T} & 0 & -\sqrt{1-T} & 0 \\ 0 & \sqrt{T} & 0 & -\sqrt{1-T} \end{pmatrix} \begin{pmatrix} q_{n=1} \\ p_{n=1} \\ q_{n=2} \\ p_{n=2} \end{pmatrix} \tag{2.31b}$$

where T is the transmission coefficient of the mixed modes from the beam splitter and the reflection is thus $\sqrt{1-T}$ [65]. To preserve energy note, $|(1-T)|^2 + |T|^2 = 1$.

Note the negative off-diagonal term in Eq.2.30 is present as rotation matrices are orthogonal, meaning their transpose is their inverse ($R^T = R^{-1}$). This ensures the matrix represents a pure rotation without scaling or mirroring.

The transmissivity of the beam splitter can also be described by $cos^2\theta$, and thus the reflectivity takes the form $sin^2\theta$, where θ is the angle of rotation.

We will further discuss these transformation matrices in the next subsection and go through a few simple examples to build up intuition.

2.10.2 State Transformation Examples

Fig.2.4 shows several simple examples of single and two-mode systems propagating over some distance in free space. We walk through examples of a single mode undergoing no rotation (Fig.2.4a), experiencing some change (Fig.2.4b), two non-interacting modes (Fig.2.4c), and two interacting modes (Fig.2.4d).

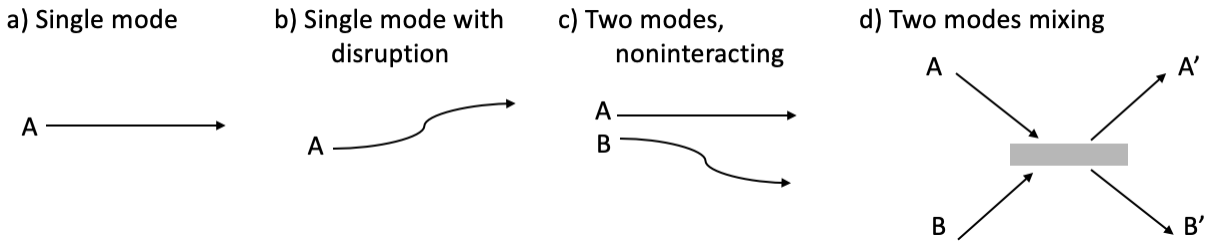

FIG. 2.4: Examples of mode propagation where a) is a single mode (A) traveling some length (↕) and undergoing no path transformation, b) shows a single mode (A) traveling some length (↕) and experiencing some phase change, θ, c) shows two non-interacting modes where mode A does not experience any rotation transformation but mode B does. d) shows two modes mixing together via a beam splitter transformation (Eq.2.31).

As shown in Figure 2.4a, a single mode (A) propagating through space and not experiencing any disruption undergoes a rotation transformation that does not alter or change its original form. Thus, the angle between the initial and detected state is $\theta = 0$. Plugging this into Eq.2.30 results in a matrix of $R_a = \begin{pmatrix} 1 & 0 \\ 0 & 1 \end{pmatrix}$. Note this is essentially the identity matrix. This makes sense as passive transformations should preserve the identity transformation, which maps a state to itself.

If instead the single mode (A) experiences some disruption during propagation, as shown in Fig. 2.4b, we can no longer set $\theta = 0$ as some rotation was experienced. Instead, the transformation is described as Eq. 2.30.

If there is more than one mode present, as is likely to be the case in our experimental system, we need to examine how these modes interact with one another, if at all. Further discussion will be provided in Ch. 3. Fig. 2.4c shows two non-interacting modes, A and B, propagating where mode A does not experience any disruptions ($\theta_A = 0$), but mode B does ($\theta_B \neq 0$). Where we previously only had a single mode and its two quadrature measurements, q_A and p_A, we now have two modes (A and B) and each of their quadratures, q_A, p_A, q_B, p_B, or four quadrature measurements in total. Thus our rotation matrix will double in size from $2x2$ for a single mode, to $4x4$. Maintaining a basis ordering of (q_A, p_A, q_B, p_B), the rotation matrix for two non-interacting modes is

$$R_c = \begin{pmatrix} 1 & 0 & 0 & 0 \\ 0 & 1 & 0 & 0 \\ 0 & 0 & \cos\theta_B & \sin\theta_B \\ 0 & 0 & -\sin\theta_B & \cos\theta_B \end{pmatrix}. \tag{2.32}$$

As modes A and B are not interacting, cross-diagonals yield zero. It should be straight forward to see that R_c is simply a combination of R_a and R_b.

We next move to a more complex case of two modes (A and B) that mix together. This transformation is conducted with a beam splitter, as visualized in Fig. 2.4d where modes A' and B' are the outputs of the process. Mode A's transmission (T) is present in output mode B' and mode A's reflection (1-T) resides in A'. Input mode B follows the opposite process where mode B's transmission is present in A', but mode B's reflection is in B'. This process results in a beam splitter matrix of the form shown in Eq. 2.31.

We can generalize the mode A and B example such that the first mode is actually our q quadrature and the second input mode is the p quadrature. Now $q = a_{out}T + b_{out}(1-T)$ and $p = b_{out}T + a_{out}(1-T)$ for some coefficients a_{out} and b_{out}. Again, T is the transmission and reflectivity is $1-T$ as the sum of transmission and reflection should yield 100% of the propagation possibilities.

Now that some intuition of transformations has been built, we note that any transformation our Gaussian states may go through as the states propagate can be broken down into combinations of rotations and beam splitters.

CHAPTER 3

Multimode Quantum Gaussian States

In this chapter, we expand on single Gaussian states by redefining the q and p quadratures used in the Wigner function (Eq. 2.10) to now be arrays $q = (q_1, q_2, \ldots, q_n)$ and $p = (p_1, p_2, \ldots, p_n)$ for n modes. Previously we looked at single mode cases and how they propagate through space as in Sec. 2.10. However, the problem becomes much more complex as modes not only change as they propagate, but can mix with each other. This is the crux of the problem we aim to solve - to separate out independent modes from one another via their squeezing parameters. Ideally, the separated modes can then inform us how to better modify our measurement system, discussed in Sec. 5.4 [76].

The covariance matrix contains mode information, but in order to obtain this information, we need to decompose the covariance into individual modes, as we will discuss in Ch. 4. To verify our decomposition process, we verify our method via a simulated process, outlined in Sec. 4.3.

Multimode quantum systems are significantly more difficult to work with and measure

than single modes, but can be desirable in fields such as optical information multiplexing [77, 78] or imaging [30, 79, 80]. As our system produces multimode states (see Sec. 5.1), we are further motivated to study multimode systems.

Multimode states involve two or more spatial modes, where optical power is distributed across several mode patterns. Multimodes are higher-order modes that can be decomposed into a sum of Gaussian states, specifically a mixture of squeezed vacuums and thermal states [65]. Unfortunately for us, multiple single vacuum squeezed modes can mix with one another or be contaminated by thermal modes, and the total measurable amount of squeezing may be less than what is present in one mode individually.

3.1 Multimode Analogy

Let's walk through an analogy to build intuition of multimode systems. Generally, we categorize single modes as either squeezed or contaminating to squeezing modes. Contaminating modes are considered to be thermal modes. Each squeezed mode has a unique squeezing parameter (r) while thermal modes are spatially indistinguishable from one another if they are spatially overlapped.

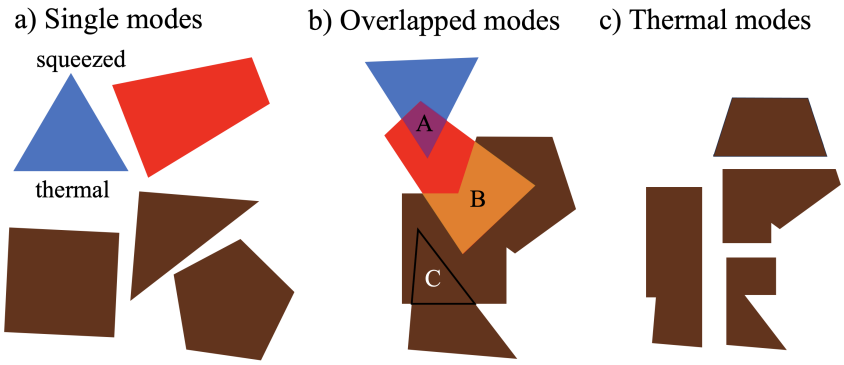

FIG. 3.1: a) Two squeezed modes (blue and red) and three thermal modes (brown). b) The modes in part a are now overlapped such that area A shows two squeezed modes overlapped, area B shows one squeezed mode and one thermal mode overlapped, and area C shows the overlap of two thermal modes. c) Four thermal modes.

Let's consider a system with two squeezed modes and three thermal modes, all with arbitrary spatial shapes as displayed in Fig. 3.1a. As the squeezed modes are indistinguishable, we give one a squeezing parameter of $r = blue$ and the other of $r = red$, referring to the blue triangle and red trapezoid respectively. As thermal modes are only distinguishable spatially, they are all shown in brown. When none of the modes are spatially overlapped, each modes' shape is simple enough to see.

As we look at Fig. 3.1b, we see three areas of overlap: A,B, and C. Area A shows two squeezed modes overlapped such that there is some interference between the two. Depending on the orientation of their noiseballs, the total squeezing may be reduced. Area B shows the overlap of one squeezed mode and one thermal mode. The brown thermal mode will reduce the total squeezing that the red trapezoid originally may have had. In area C, we have the overlap of two thermal modes. As thermal modes are indistinguishable, area C is simply categorized as a thermal mode and maintains its brown color in our analogy. Unlike two squeezed modes negatively interfering as shown in Fig. 3.2, thermal modes have an arbitrary mode decomposition as they lack phase-sensitive coherence, or have a flat phase, as discussed in Subsec. 2.8.1. To expand on this point, it is equally valid to break up the thermal modes into any shape structures, as shown in Fig. 3.1c.

We will now return to discussing our measurement and post-processing techniques, focusing on squeezed modes.

3.2 Two Squeezed Vacuum Modes

Two squeezed modes' noiseballs (Sec. 2.7) are shown in blue and red in Fig. 3.2. The two squeezed modes are rotated in different directions in phase space (or their fields have different phases), and the mixed mode noiseball is shown in purple. The final mixed purple noiseball is significantly less squeezed than either of the original input noiseballs, although

some squeezing remains in this example.

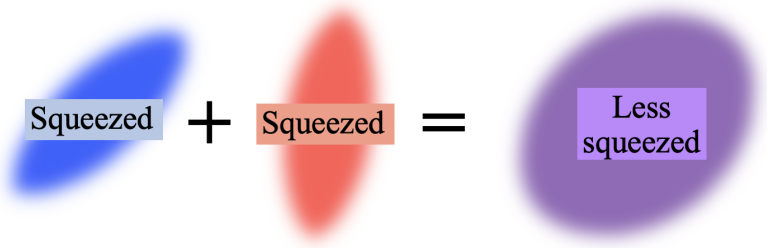

FIG. 3.2: Two single squeezed noiseballs (blue) interfere into a multimode noiseball (purple)

However, we cannot enhance squeezing without furthering experimental techniques and post processing that separate out the squeezed noiseballs. As each squeezed mode has its own squeezing parameter, we aim to find single squeezed modes and separate them out via their unique squeezing parameter (r).

Two squeezed modes produce a covariance matrix of the form:

$$\Sigma_{sqz_1,sqz_2} = \begin{pmatrix} r_1, \phi_1 & 0 \\ 0 & r_2, \phi_2 \end{pmatrix} \tag{3.1}$$

where the first quadrant (blue) plugs r_1 and ϕ_1 into Eq. 2.23 and the bottom quadrant (red) plugs r_2 and ϕ_2 into Eq. 2.23. The blue and red blocks represent a 2x2 matrix, one per mode in the system. The off-block-diagonal 2x2 blocks are all 0 in this instance. However, Eq. 3.1 makes the assumption that neither noiseball of the squeezed state interferes with the other, which is highly improbable. As there is likely mode mixing occurring, we introduce a spatial shape sorting, or detection, process that discusses how this noiseball mixture affects the experimentally measured covariance matrix.

3.2.1 Spatial Shape Matching Effects

Spatial shape information about single modes in the system can be fed back into the experiment through a technique discussed in Sec. 5.4 and originally used in [76] to reduce a mismatch of spatial mode shapes. Thus far we have assumed perfect overlap between the signal of interest and its reference, which we use for detection as demonstrated by Fig. 3.3. Further details of this process are discussed in Ch. 5, but we first discuss how overlap affects our measured covariance matrix.

With the assumption of perfect mode matching in our detection scheme, we essentially 'mode sort' the true spatial mode, in this case a square, A (Fig. 3.3a), by a square mode sorter (Fig. 3.3b) and then measure how well the sorting shape aligned with the true spatial mode shape (Fig. 3.3c).

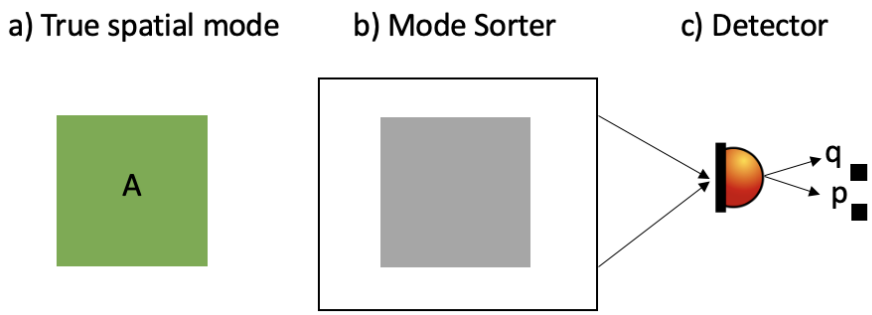

FIG. 3.3: a) True shape of the single squeezed spatial mode. b) The shape used to measure the spatial mode, which perfectly aligns to the spatial mode. c) The device used to detect quadratures q and p of the mode sorter

As this is the scheme we have assumed thus far, the covariance of a single squeezed mode here would take the form of Eq. 2.23. This assumption can be expanded to n modes with n perfectly overlapped mode sorter shapes. The resulting covariance would result in a block-diagonal matrix made of n 2x2 blocks where all off-diagonal blocks had elements of 0, following the structure of Eq. 3.1.

However, it is more likely that our selected mode sorter spatial shape does not perfectly

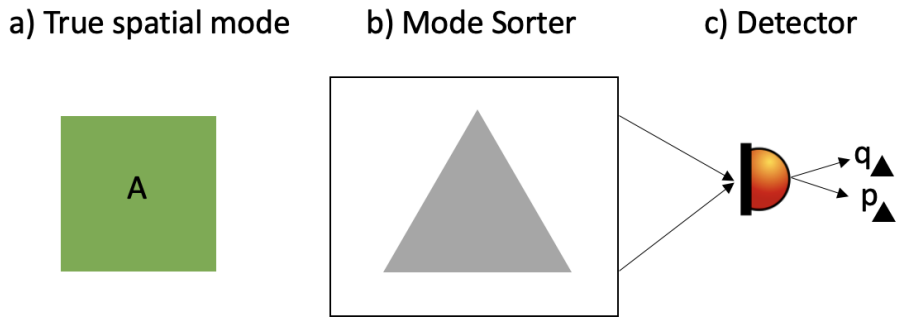

FIG. 3.4: a) True shape of the single squeezed spatial mode. b) The shape used to measure the spatial mode, which does not align to the spatial mode. c) The device used to detect quadratures q and p of the mode sorter

align with the true spatial mode, as demonstrated with Fig. 3.4. Unlike in Fig. 3.3b, here we are using a triangle shape that does not spatially match the true square mode, A, shown in Fig. 3.3a. Now that we are attempting to detect q and p of a triangular spatial shape, our cleanly diagonalized covariance matrix for a single squeezed is no more, and we must account for off-diagonal terms such that

$$\Sigma_{sqz} = \begin{pmatrix} e^r \cos^2\theta + e^{-r}\sin^2\theta & [e^{-r} - e^r]\cos\theta\sin\theta \\ [e^{-r} - e^r]\cos\theta\sin\theta & e^r \sin^2\theta + e^{-r}\cos^2\theta, \end{pmatrix} \tag{3.2}$$

where the diagonal elements are the same as our perfectly matched single squeezed mode, Eq. 3.1, but with additional off-diagonal terms in the block-diagonal. We can again expand this logic to n modes with no spatial overlap of their mode sorter shape, resulting in a more intensive covariance matrix.

3.3 One Squeezed Vacuum and One Thermal Mode

In addition to the potential of the squeezing modes negatively interfering with one another, our system also likely contains contaminating thermal modes, which typically have larger noiseballs than squeezed vacuum states. Thermal modes may reducing squeezing

or even eliminate it completely, as illustrated in Fig. 3.5 where a blue noiseball of a squeezed mode and an orange noiseball of a thermal mode are mixed, resulting in a purple noiseball of an undefined state. Mixed modes are generally larger and less anisotropic than the squeezed mode alone. The thermal mode, characterized by a circular noiseball with radius determined by its mean photon number n_{th}, tends to "inflate" the squeezed state's noiseball, thereby reducing or even eliminating the observable squeezing.

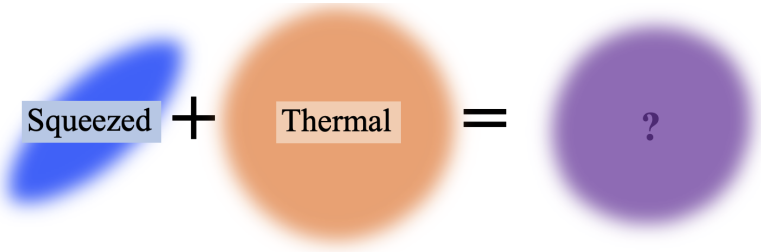

FIG. 3.5: One noiseball of a squeezed state (blue) and one noiseball of a thermal state (orange) interfere into a multimode noiseball (purple)

The covariance of the mixed squeezed and thermal mode has the diagonal block form of

$$\Sigma_{sqz,th_k} = \begin{pmatrix} e^r \cos^2\theta_k + e^{-r_k}\sin^2\theta_k + \mathbf{2n_{th_k}} & [e^{-r_k} - e^{r_k}]\cos\theta\sin\theta \\ [e^{-r_k} - e^{r_k}]\cos\theta\sin\theta & e^{r_k}\sin^2\theta_k + e^{-r_k}\cos^2\theta_k + \mathbf{2n_{th_k}}, \end{pmatrix} \tag{3.3}$$

where the matrix is changed by adding twice the thermal photon average ($2n_{th_k}$) to all diagonal terms of Eq. 3.2 for the k^{th} mode [65]. The mixed covariance state has the form

$$\Sigma_{sqz_1,th_2} = \begin{pmatrix} r_1, \phi_1, n_1 = 0 & c(sqz_1, th_2) \\ c(th_2, sqz_1) & r_2 = 1, \phi_2 = 0, n_{th_2} \end{pmatrix} \tag{3.4}$$

where the top left diagonal block (blue) and bottom right diagonal block (orange) take the form of Eq. 3.4. The squeezed mode parameters (blue box) include some squeezing

parameter r_1, some squeezing angle ϕ_1 and an average photon count of zero ($n_1 = 0$). The thermal mode (orange box) parameters do not have squeezing ($r_2 = 1$), do not have a squeezing angle ($\phi_2 = 0$), and contain some nonzero average photon number, n_{th_2}. The off-diagonal 2×2 blocks are left in their general covariance form as there is significant quadrature mixing occurring.

CHAPTER 4

Decompositions

Once a covariance matrix of the system is measured (Σ_o), we separate out any linear transformations (C) it may have undergone from its diagonalized form (Σ_d), which describes independent single modes making up the multimode measurement. To find Σ_d, we need to track the change in quadratures, which we will embed into an array as $\vec{X}_n = (q_1, p_1, q_2, p_2, \ldots, q_n, p_n)$, as they directly tie to the change of detected states u, a concatenated matrix where each column is one mode. More precisely, u changes $a^\dagger$ and a, while C is in charge of quadratures. We find that the spatial modes in the quadrature basis take the form $\vec{X}_n$ such that we can determine all linear transformations C experienced from mode creation to detection as

$$\vec{X} = C\vec{X}. \tag{4.1}$$

Essentially, finding the reversible linear transforms, C, permits us to find Σ_d as

$$\Sigma_d = C^T \Sigma_o C \tag{4.2a}$$

$$C\Sigma_d C^T = \Sigma_o \tag{4.2b}$$

in orthogonal mode basis where Σ_o is the initially measured covariance matrix, Σ_d is the diagonalized covariance matrix, and C is some combination of linear transformations the system underwent while propagating to the detector as described in Sec. 2.10. This emphasizes that any transformation must be unitary (i.e. reversible). For example, the modes may have traveled and picked up a phase shift as well as have gone through a beam splitter where mixing occurred, resulting in $C = RB$. We are only able to find spatial modes and squeezing parameters from a diagonalized covariance, rather than the measured covariance, as phase shifts and mode mixing processes are embedded in Σ_o due to propagation. As Σ_o is a measurement we can experimentally perform, we simply need to identify what linear transformations were undergone. In other words, we decompose to find matrix C. It is highly unlikely that the system did not undergo any transformation during propagation from the creation of squeezed light to the detection scheme.

We also note the covariance matrix must still follow Heisenberg's uncertainty principle such that there is a lower bound of 0 for all eigenvalues of the covariance matrix [50, 70]. A proof of the matrix inequality condition is provided in [50], but we will continue on with the result as this positivity condition is used to verify our reconstructions and will be used later on in Sec. 7.4.

The decomposition of the covariance is done in two parts and is modified from open source quantum photonic algorithms, Strawberry Fields [70].

4.1 Forward System Propagation

Prior to discussing the decomposition processes, we first generalize how the system propagates the diagonalized covariance matrix (Σ_d) into the covariance matrix we measure

(Σ_o).

u is the transformation of creation and annihilation operators vector such that the spatial modes in the system can be concatenated into $u_{d_{n\times n}}$ for n modes. u_d forms a basis set. Initially u is in a creation and annihilation operator basis defined as $\vec{A_n} = (a_1^\dagger, \ldots, a_n^\dagger, a_1, \ldots, a_n)$. We redefine u to explicitly include its conjugate components, as it is in a creation and annihilation operator basis such that

$$U_{2n\times 2n} = \begin{pmatrix} u_{n\times n} & 0_{n\times n} \\ 0_{n\times n} & u^*_{n\times n} \end{pmatrix}. \tag{4.3}$$

We transform $\vec{X}$ into quadrature basis, using operator Q as defined in Eq. 2.8 as

$$C_o = P_{2n\times 2n} U_{2n\times 2n} P_{2n\times 2n} Q_n^{-1} \vec{X}_n^T \tag{4.4}$$

where Q_n is a diagonalized matrix made of n 2×2 Q matrices blocks and matrix P reorders spatial matrix U from $(a_1^\dagger, \ldots, a_n^\dagger, a_1, \ldots, a_n)$ ordering to $(a_1^\dagger, a_1, \ldots, a_n^\dagger, a_n)$, according to the following recipe. Matrix U is ordered as $(a_1^\dagger, \ldots, a_n^\dagger, a_1, \ldots, a_n)$ but must be ordered as $(a_1^\dagger, a_1, \ldots, a_n^\dagger, a_n)$ to continue on in our forward propagation of the spatial modes to a covariance matrix. This is done via a 'reordering' process, or a permutation of the rows (P_r) and permutation of the columns (P_c) of the matrix U. The row permutation first accounts for the odd-ordered rows, then even-numbered rows. As an example, if $n = 2$,

$$U_{reorder_{2n\times 2n}} = P_{2n\times 2n} U_{2n\times 2n} P_{2n\times 2n}. \tag{4.5a}$$

$$\begin{pmatrix} u_{1,1} & 0 & u_{1,2} & 0 \\ 0 & u_{1,1}^* & 0 & u_{1,2}^* \\ u_{2,1} & 0 & u_{2,2} & 0 \\ 0 & u_{2,1}^* & 0 & u_{2,2}^* \end{pmatrix} = \begin{pmatrix} 1 & 0 & 0 & 0 \\ 0 & 0 & 1 & 0 \\ 0 & 1 & 0 & 0 \\ 0 & 0 & 0 & 1 \end{pmatrix} \begin{pmatrix} u_{1,1} & u_{1,2} & 0 & 0 \\ u_{2,1} & u_{2,2} & 0 & 0 \\ 0 & 0 & u_{1,1}^* & u_{1,2}^* \\ 0 & 0 & u_{2,1}^* & u_{2,2}^* \end{pmatrix} \begin{pmatrix} 1 & 0 & 0 & 0 \\ 0 & 0 & 1 & 0 \\ 0 & 1 & 0 & 0 \\ 0 & 0 & 0 & 1 \end{pmatrix}. \tag{4.5b}$$

Once $U_{reorder}$ is in quadrature basis, use Eq. 4.4 to find C. As Σ_o is already measured, we simply follow Eq. 4.2 to determine the diagonalized covariance, Σ_d, a process outlined in the next section. Note, for our decompositions we need to shuffle C in $(q_1, \ldots, q_n, p_1, \ldots, p_n)$ order one more time.

4.2 Backwards Propagation

Now we have the measured covariance matrix, Σ_o and a method of determining the linear transformations that make up C we find its diagonalized form, Σ_d through Eq. 4.2. This is done in two backwards propagating steps, Williamson Decomposition and Bloch-Messiah Decomposition.

4.2.1 Williamson Decomposition

We first analyze the covariance matrix in a thermal field basis, known as Williamson decomposition [51] described as

$$\Sigma_o = SDS^T \tag{4.6}$$

where S is a symplectic transformation acting on a state described by the diagonal matrix D. Contaminating thermal modes can be decomposed from matrix D, which describes the input thermal modes as $D = \text{diag}(n_{th_1} + 1, n_{th_2} + 1, \ldots, n_{th_k} + 1, n_{th_1} + 1, n_{th_2} + 1, \ldots, n_{th_k} + 1)$ where n represents the photon number of the mode of the k^{th} mode [70].

Eigenvalues of 1 in matrix D indicate a vacuum state as diagonal elements are equal to the photon number in the mode plus one. Should no photons be present ($\nu_{th} = 0$), this leaves us with a value of 1 corresponding to vacuum mode inputs. D matrix diagonal values larger than one indicate some thermal or mixed states. Although matrix D is not used in squeezed mode reconstruction, its physical requirement of diagonal elements to be greater than or equal to 1 is a key factor that we use in Sec.7.4.

The S matrix in Eq. 4.6, holds the modes' squeezing parameters and mixing transformations, which we separate in the next decomposition step. Matrix S represents the linear transformations that preserve the form of our Gaussian state, as discussed in Sec. 2.10, holds the remaining modes and their squeezing parameters. We send S on to the next step of our decomposition process.

4.2.2 Bloch Messiah Decomposition

Bloch-Messiah decomposition, uses the matrix S from Williamson decomposition, which can now be decomposed into orthogonal matrices O_1 and O_2 and a diagonal matrix Z. O_1 and O_2 are both required in order to maintain unitary transformations, a condition of quantum operators.

$$S = O_1 Z O_2 \tag{4.7}$$

where O_1 and O_2 matrices are orthogonal matrices that hold the linear transformation information. This leaves Z, which holds the squeezing parameter information, r, as $Z = \text{diag}(e^{r_1}, \ldots, e^{r_n}, e^{-r_1}, \ldots, e^{-r_n})$ is the set of single mode operations for n modes with squeezing values $(r_1, \ldots, r_n)$, respectively. Consequently, e^{-r_i} terms hold noise suppression information [70]. Note in a perfect vacuum mode, antisqueezing is the inverse of the squeezing parameter or, $\frac{1}{r}$.

Squeezing parameters (r) can now be easily seen and we continue on to find the spatial mode information from matrix O_1. Breaking the matrix up into four quadrants, the top left of the matrix indicates the real part of the modes (let's call it A), and the top right of the matrix indicates the complex part of the modes (let's call it B). Reconstructed unwrapped modes of the system are found by $U = A + iB$ where each of matrix U's columns make up one reconstructed mode. The mode reshaping will be visualized in Sec. 4.3.

Note O_2 is not explicitly used, but is still an output requirement to maintain unity. Matrices O_1 and O_2 are passive Gaussian transformations (Sec. 2.10) and are orthogonal to one another such that we only need to use one to reconstruct mode shapes.

4.3 Simulation

Prior to utilizing the decomposition method on experimental data, we first demonstrate the decomposition method with a simulated model. This permits us to check our backward propagating system buildup compared to how it would forward propagate, as the experimental setup does.

First, we need to build up a simulated covariance matrix such that it mimics what we expect to see in the experiment. To do this, we determine the modes, their squeezing parameters, and the number of pixels (n) used in reconstruction. We demonstrate this simulation and decomposition method with a single squeezed vacuum mode, whose amplitude is shown in Fig. 4.1 over $n = 16$ pixels, creating a 4×4 matrix. For simplicity of the demonstration, the input mode has a flat phase. The simulated squeezing parameter is set to $r = \sqrt{0.5} \approx 0.707$.

An orthogonal set of modes, which includes our selected modes, are shown as $u_{n=16}$ in fig. 4.2 where each column is an unwrapped spatial mode. As we only sent in one mode, we focus only on the first column, boxed in red in fig. 4.2. The other columns complete

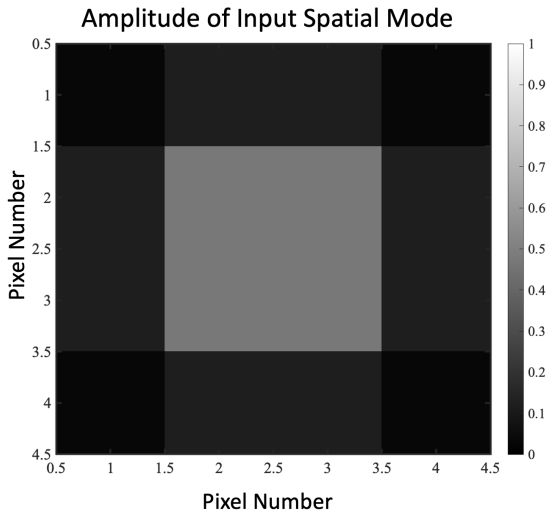

FIG. 4.1: Single simulated input spatial amplitude mode, digitized to 16 pixels.

an orthogonal basis set, but as we left them undefined, they are vacuum modes.

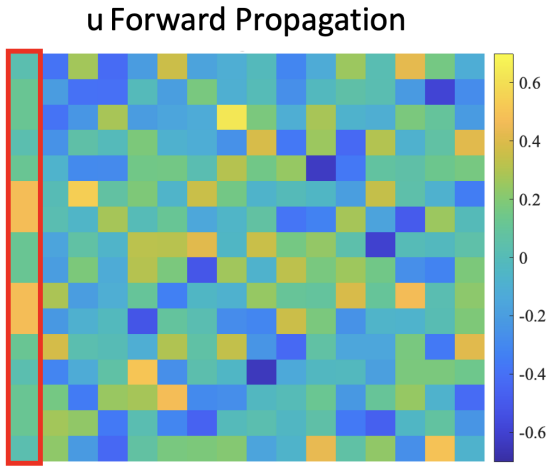

FIG. 4.2: An orthogonal basis mode set, where the first column is our input single mode.

By following Eq. 4.3, matrix u is expanded to matrix u_d as shown in Fig. 4.3. Here, the first two columns hold our input spatial mode information.

We next transform mode matrix u by q and p quadrature definitions per spatial pixel, as expressed in Fig. 4.4. From there, we find all linear transformations, C, and create a

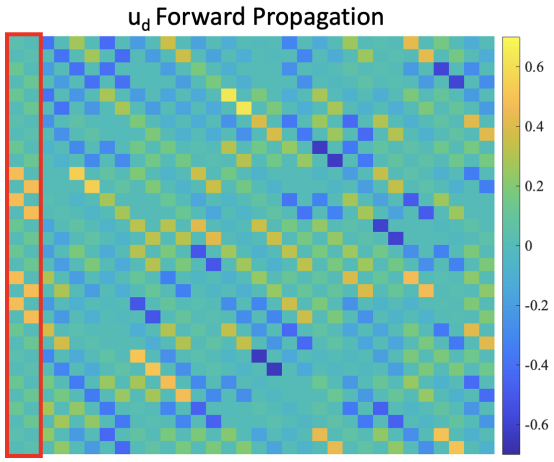

FIG. 4.3: Orthogonal basis modes, u_d, where the first two columns are our input single mode.

simulated covariance matrix (Fig. 4.4) via

$$\Sigma = Cr_nC^T \tag{4.8}$$

where r_n is an array of our inputted squeezing values. r_n is the same as Σ_d, if there are no thermal modes (which is the case of this simulation). The simulated covariance matrix is now in $(q_1, q_2, \ldots, q_n, p_1, p_2, \ldots, p_n)$ form, a requirement for our back-propagation process, or decompositions.

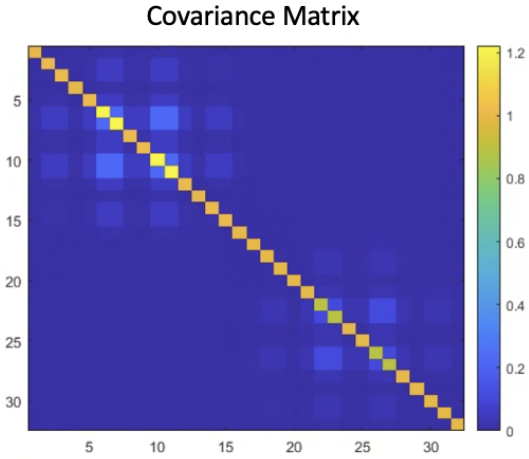

FIG. 4.4: A simulated covariance matrix for the inputted single squeezed mode

Now that a covariance matrix is created, we send it through the decomposition method described in Sec. 4.2. First, using the Williamson Decomposition process, matrix S (Fig. 4.5) shows the symplectic output and is used as the input for Bloch-Messiah Decomposition. Williamson Decomposition also produces the diagonalized matrix, D, and is not explicitly shown here as we do not explicitly use it in further squeezed mode reconstruction steps. D provides information of thermal modes present in the system and is discussed more in Sec. 7.4.

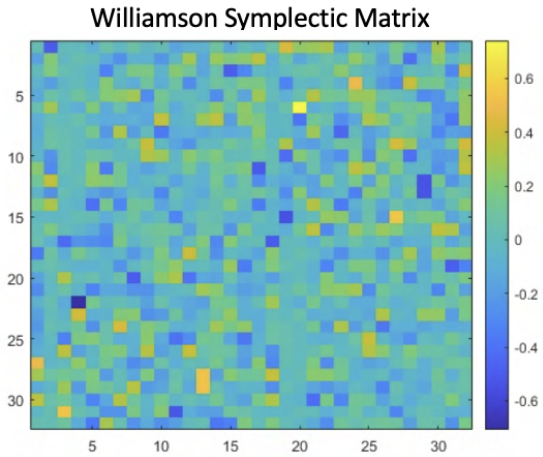

FIG. 4.5: Williamson symplectic matrix S

After sending matrix S through Bloch-Messiah Decomposition, we yield matrices O_1 (Fig. 4.7), Z (Fig. 4.6), and O_2 (not shown). Matrix Z is diagonalized and is ordered from the strongest mode's antisqueezing level through the weakest mode's antisqueezing about halfway through the matrix's diagonal. Then the order repeats from the strongest to weakest modes, but instead shows their squeezing levels. Note as we only sent in one mode, only the first and 17^{th} $(n+1)$ diagonal elements have non-one values.

It is in this step that we find the squeezing parameter of the spatial mode to be $Z(17,17) = \sqrt{0.5} = 0.707$, which matches our input of $r = 0.707$. As we simulate a perfectly squeezed mode, we can also find the antisqueezed value of $Z(1,1) = \sqrt{2} = 1.41$,

or $\frac{1}{r}$. The decompositions always order spatial modes from strongest to weakest. The other 15 modes are vacuum and have Z diagonal values of 1 indicating no squeezing.

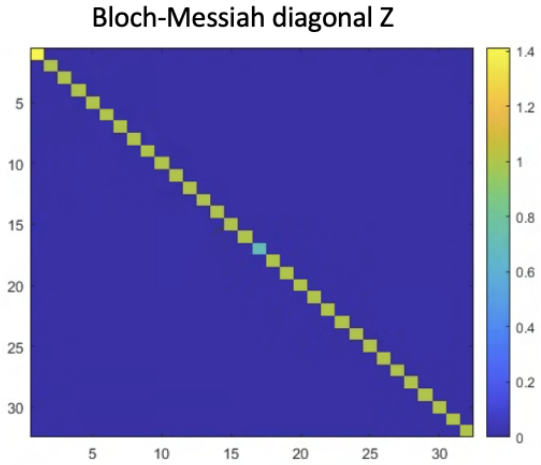

FIG. 4.6: Bloch Messiah diagonalized matrix Z

Leaving O_2 behind, we use matrix O_1 to find the final mode shapes we are after.

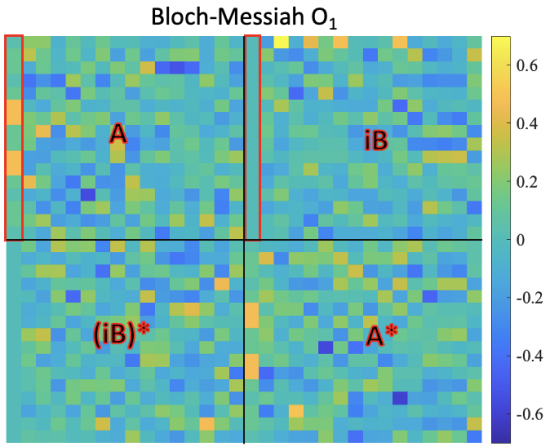

FIG. 4.7: Bloch Messiah orthogonal matrix O_1

However, there is one final reordering step we need to take to reveal the mode shape. O_1 is broken up into quadrants where we use the top two quadrants in our reconstruction [70] as shown in Fig. 4.7. Let's call the top left quadrant A and the top right quadrant B. By element summing A and a complex version of B together $(A+iB)$, we return arrays

of each reconstructed mode, concatenated together in a matrix, u, as shown in Fig. 4.8. The spatial reconstruction of the one spatial mode we input into the system uses the first column in A and the first column in iB (which is flat due to no phase input), all boxed in red in Fig. 4.8.

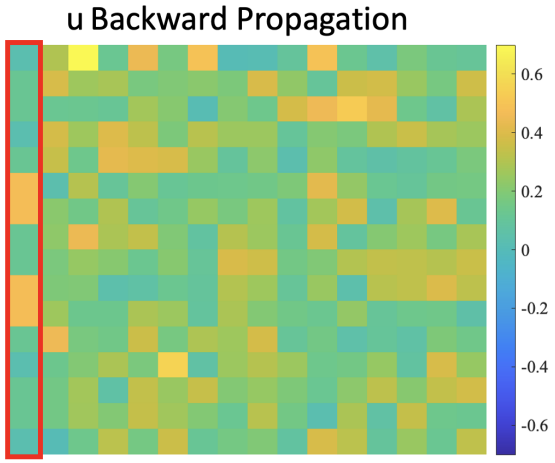

FIG. 4.8: Concatenated matrix $u = A + iB$ where each column is an unwrapped reconstructed spatial mode.

We see the backwards propagation of $u = A + iB$ in Fig. 4.8, which should match Fig. 4.2 for any existing modes. Note that this is true for the first columns of the forward and backwards propagating u, but as the other modes are vacuum, their spatial modes are random.

The final mode reconstruction amplitude is shown in Fig. 4.9b, which matches Fig. 4.1 and is reprinted here as Fig. 4.9a. This simulation is later used throughout Ch. 7 to better conceptualize experimental data and results.

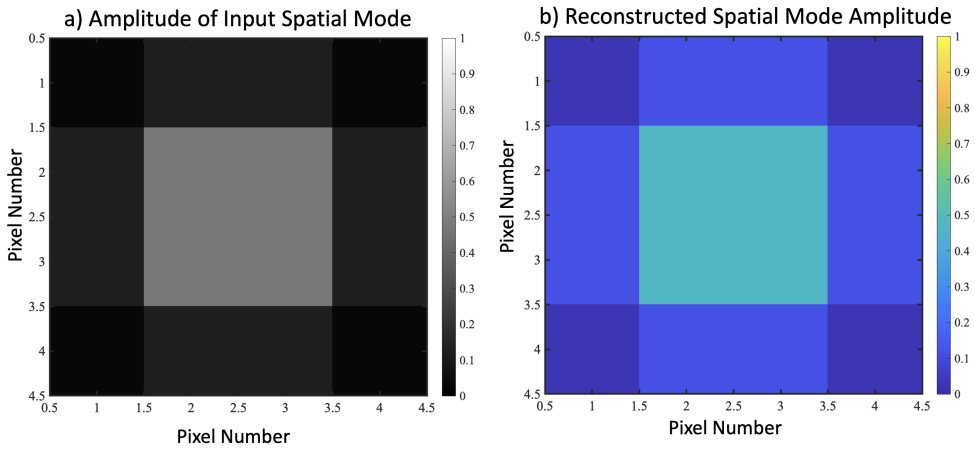

FIG. 4.9: Final mode reconstruction shape's amplitude and phase.

CHAPTER 5

Classical Experimental Techniques

We break down the experimental apparatus into multiple parts, as shown in Fig. 5.1: a squeezing mechanism, reference laser, interferometer made of a local oscillator and squeezed probe, a local oscillator shaping mechanism, homodyne detection, and lastly a final mode reconstruction. Each experimental component is further described in the chapter.

5.1 Squeezer

As we are interested in measuring squeezed light, we first need to create it via some squeezing process (Fig. 5.1a). Creating squeezed modes involves setting up the correct atom-light interaction conditions for squeezing to be possible.

Nonlinear optical processes are fundamental to generating squeezed light, as squeezing inherently requires a nonlinear interaction to redistribute quantum noise between conjugate variables, such as quadratures q and p. This noise redistribution is what causes the squeezing as there is now more uncertainty in one cross section than the other, recall Subsec. 2.8.3. To characterize nonlinear responses, we note the field's dependence of the

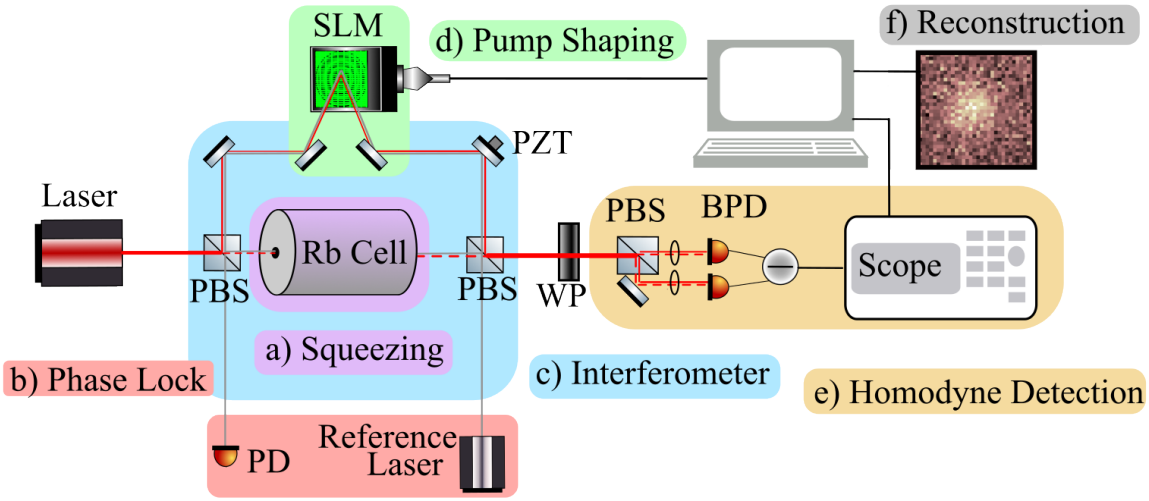

FIG. 5.1: Experimental Setup where a) shows the squeezer with rubidium (Rb), b) is the reference laser used for phase referencing and detected with a photodiode (PD), c) is the interferometer of the signal and LO using polarizing beam splitters (PBS) and a piezoelectric motor (PZT), d) is the LO shaping via the Spatial Light Modulator (SLM), e) uses a waveplate (WP) prior to the homodyne detection scheme, and f) is a final amplitude reconstruction.

dipole moment per unit volume, or polarization, $P(t)$, on the field strength [81]. An electric dipole is formed in the medium due to the distance between a positively charged nucleus and a negatively charged electron. Any perturbations of the nucleus are minimal and we neglect their contributions. We sum the dipole moments from all of the molecules present into a total polarization value defined as

$$P(t) = \epsilon_0 \chi E(t) \tag{5.1}$$

where χ is the linear electric susceptibility, E is the electric field varying in time, and ϵ_0 is the permittivity of free space. Susceptibility is a dimensionless quantity that defines a material's response to an external field, such as the electric field due to the input light. Susceptibility relates to the index of refraction as

$$n = \sqrt{1 + Re(\chi)} \tag{5.2}$$

[82]. Note the imaginary part of χ can correspond to an absorption coefficient but we will maintain χ's complex nature going forward [83, 84]. The change of index of refraction from susceptibility can cause a rotating effect on elliptically polarized light as two indices of refraction result as elliptical light is made of unequal strengths of left-handed circularly (LHC) and right-handed circularly (RHC) polarized light, as discussed in Sec. 2.2 [34].

However, Eq. 5.1 does not account for nonlinear terms that may come about from larger field interactions. To account for this, we power expand susceptibility present in Eq. 5.1 beyond first-order terms such that

$$\chi E = \chi^{(1)} E(t) + \chi^{(2)} E^2(t) + \chi^{(3)} E^3(t) + \cdots \tag{5.3}$$

where we see $\chi^{(1)}$ is the linear susceptibility, $\chi^{(2)}$ is the second-order nonlinear susceptibility, and so on. Our squeezing mechanism depends on $\chi^{(3)}$ nonlinear interactions and that is what we will focus on for the remainder of this text. (Other processes use $\chi^{(2)}$ effects and are discussed in other texts such as [81]).

As the index of refraction is dependent on susceptibility, the index of refraction also contains nonlinear terms. Overall, nonlinear processes expressed here are known as the Kerr nonlinearity [81]. This nonlinearity induces an intensity-dependent refractive index, enabling a strong beam to alter the phase of a weaker beam. The two beams can correspond to the RHC and LHC polarized light present in an elliptically polarized input beam. The beams propagate through a medium and are tuned near the resonance of the medium, the intensity of the stronger beam alters the refractive index experienced by the weaker beam, leading to a phase shift in the weak beam through the AC Stark shift as shown in Fig. 5.2 in an atomic rubidium system [85].

Through a lambda three-state energy level scheme, large refractive indices can be obtained while maintaining small absorption coefficients [86], a desired effect for our squeezer

in order to optimize a phase shift of one of the polarized beams, compared to the other beam. A phase shift is added to a weaker beam (LHC or RHC in our case) via the stronger second beam (RHC or LHC in our case). The magnitude of the phase shift depends on both the intensity of the strong beam and the properties of the medium and is known as cross phase modulation [87]. The rotation is due to some of the strong field's polarization direction projecting onto the weaker field's polarization direction, depending on the phase between the fields. The output field can then be amplified or attenuated compared to the weak field by their phase difference. When the field is attenuated, there is a reduction in the weak field direction, even for weak fields made up only of vacuum fluctuations, as is our case [34]. Nonlinear interactions take place as long as the two beams physically overlap in the medium. There is almost a 'breathing' to the process where the right conditions yield the right phase, and consequently, self-rotates the ellipticity of the input light by an angle ϕ.

We specifically send linearly polarized light into the medium, rather than elliptical, and still see a rotation phenomena that leads to squeezing production. The inherent presence of vacuum fluctuations still introduces an orthogonal polarization to the input light at times and permits a squeezing effect. When this self-rotation effect occurs, the vacuum field in the opposite linear polarization can be squeezed when in phase alignment with the much stronger input linearly polarized beam. The self-rotating of elliptical light yields the squeezing process used in the experiment, known as polarization self-rotation (PSR) [32]. Note PSR inherently produces multimode squeezing, which motivated our previous discussion of multimode states in Ch. 3.

The self-rotation angle ϕ in PSR depends on the initial ellipticity ε, the self-rotation parameter g, and the optical path length L, and is given by:

$$\phi = \varepsilon g L \tag{5.4}$$

The self-rotation parameter g is dependent on light intensity, the electric field magnitude, and splitting levels (Δ) of the excited state as shown in Fig. 5.2 [88]. Essentially, having g means there is rotation, which means there is squeezing. Thus if the amplitude of RHC and LHC polarized components of the input beam are equivalent, $\epsilon = 0$ and there is no rotation.The self-rotation parameter g is not explicitly derived in this text but follows the process outlined in [88] and is approximated in [18] for atomic rubidium, which is what we use in the experiment. Predicted levels of squeezing have also been well-studied and range from 10 dB [88] to 8 dB [34] below shot noise, or classical limits. However, we experimentally see about 2.5 dB of squeezing, which indicates there is a significant amount of squeezing lost from the mixing of modes, the ultimate problem we wish to solve.

For completeness, we note how squeezing parameters affect field variance as it is a parameter we are interested in measuring (Sec. 2.6). The variance of the field is dependent on both the squeezing parameter g and field angle θ such that

$$\langle \hat{\mathbf{E}}_x(\theta, L)^2 \rangle = \frac{E_0^2}{4} \left(1 - 2gL \sin\theta \cos\theta + g^2 L^2 \cos^2\theta\right), \tag{5.5}$$

where E_x is the field in the $\hat{x}$ direction and L is the atom-light interaction path length [34].

5.1.1 Rubidium

Atomic rubidium (^{87}Rb) is our medium of choice for several reasons. It is analogous to a hydrogen atom with only one valence electron. Hydrogen is a well-studied element in quantum mechanics and is often used in textbooks as a foundational example due to its simplicity [3, 89]. Although other elements such as cesium and lithium also have one valence electron, there are lasers that can access rubidium energy level transitions, making rubidium the preferred element. We also already had rubidium in the lab.

Experimentally, we use the D1 transition line ($\lambda = 795$ nm) between the $5^2S_{1/2}$ ground state and the $5^2P_{1/2}$ excited state (Fig. 5.2) in (^{87}Rb). It has been experimentally shown that ^{87}Rb can produce more squeezing compared to ^{85}Rb [88].

Fig. 5.1a shows a glass cylindrical cell of ^{87}Rb used in the experiment. Several different atomic cells have been used throughout the experimental process and although various cell lengths and the presence (or lack of) buffer gases have been used, the cell is always surrounded by three layers of metal shielding preventing the cell from experiencing any external fields. The shielding also offers us control over the environmental temperature, which will be discussed in Subsec. 5.1.2.

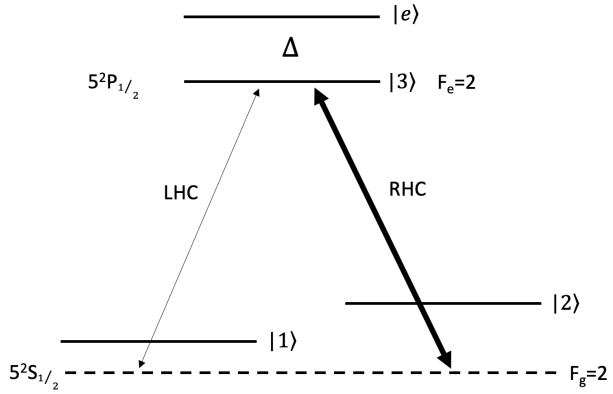

FIG. 5.2: A rubidium lambda system with two superposition ground states $|1\rangle$ and $|2\rangle$, on the $5^2S_{\frac{1}{2}}$ line, each have their own energy transition to the excited state $|3\rangle$, on line $5^2P_{\frac{1}{2}}$. Each transition is made up of either left-handed circularly polarized light (LHC) or right-handed circularly polarized light (RHC). The line transitions go from a ground state of hyperfine level 2 to a hyperfine excited state 2 ($F_g = 2 \rightarrow F_e = 2$). There is also splitting of the excited state from $|3\rangle$ to $|e\rangle$, by some detuning Δ.

5.1.2 Optimizing Squeezing

Experimentally, there are several interacting parameters we can tune to optimize the total squeezing in the system, such as the laser detuning, laser power, and atomic density of the rubidium. Various combinations of the three parameters are further complicated by other components which often overwhelm squeezing at higher atomic densities. We next

discuss the optimization of detuning, laser power, and atomic density of the squeezing operation.

From historical trial and error, the best squeezing in our system is found when the laser is a bit red detuned of the $F = 2 \rightarrow F' = 2$ transition of the D1 line of rubidium, in the valley as shown by the arrow in Fig. 5.3. The valley is approximately 100 MHz wide. The $F = 2 \rightarrow F' = 1$ transition can also produce squeezing, though in our setup it was historically found to yield less squeezing [90].

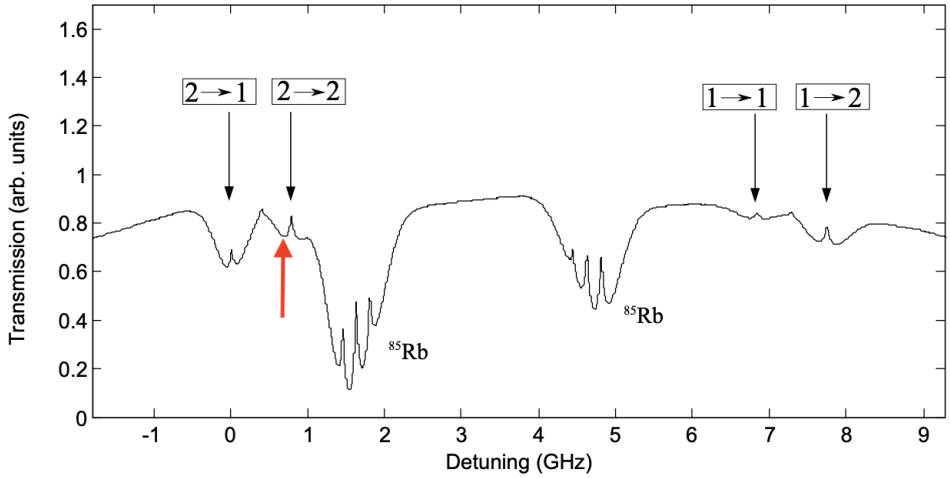

FIG. 4.2: D_1 line absorption resonances of ^{85}Rb and ^{87}Rb shown with saturation spectroscopy. The transitions are labeled $F_g \rightarrow F_e$.

FIG. 5.3: Resonances of rubidium. Optimized squeezing levels are found when the laser is parked in the valley just to the left of the $F = 2 \rightarrow F' = 2$ transition, as pointed out by the bold red arrow. *Reprinted from Horrom Dissertation 2013 [1].*

At low laser intensities, the self-rotation angle ϕ grows proportionally with laser power, following Eq. 5.4, where g scales with intensity [37]. There is a point where intensity-dependent noise overwhelms quantum correlations at all intensities. Power broadening also smears spectral features, reducing squeezing by overlapping nearby transitions. Through experimental optimization, squeezing is maximized when 12 mW of power is sent through the rubidium cell, see Fig. 5.4 for the experimental results of total squeezing levels versus laser power sent into the rubidium cell. Laser power optimization data was taken while

the cell temperature was set to 65°, the historical ideal temperature setting [18].

There are only 18 mW to send through the interferometer (Fig. 5.1c) in total, leaving 6 mW to use for all LO operations, a problem that will come up in Ch. 7. As squeezing production must take priority, we leave low LO power levels as a concern to address later on.

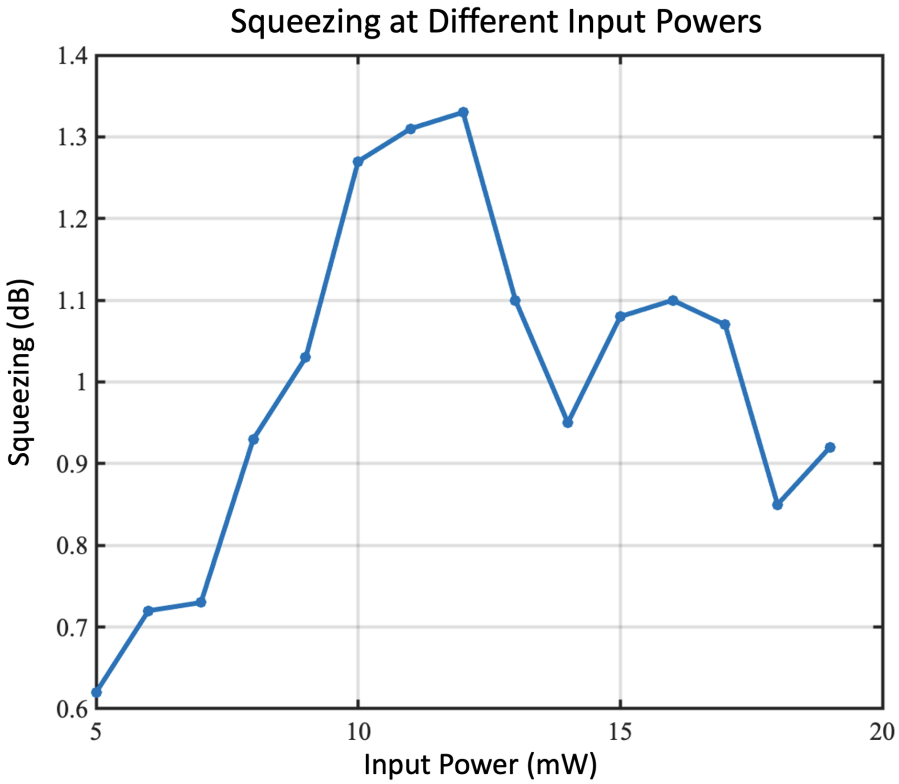

FIG. 5.4: Decibels of squeezing at various input power levels.

We can also vary the temperature of the rubidium cell to control vapor density [91]. Generally, the more atoms in the system, the stronger the interaction. However, there is a threshold where parasitic effects start to dominate at higher atomic densities [1].

Ideally, all squeezing optimization parameters can be locked at their ideal settings. However, laser detuning can drift out of the valley near $F = 2 \rightarrow F' = 2$ by tens of MHz over the course of several hours. Through experience, the laser can stay parked in

its set spot anywhere from 2 hours to 24 hours, depending on weather, humidity, and general kinetic motion of the students surrounding the laser, to name a few parameters. Additionally, the 12 mW laser power entering the cell is not locked. Optical elements between the laser and cell, such as polarizing beam splitters, a fiber to clean up beam shape, and various waveplates will affect the total power reaching the cell. Cell power is checked daily, but does not have an independent stabilization mechanism. Lastly, the temperature of the cell is the only parameter that has its own stabilization control. Through a feedback loop, a temperature setpoint is selected and remains steady so long as the setpoint does not change.

As only temperature can be stabilized, laser power into the cell and laser detuning remain will slightly vary between data collection runs, though they remain steady over a few hours, if not days. A laser lock would rectify the detuning drifts, but we are already power starved due to how much power needs to be sent to the squeezer. There is little power left for additional processes, such as a lock. The lack of stability of several squeezing optimization parameters does affect the reproducibility of the data sets, as later discussed in Ch. 7.

5.2 Detection Scheme

Nearly all optical observable measurements depend on photodetection. This includes our own, in which we utilize homodyne detection (Fig. 5.1e), a common measurement method in quantum optics due to its robust phase measurement abilities. Homodyning is a phase sensitive measurement scheme which permits the differentiation between quadratures through the addition of a local oscillator (LO) [4]. The LO and squeezed signal of interest come from the same lasing source to maintain phase stability in order to adequately provide a phase reference to distinguish between quadratures. The signal and LO additionally have

the same frequency, a condition of homodyning. To create a balanced homodyning process, we send the LO and signal through different arms of an interferometric setup, as seen in Fig. 5.1c where they travel through the same optical elements and have the same path length, aside from the field shaping the LO undergoes in Fig. 5.1d. LO field shaping will be discussed in Sec. 5.4.

Each beam's mean field can be classically described as (α_{LO}) for the local oscillator and the signal field as (α_{sig}). We account for fluctuations of the fields with quadratures q and p such that the total field behavior is described as

$$\alpha_{sig}(t) = \alpha_{sig} + q_{sig} + ip_{sig} \tag{5.6a}$$

$$\alpha_{LO}(t) = [\alpha_{LO} + q_{LO} + ip_{LO}]e^{i\phi_{LO}}. \tag{5.6b}$$

where $e^{i\phi_{LO}}$ indicates the phase difference between the LO and probing signal beam such that the homodyning process measures the variance of the fluctuations under this projection angle [4]. Experimentally, we sweep the relative phase between the signal and local oscillator by adjusting the path length of the signal arm with a piezoelectric transducer (PZT), as shown in Fig. 5.1c. This allows us to rotate the signal's noise distribution in phase space and measure all possible quadrature projections. Without the PZT, we would only detect a single, arbitrary quadrature, and interference fringes would not appear. By mounting the PZT in the signal arm, we achieve precise phase control, enabling complete phase-space characterization.

In our case, the LO is much stronger than the signal field ($\alpha_{LO}^2 >> \alpha_{sig}^2$) as the LO is used to amplify the weak squeezed signal. Our signal is made of vacuum fluctuations, which are too small to be directly detected. Mixing the squeezed signal with a stronger LO via a 50/50 beam splitter (Fig. 5.1c) amplifies the signal such that it is measurable with modern detectors. We use two photodiodes as our detectors in the homodyning setup

(Fig. 5.1d) where each detector sees

$$\alpha_{D1} = \sqrt{1/2}\alpha_{LO}(t) + \sqrt{1/2}\alpha_{sig}(t) \tag{5.7a}$$

$$\alpha_{D2} = \sqrt{1/2}\alpha_{LO}(t) - \sqrt{1/2}\alpha_{sig}(t). \tag{5.7b}$$

which follows standard beam splitter procedures as outlined in [4]. As photo-currents from the two detectors are proportional to $|\alpha_{D1,2}|^2$ (and by neglecting high-order terms, small values, etc) we can obtain more meaningful photo-currents of

$$|\alpha_{D1,2}|^2 = \frac{1}{2}[|\alpha_{LO}|^2 + 2\alpha_{LO}q_{LO}(t) \pm 2\alpha_{LO}(p_{sig}(t)\cos(\phi_{LO}) + ip_{sig}(t)\sin(\phi_{LO}))] \tag{5.8}$$

where q and p are the quadrature operators in phase space. The two detector signals can then be subtracted from one another to yield a differential current of

$$i_-(t) = |\alpha_{D1}|^2 - |\alpha_{D2}|^2 \approx 2\alpha_{LO}(q_{sig}(t)\cos(\phi_{LO}) + ip_{sig}(t)\sin(\phi_{LO})). \tag{5.9}$$

where we see the current scaling with the LO amplitude while LO fluctuations are suppressed. The LO is much stronger than the signal field ($\alpha_{LO}^2 >> \alpha_{sig}^2$), so when the signal and LO are mixed together via a 50/50 beam splitter, each photo diode's current measurement encodes the quadrature information. The squeezed signal (α_{sig}) and LO fields' (α_{LO}) output photocurrent difference is proportional to the quadrature operators as described by the variance:

$$\Delta i^2 = \langle i(t)^2\rangle - \langle i(t)\rangle^2 \approx 4\alpha_{\mathrm{LO}}^2(\Delta q^2(t)\cos^2(\phi_{\mathrm{LO}}) + \Delta p^2(t)\sin^2(\phi_{\mathrm{LO}})) \tag{5.10}$$

The current variance (i.e. noise) follows the variance of the q and p quadratures amplified by the LO (more details in Sec. 5.4). For coherent states, such as the LO, the detectors

see a photocurrent variance around shot noise, or zero fluctuations, where squeezed states will yield detector measurements of reduced noise in one quadrature. Using the PZT, the phase between the LO and squeezed signal is modified such that the minimum variance (squeezed quadrature), maximum variance (antisqueezed quadrature), and variances in between can all be measured.

5.3 Phase Reference of the Local Oscillator

A local oscillator (LO) is used to strategically select the squeezed signal and is shown in Fig. 5.1d. However, as various modifications are made to the LO (for further details see Sec. 5.4) it becomes important to know what the initial LO phase was in order to know what the modified LO phase is by eliminating any environmental contaminants. Thus, we introduce a second laser to use as a reference beam for the LO, as shown in 5.1b. As this reference beam does not experience any of the modifications placed on the LO, its phase remains the same as the initial LO phase and is considered a phase-locking mechanism. The reference and LO counter-propagate through the same arm of an interferometer (Fig. 5.1c) and experience optical elements in the same manner, except for one exception - the spatial light modulator (SLM) as shown in Fig. 5.1d. The SLM does the LO modifications and is further discussed in Sec. 5.4. The SLM is sensitive only to horizontal polarizations and acts as a mirror on any incoming vertical polarizations. We set the LO to be horizontally polarized when it interacts with the SLM while ensuring the reference beam is vertically polarized and is not altered by any SLM modifications. Both LO and reference are detected and the phase difference between them yields the true phase from the SLM modification.

5.4 Shaping the Local Oscillator

We continue discussions of the local oscillator and leave details of the use of the signal beam to Sec. 5.2. The local oscillator highlights the signal beam where the two beams overlap, a classical and well-studied process [76, 92]. The spatial overlap ($\mathcal{O}$) of the LO field (u_{LO}) and signal field (u_{sig}) is generally described as

$$\mathcal{O} = \int_{\mathrm{A}} (u^*_{\mathrm{LO}} u_{\mathrm{sig}})\, dA \tag{5.11}$$

over some area of detection A [18]. By controlling the overlap, we determine how we interact and measure a particular mode of the signal beam. The differential homodyne signal (Eq. 5.10) comes from the overlap of the signal with each masked LO. Essentially, shaping the LO controls how we interact with a particular mode in the signal. In our case, this interaction means we are measuring the quadrature projection in the overlap of a particular mode shape.

Many texts start with the assumption that the LO and signal beam are perfectly overlapped and in the same spatial mode, permitting an optimal detection scheme. However, perfect overlap of the LO and signals' spatial modes is experimentally unlikely and certainly untrue in our case, even in the best of times.

We strategically spatially modify the LO since we cannot well overlap with every mode. The idea can first be easily visualized by breaking the spatial area of the LO into smaller pixel sizes. By turning the pixels "on" one at a time, we can measure the variance of the quadrature projection in that particular pixel, as illustrated in Fig. 5.5. Each pixel's measurement is combined to create a covariance matrix (Sec. 2.6).

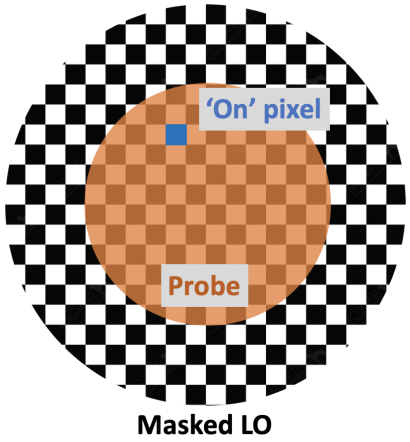

FIG. 5.5: A large local oscillator is masked with a single "on" pixel (blue), used to highlight a smaller and weaker signal beam (orange)

5.4.1 Single Pixel Imaging

Single-pixel imaging (SPI) is a technique that reconstructs images by measuring the intensity of light from a scene with a single-pixel detector, using a sequence of structured illumination patterns and computational algorithms. SPI is an established method for amplitude-based image reconstruction [93].

In conventional single-pixel imaging (SPI) systems, structured detection forms the core methodology: a light source illuminates a scene, and reflected light is collected through spatial basis patterns H_i before being measured as intensity weights w_i with a photodiode [93]. Scene reconstruction follows the linear combination Image $= \Sigma_i w_i H_i$, effectively mapping intensity pixel by pixel.

In our work, we extend this framework by implementing single-pixel homodyne imaging, which merges the structured detection strategy of SPI with the phase-sensitive measurement capabilities of homodyne detection. This hybrid approach eliminates the dependence on uniform reference fields and enables the reconstruction of arbitrary spatial modes, including both amplitude and phase information. The number of required measurements scales with the square of the image resolution, that is, n^2 for an n-pixel image. As we will

discuss further in Ch. 7, practical implementations may require even more measurements, highlighting the importance of optimizing experimental protocols.

5.4.2 Masking of the Local Oscillator

Any sampling basis can be used for classical field profile recovery. We select to use Hadamard matrices as our sampling basis as Hadamard matrices experimentally permit at least 50% of the laser power to diffract into the 0^{th} order of the SLM grating. In a raster scan, only one pixel at a time is used, significantly reducing the laser power that reaches our detector. Later on, we will need to follow a raster sampling procedure and the limitations will be discussed in Ch. 7. For now we continue with applying Hadamard masks to the LO.

Hadamard matrices are square matrices whose rows are mutually orthogonal. The elements of the matrix are ± 1 such that each column can be reshaped into a mask that we then apply to the LO. Note experimentally we cannot produce a -1 mask and instead take two mask measurements, one of the $+1$ mask components and one of the -1 components, and then take the difference [18, 2, 65].Although in theory we only need n^2 measurements for an n-pixel image, in practice we take $2n^2$ Hadamard measurements.

As an example, this two mask measurement process is demonstrated as:

$$Mask_{1m} - Mask_{2_m} = Hadamard_m \tag{5.12a}$$

$$\begin{pmatrix} 1 & 0 \\ 0 & 1 \end{pmatrix} - \begin{pmatrix} 0 & 1 \\ 1 & 0 \end{pmatrix} = \begin{pmatrix} 1 & -1 \\ -1 & 1 \end{pmatrix} \tag{5.12b}$$

for the m^{th} Hadamard mask and is done for M Hadamards. Through this process, we use at least half of the laser power (noted by the 1 elements), unlike in a raster scan where

one pixel at a time is used.

5.4.3 Spatial Light Modulator (SLM)

As the signal mode shape is unknown, we strategically select the spatial modifications placed onto the LO to be specialized bases sets to highlight the squeezed signal. Experimentally this is done with a Meadowlark Spatial Light Modulator (SLM) as shown in Fig. 5.1d such that the phase wavefront of the incoming LO is strategically modified. The SLM is a birefringent liquid crystal (LC) optoelectronic device that controls light properties across a beam's profile. The modulation patterns we apply to the LO are called masks. Specialized masks are applied to the LO via a phase blazed grating across the beam, which results in parts of the beam being deflected away from our detection path, or different diffraction orders. Adding a mask to the LO changes the LO's overlap with the squeezing signal, and thus modifies the noise variance measurement we make.

The SLM does not directly control the amplitude of the wavefront, only the phase. However, we require both amplitude and phase control of the LO to properly highlight the squeezed signal, as discussed in Subsec. 5.4.2. We use diffraction techniques to modify amplitude. Following the procedure outlined in [94], we are able to apply an equivalent of a phase and amplitude mask to the LO. Essentially, we encode the amplitude and phase of an optical field into a phase-only input, permitting exact control of spatial transverse fields. We use a grating pattern, whose diffraction efficiency is modified depending on the phase depth of the applied mask.

We define an optical field by two independent functions, one for the amplitude profile and one for the phase distribution, such that each function can be decomposed into their plane wave components. Each field then undergoes a Fourier transformation such that the amplitude's function acts as varying phase delays to the SLM output [94].

The surface of the SLM is broken up into 512×512 pixels, theoretically limiting the resolution of our reconstructions. As we are using bases sets of masks, the number of modes we can reconstruct is equal to the number of pixels, which, although seems like it should be 512^2, is much less. The blazed grating pattern uses multiple pixels per grating, significantly reducing the super-pixel count available for reconstructions. For example, a blazed grating made of 5×5 pixels will result in a 102×102 super-pixel region. We will later discuss additional experimental limiting factors to the number of modes we are able to reconstruct in Ch. 7.

Although the SLM is not our limiting factor when it comes to the amount of modes reconstructed, it does have a larger effect on the data acquisition time. It takes the SLM about 0.4 seconds to fully update its mask. Fig. 5.6 shows the response time of the SLM as it changes from one mask to another and shown in the blue curve. We are utilizing the 0^{th} order diffraction grating so an "off" pixel simply means all of the light is sent away from the 0^{th} diffraction order to other orders while an "on" pixel means all the light is reflected into the 0^{th} order.

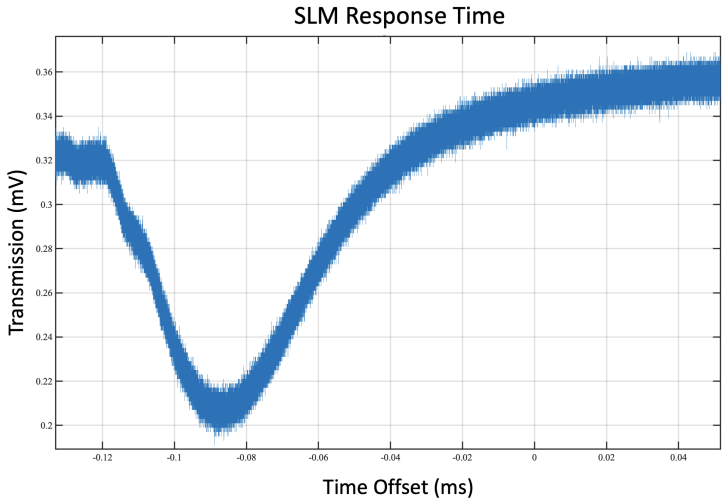

FIG. 5.6: SLM response time as a new mask is applied. *Adapted with permission from Nic DeStefano, 2025*

Note there is still some signal in the "all off", or dark mask. This is due to the diffraction order we are using, 0^{th} as there is some "bleed through" where some "off" pixels still reflect some light into the 0^{th} order. The 1^{st} order diffraction is actually more efficient as there is no "bleed through" from any "off" pixels and is typically the order used in experimental procedures [94, 95]. However, most of the incoming light intensity diffracts into the 0^{th} order, compared to the 1^{st} orders and beyond. As noted before, the LO is very power-starved so we must use the order with more intensity, the 0^{th}. The SLM is calibrated such that the 0^{th} order responds appropriately.

CHAPTER 6

Classical Field and Image Reconstruction

This chapter is based on a previously published paper [2].

We verify our reconstruction method by first imaging classical objects. As the objects are originally known, we are able to easily certify their reconstructions. By collecting the overlap values of each SLM Hadamard basis mask, as shown in Fig. 7.1, we find the full wavefront product described as, $S = u^*_{LO} u_{sig}$. The overlap of the LO and the signal probe per each Hadamard mask is described as

$$\mathcal{O}_m = \sum_n u^*_{LO}(n) u_{in}(n) H_m(n) \tag{6.1}$$

for n pixels. When the masked LO has a strong overlap with the input field, the differential signal will increase, as shown in Eq. 5.10 [96]. Experimentally, we sweep through all LO phases and fit the measured differential current with a generalized cosine function:

$$i_d(\phi_m) = |\mathcal{O}_m| cos(\omega_{PZT} + \phi_m) \tag{6.2}$$

for M total masks where ω is the frequency of the PZT sweep, 5 Hz. As in single pixel imaging, full wavefront is reconstructed as

$$\mathcal{S}(p) = \frac{1}{\mathrm{M}} \sum_{\mathrm{m}=1}^{\mathrm{M}} |\mathcal{O}_m| e^{i\Delta\phi_m} H_{\mathrm{m}}(p). \tag{6.3}$$

where p is the pixel of the Hadamard mask, H_m is the Hadamard mode, $\mathcal{O}_m$ is the overlap between the LO and probe field, and $\Delta\phi_m$ is the relative phase of the shaped LO and probe field [2].

As discussed in our publication, [2], this reconstruction method is compatible with compressive sensing techniques which would reduce the number of mask variance measurements we would need in total, as masks that would minimally contribute to the final reconstruction are simply skipped, leaving only heavily weighted measurements [97, 98, 99, 100, 101] .

While working with classical objects that are manually inserted into the signal beam, we need to account for background transmissions and our reconstructions are made of the ratio of the classical object's transmissions and the transmissions of the empty beam profile as

$$T(p) = \frac{\mathcal{S}_{\mathrm{obj}}(p)}{\mathcal{S}_{\mathrm{ref}}(p)}. \tag{6.4}$$

The resolution of minute variations in complex transmission systems faces inherent limitations rooted in the noise characteristics of differential photocurrents, as quantified by Eq. (4). Under ideal conditions using coherent-state laser fields, shot noise from the probe beam dictates the fundamental noise floor, which scales inversely with the square root of the detected photon count. While this relationship suggests sensitivity improvements through increased probe beam intensity, real-world systems encounter practical constraints that often dominate performance. Phase fluctuations and intensity instabilities in laser

sources frequently exceed theoretical shot noise levels, creating operational limits that cannot be overcome through brightness enhancement alone.

Measurement accuracy further depends critically on the stability of local oscillator (LO) parameters, as probe beam characteristics are intrinsically referenced against this benchmark. Any drift or instability in the LO directly propagates through the measurement chain, introducing systematic errors that compromise precision.

Spatial reconstruction capabilities face separate constraints tied to optical system performance. Imperfections in Hadamard mask implementations combine with unavoidable diffraction effects in imaging optics to establish ultimate limits on reconstruction fidelity. These dual challenges, noise related detection limits and optical system imperfections, collectively define the practical boundaries of achievable resolution in complex transmission measurements.

To demonstrate the phase sensitivity of our method, we choose to reconstruct several transparent objects with variable optical depths (see Fig. 6.1). The background of each object reconstruction is removed by dividing out an empty beam profile from the object, resulting in phase and amplitude transmission profiles (Eq. 6.4). For visual convenience, the dark pixels, or edge pixels are not included due to their high level of noise. Instead, the boundary of illuminated pixels are simply cropped out.

The top row of Fig. 6.1 shows experimentally reconstructed images of a dried drop of hand sanitizer on a glass plate after the water has evaporated. Fig. 6.1a shows a camera reference of the sanitizer object, Fig. 6.1d shows our phase reconstruction, and Fig. 6.1g shows our amplitude reconstruction. The camera and amplitude reconstruction look fairly similar to one another, as expected. The phase reconstruction of the sanitizer drop also shows the boundary of the drop, but begins to highlight the more uniform center of the drop, compared to the nosier pixels that were just reconstructing the surface of the glass plate. The surface difference is not as apparent with just the camera.

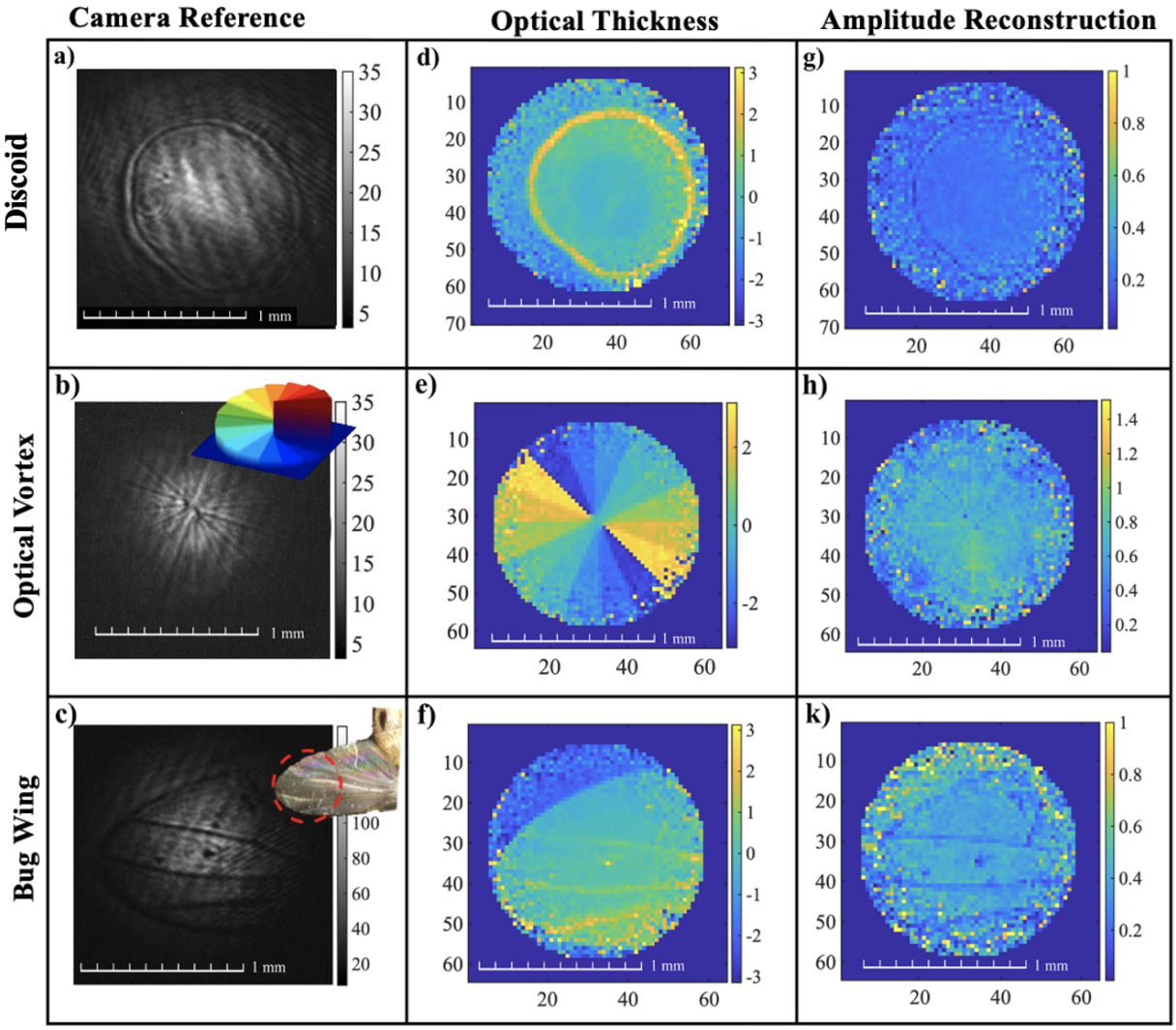

FIG. 6.1: a) The camera reference of a dried discoid of hand sanitizer on a glass plate. b) The camera reference of an optical vortex. The inlay shows a $3D$ cartoon of the vortex's different sectors of depth. c) The camera reference of a translucent bug wing, The inlay shows the bug wing's image taken with a standard microscope. d) The phase reconstruction of the discoid. e) The phase reconstruction of the vortex. f) The phase reconstruction of the bug wing. g) The amplitude reconstruction of the discoid. h) The amplitude reconstruction of the vortex. k) The amplitude reconstruction of the bug wing

The middle row of Fig. 6.1 shows experimentally reconstructed images of an optical vortex mask which is a glass plate with sector-wise variable thickness spanning $850nm$ (Fig. 6.1(e,h)). The inlay of Fig. 6.1b shows a cartoon example of a side view of a vortex where it becomes clear each sector has a different thickness. In our phase transmission reconstruction (Fig. 6.1e), we observe clear phase steps corresponding to the sectors of the phase plate. Notice that no such information is available in the direct camera image (Fig. 6.1b), which is sensitive only to changes in intensity. As expected, the amplitude transmission reconstruction shows a flat profile with an approximate transmission of 1 (Fig. 6.1h). Due to the noise around the edges of the beam, the maximum transmission is scaled larger than 1.

The bottom row of Fig. 6.1 shows c) a camera image of a bug wing with an inlay of a microscopic image of the wing, f) the wing's phase reconstruction, and k) the wing's amplitude reconstruction. Although most of the detail of the wing, such as the veins, is present in the camera and amplitude images, the phase reconstruction is included for completeness.

To evaluate the depth resolution of our phase transmission reconstructions in a qualitative manner, we take multiple data sets of the drop of sanitizer as shown in Fig. 6.2. A Bruker Dektak Surface Profiler employs a diamond-tip stylus to scan the surface of the discoid, measuring height variations between the ridge boundaries and revealing a crater-like depth profile in Fig. 6.2b. Fig. 6.2a shows the path of the diamond-tip which produces a cross section with a vertical resolution of 0.1 nm. The Bruker Profiler operates with a 2 µm stylus tip and 3 mg force, completing 2 mm scans in 20 seconds as part of its standard protocol. Multiple reconstructions of the phase transmission (Fig. 6.2c) are performed, with a corresponding cross-sectional profile (Fig. 6.2d) extracted across the crater-shaped morphology. Variability in the phase transmission reconstruction stems from the statistical analysis of repeated runs. Despite slight differences in cross-sectional comparisons of

the microscope image and reconstructed phase, the overall discoid geometry and boundary positions remain consistent [2].

Based on multiple data sets of discoid phase reconstruction (Fig. 6.1c) the experimental phase reconstruction uncertainty is ± 0.02 radians in the center of the image where the LO is strongest. We can reconstruct the amplitude of transmission with a statistical uncertainty of ± 0.01. We achieve spatial reconstructions at a resolution of 64×64 pixels, where each pixel corresponds to a physical dimension of $26 \pm 2\mu$m [2].

As we have now successfully reconstructed known classical objects, we next move on to our object of interest - squeezed light.

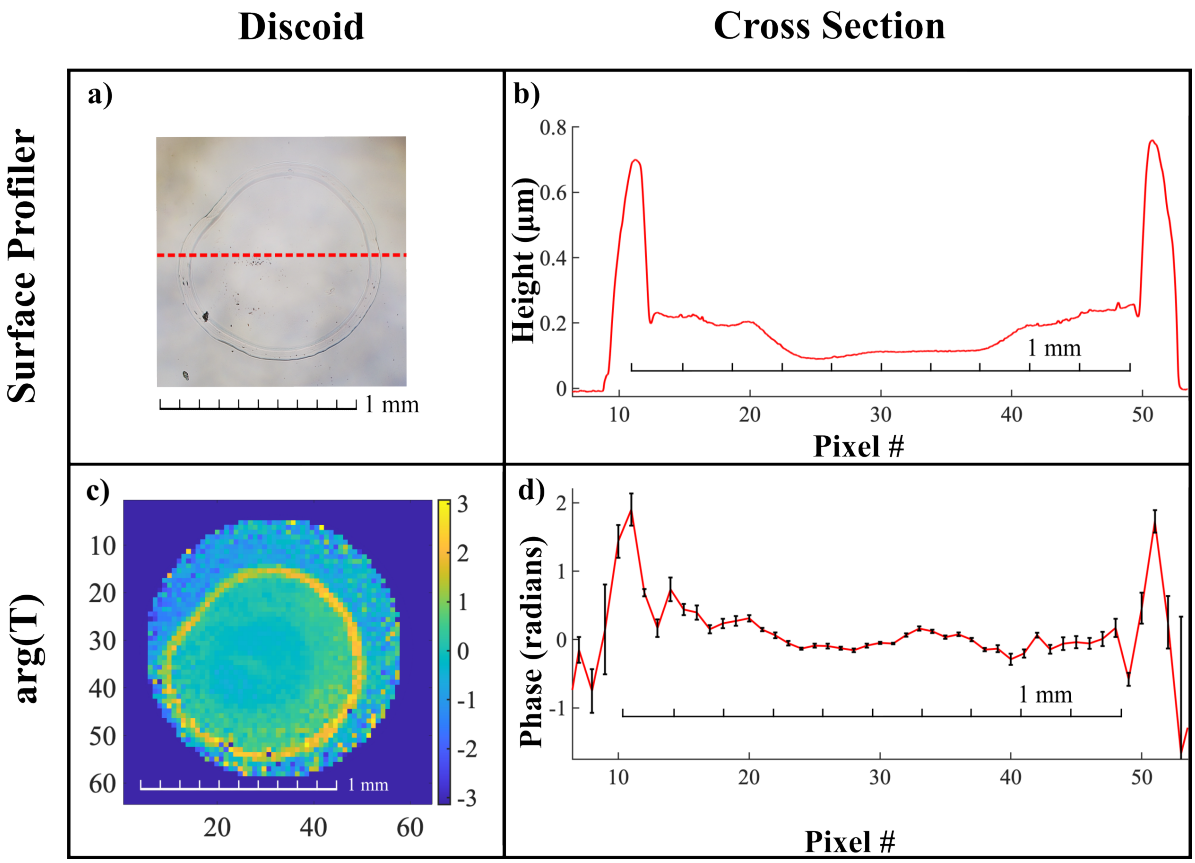

FIG. 6.2: a) A HIROX microscope system image of the discoid, after the alcohol evaporated, taken in mid-range at x140 (field of view is 2169.05μm with a resolution of 1.13 μm). The horizontal dashed red line indicates the approximate b) cross-section taken with a Bruker Dektak Surface Profiler. The vertical uncertainty is 0.1 nm. c) The phase profile of the discoid outlines the ridge and crater-like shape that is physically present. d) A similar cross-section of our phase reconstruction is qualitatively compared to the Bruker Dektak Profiler cross-section. The edges have a larger uncertainty, which is attributed to the minimal light at the edges of the beam as the signal-to-noise ratio decreases. Reprinted with permission from Cuozzo et al., Wave-front reconstruction via single-pixel homodyne imaging, Opt. Express 30, 37938 (2022). © Optica Publishing Group.

CHAPTER 7

Quantum Mode Reconstructions

We expand on the experimental outline of Ch. 5 and reconstruct quantum modes rather than classical objects. First we demonstrate reconstructions with the assumption that there is one single mode and one contaminating thermal mode. From there, we generalize our reconstruction scheme to account for any potential modes. Lastly, we characterize the general scheme and verify acceptable noise levels of the experimental system.

7.1 Two Mode Assumption

This section is based on the published paper [65].

Using the same experimental setup in Ch. 5, we make the initial assumption that there is one single squeezed mode and one single thermal mode present in our system. The mode assumption permits us to make mathematical simplifications such that $\Sigma_o = \Sigma_d$ where the off-diagonal elements of the measured covariance matrix (Σ_o) are zero.

The overlap (Eq. 5.11) relates to the spatial mode shapes as

$$\mathcal{O}_{km} = \int_{A_d} u^*_{LO}(x,y) u_k(x,y) H_m(x,y) dxdy \tag{7.1}$$

where A_d is the detector area, $u^*_{LO}(x,y)$ is the local oscillator field, $u_k(x,y)$ is the signal field, and $H_m(x,y)$ is the m^{th} Hadamard mask.

The single squeezed and single thermal mode covariance matrix takes the form shown in Eq. 3.4. This can be generalized as

$$\begin{aligned} diag(\Sigma(\theta))_m = 1 + |\mathcal{O}_{th_m}|^2 (v_{th} - 1) + \\ + |\mathcal{O}_{sq_m}|^2 \left(v^+ \cos^2(\theta - \theta_m) + v^- \sin^2(\theta - \theta_m) - 1 \right) \end{aligned} \tag{7.2}$$

where we identify v^+ as the maximum variance and v^- as the minimum variance of mask m as shown in Fig. 7.1 for various masks where fits are done with Eq. 6.2. This makes the assumption that the mixed noiseball we measure is oriented as the inlay of Fig. 7.1, or has a rotation angle $\theta = 0$. With the assumption that each measurement aligns the noiseball as so, we measure the maximum variance, minimum variance, and track θ_m per each Hadamard mask.

The overlap of the squeezed mode can be determined as

$$\mathcal{O}_{sq_m} \propto e^{i\theta_m} \sqrt{V^+_m - V^-_m}. \tag{7.3}$$

If we assume that the thermal mode is much noisier than shot noise ($v_{th} \gg 1$), and consequently, the thermal mode variance is much larger than squeezed quadrature variance

$(v_{th} \gg v^{-})$, we can approximate

$$|\mathcal{O}_{th_m}|^2 \approx V_m^- \tag{7.4}$$

such that the thermal mode reconstruction is not dependent on θ.

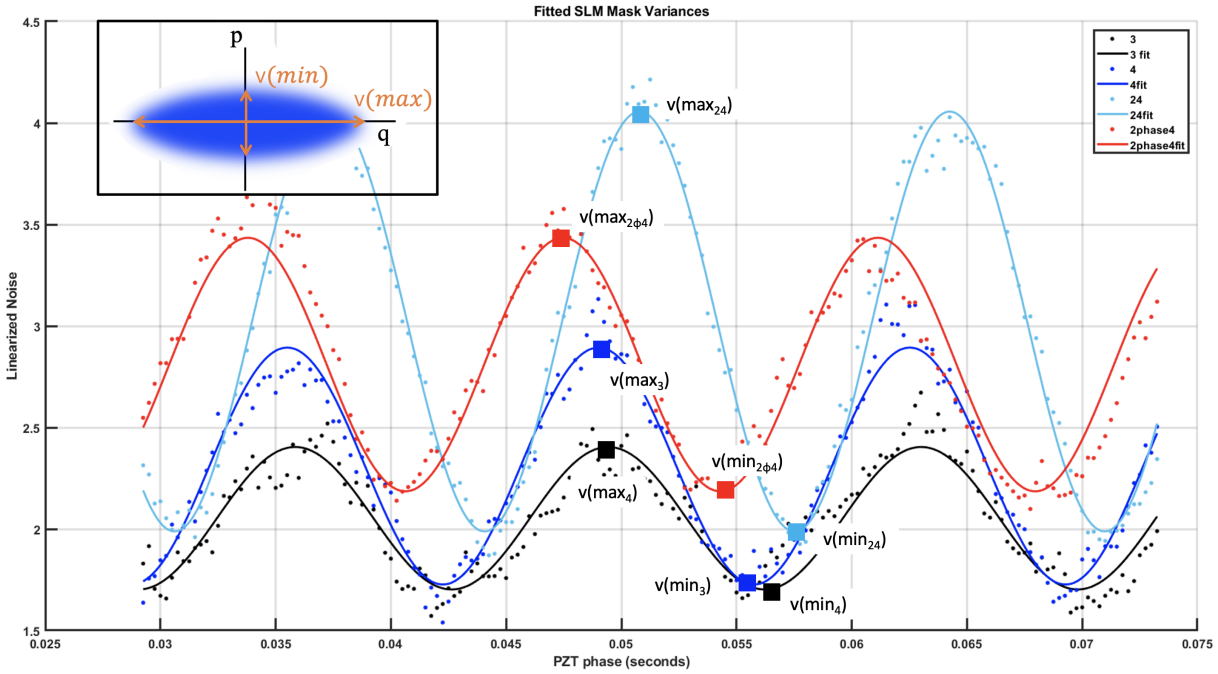

FIG. 7.1: Quadrature variance traces for a single pixel mask (black), another single pixel mask (dark blue), a two pixel mask (light blue), and a two pixel mask with a phase shift between the pixels (red). Each trace's maximum and minimum variances are noted with squares.

7.1.1 Single Mode Reconstructions

We use Eq. 7.3 to reconstruct the shaped squeezed field amplitude and phase (Fig. 7.2a,b and Fig. 7.3a,b) and Eq. 7.4 to reconstruct the thermal field (Fig. 7.2c and Fig. 7.2c).

The last column of Fig. 7.2 and Fig. 7.3 shows the classical reconstruction [2] using a small leakage of the classical LO field into the squeezing polarization due to the limited extinction ratio of the polarizing beam displacer. At lower temperatures, corresponding to

reduced atomic density and weaker nonlinear effects responsible for squeezing and output mode structure [102], the reconstruction at 65°C (Fig. 7.2) reveals a distinct fundamental Gaussian beam shape in both classical (Fig. 7.2d,e) and quantum (Fig. 7.2a,b) reconstructions. This aligns with expectations, as squeezing occurs in a mode closely resembling the LO used to pump the squeezer [103, 104, 105, 102, 106]. At 65°C, -2.0 dB of squeezing (noise suppression relative to shot noise) is observed directly from the Rb cell. Optical losses in polarizers and SLM reflections reduce this to -0.5 dB at the detector, while 5.7 dB of antisqueezing suggests thermal noise influence. Though the thermal mode's spatial profile remains unpredictable, its overlap with the squeezed vacuum is inferred from noise degradation [105, 102], a hypothesis supported by measured thermal mode profiles.

Increasing the Rb cell temperature to 80°C enhances atomic density but eliminates measurable squeezing. The minimum noise rises to 2.7 dB above shot noise due to thermal mode dominance, while maximum noise reaches 11.5 dB after imaging optics. Spatial mode changes become evident in both classical and quantum reconstructions (Fig. 7.3). The classical overlap reconstruction (Fig. 7.3e) develops an additional "ring," likely from laser self-defocusing in hotter vapor. Quantum reconstructions (Fig. 7.3a,b) display modified Gaussians with digital "boxiness" artifacts sensitive to post-processing phase choices. The phase-independent thermal mode reconstruction (Fig. 7.3c) exhibits a two-lobe structure, faintly visible even at 65°C (Fig. 7.2c).

The reconstructed field magnitudes correlate with input squeezing and thermal variances, as Eqs. 7.3 and 7.4 omit normalization by $\sqrt{V^+ - V^-}$ and V_{th}. This reveals that higher atomic densities generate noisier fields with greater input variance, consistent with the observed temperature-dependent noise escalation.

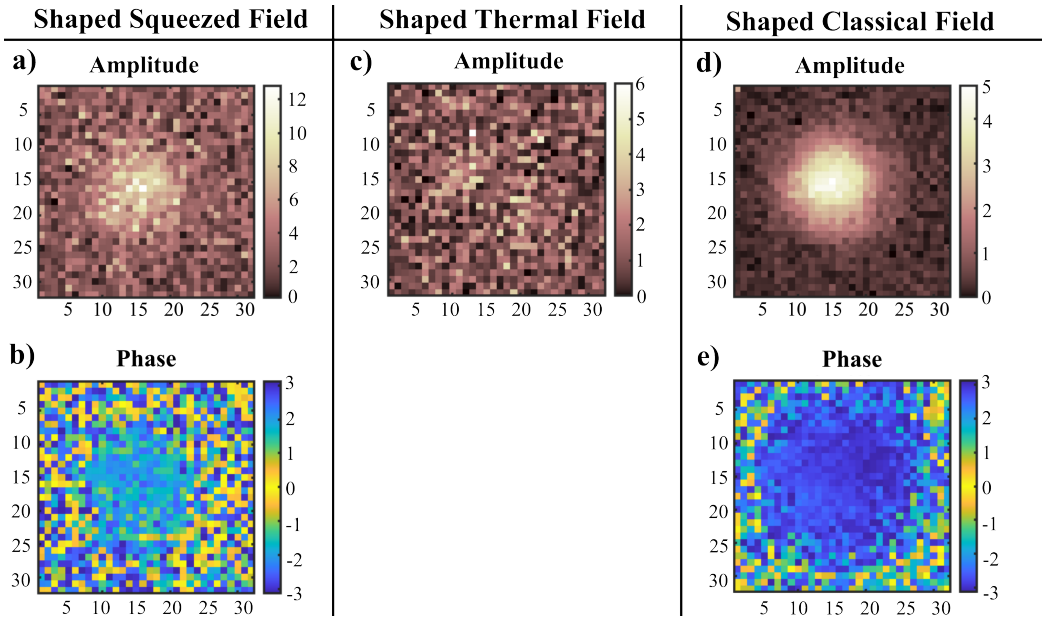

FIG. 7.2: A low temperature reconstruction (65^{o}C) where a) is the amplitude of the shaped squeezed field b) is the squeezed phase c) is the amplitude of the shaped thermal field and d) and e) are the amplitude of the shaped classical field and phase reconstructions respectively. Classical field images (recovered with methods described in [2]) are included to provide comparison. Phase colorbars are in radians. Quantum fields amplitude colorbars are proportional to the square root of quantum noise variance. *Reproduced from C. Gabaldon et al., AVS Quantum Sci. 5, 025005 (2023), with the permission of AIP Publishing*

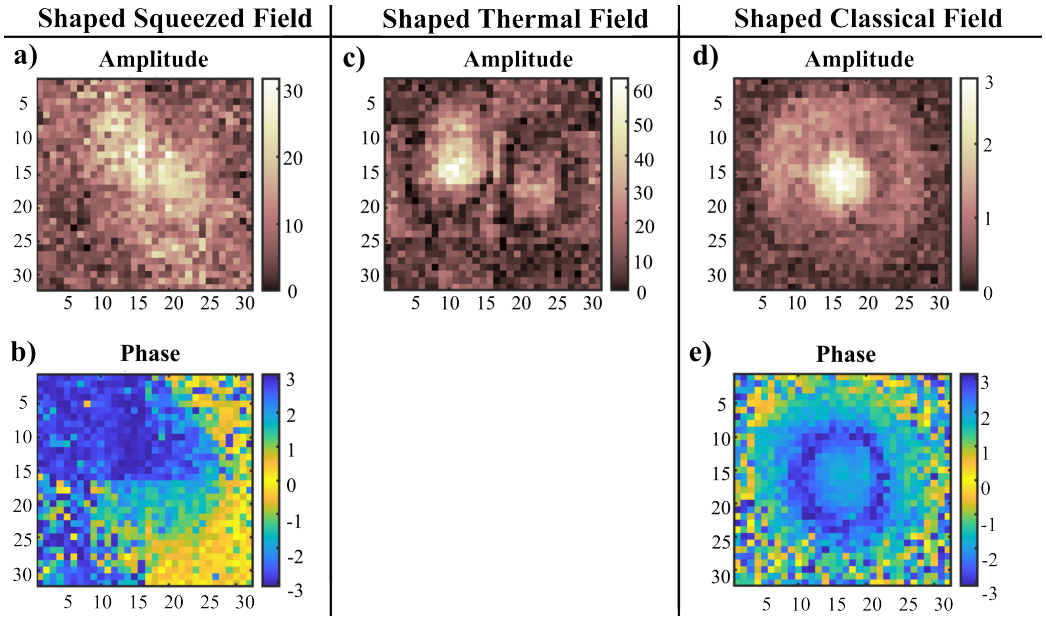

FIG. 7.3: A high temperature reconstruction (80^{o}C) where a) is the amplitude of the shaped squeezed field b) is the squeezed phase c) is the amplitude of the shaped thermal field and d) and e) are the amplitude of the shaped classical field and phase reconstructions respectively. Classical field images (recovered with methods described in [2]) are included to provide comparison. Note the thermal shape difference (c) compared to Fig. 7.2c. Phase colorbars are in radians. Quantum fields amplitude colorbars are proportional to the square root of quantum noise variance. *Reproduced from C. Gabaldon et al., AVS Quantum Sci. 5, 025005 (2023), with the permission of AIP Publishing*

7.1.2 Thermal Field Reconstruction Comparisons

This last topic of Sec. 7.1 builds upon the published paper [65], although it was not included in the published version.

We additionally verify that we are able to reconstruct the thermal field amplitude under various experimental settings in Fig. 7.5. By increasing atomic density via changing the surrounding temperature of the rubidium cell, we expect antisqueezing to exponentially dominate the system, as shown in Fig. 7.4. In our system, the red circled region of Fig. 7.4 finds the most squeezing at 65°C.

We first show the amplitude of the thermal field under experimental conditions that best produce squeezing, 65°C. As temperature is increased in Figs. 7.5b-g we see the

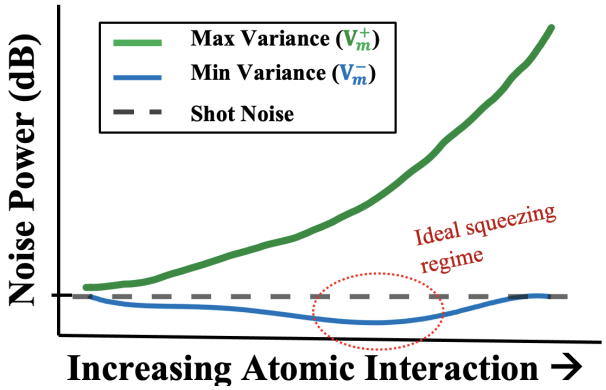

FIG. 7.4: Levels of squeezing and antisqueezing at varying temperatures *Adapted from "Experimental Generation and Manipulation of Quantum Squeezed Vacuum via Polarization Self-Rotation in Rb Vapor," by Travis S. Horrom, College of William and Mary, 2013* [1]

expansion of the thermal field amplitude (note the different colorbar limits) until a two-lobe shape appears in Fig. 7.5h at 80°C. Some change was expected at higher temperatures as antisqueezing values exponentially dominate at higher atomic densities. The two-lobe thermal field amplitude is stressed even more in the 80°C reconstruction shown in Fig. 7.5i.

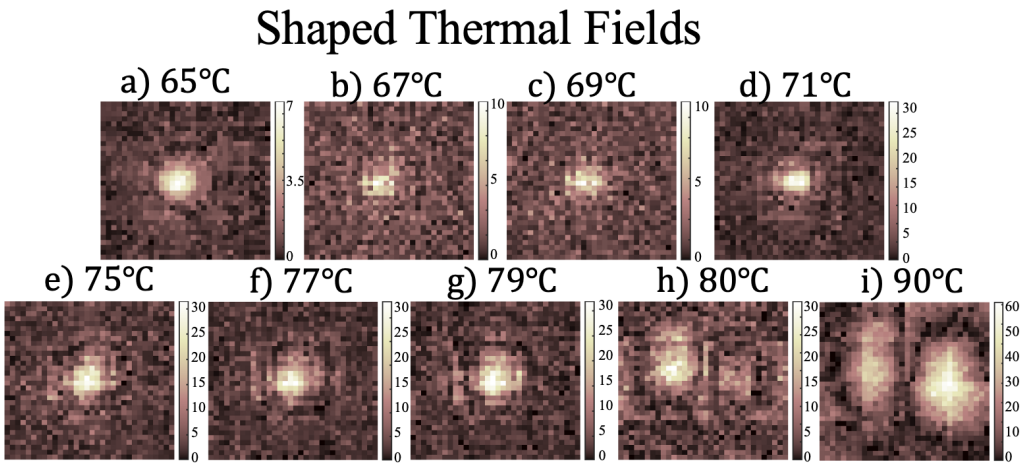

FIG. 7.5: Reconstructions of the amplitudes of the thermal field done at temperatures a) 65°C, b) 67°C, c) 69°C, d) 71°C, e) 75°C, f) 77°C, g) 79°C, h) 80°C, and i) 90°C.

7.2 Generalized Quadrature LO Masking

If we avoid presuming specific individual modes within the system, we must discard the assumption of a diagonalized covariance matrix and instead adopt a raster mask imaging approach. This framework relies fundamentally on the premise of multimode squeezing.

Although Fig. 5.5 shows us how one pixel is used at a time, there is a bit more work that goes into creating the full covariance matrix. Recall the covariance is made up of the quadrature projections of axes q and p per each basis measurement, or pixel in our case. Not only do we need a single quadrature projection variance ($v(q)$) but we also need its orthogonal counterpart ($v(p)$) and combination of both ($v(q+p)$) per each pixel. We then need to compare how q and p quadratures from each pixel interact with quadratures q and p from every other pixel via the covariance matrix. As the number of pixels used in the total reconstruction grows, the number of required measurements quadratically grows. Unlike in our classical and single mode reconstructions, our number of measurements scales with covariance size as $(2n)^2$. But note, this can be done with non-square matrices whereas Hadamard masks were square by definition.

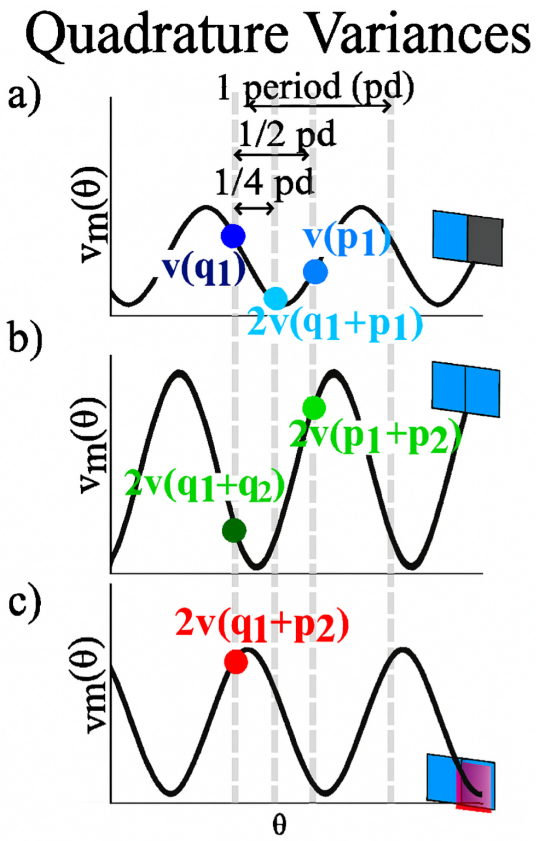

FIG. 7.6: Three types of LO masks are used to gather all needed variance measurements. Here we show an example of masks used in a two pixel reconstruction where θ is the repeated PZT sweep. a) A single pixel where pixel 1's q and p quadrature projects are measured, $v(q_1)$ and $v(p_1)$, respectively. Note pixel 2 is measured similarly to collect $v(q_2)$ and $v(p_2)$. b) Two pixels are used to collect variance combinations $v(q_1 + q_2)$ and $v(p_1 + p_2)$. c) Two pixels where pixel 2 has a $\frac{\pi}{2}$ mask phase difference compared to pixel 1. This LO mask measures $v(q_1 + p_2)$. Applying the $\frac{\pi}{2}$ mask phase shift to pixel 1 instead of pixel 2 yields the projection measurement of $v(q_2 + p_1)$.

In order to obtain all of these types of variances, there are three types of LO masks used per every two pixels, as shown for a two pixel ($n = 2$) example in Fig. 7.6; a single pixel, two pixels, and two pixels with a phase difference. We simultaneously track a reference trace from the reference laser for every measurement taken and arbitrarily take the first $v(x_n)$ point where it aligns with the maximum peak of the reference trace. As no changes are made to the reference trace, we know the trace of the reference should not be changing and shift all mask measurements accordingly. In the previous classical and two mode

assumption reconstructions, we directly extracted a phase difference relative to a reference and incorporated this phase into our reconstruction. By contrast, our generalized method of directly shifting masks captures equivalent information through indirect processing, ensuring all masks remain mutually aligned as demonstrated in Fig. 7.6.

We first collect $v(q_1)$, $v(p_1)$, $\frac{1}{2}v(q_1+p_1)$ variances, and scan LO phase from turning pixel 1 on and leaving pixel 2 off as shown in Fig. 7.6a. $v(p_1)$ is half a period from $v(q_1)$, as rotating the noiseball by half a period results in the orthogonal projection to be on quadrature q. Similarly, $v(q_1+p_1)$ is measured a quarter period away from $v(q_1)$. This process is repeated for pixel 2 on and pixel 1 off resulting in variance measurements $v(q_2)$, $v(p_2)$, and $v(q_2+p_2)$. Fig. 7.6b has both pixels 1 and 2 on where $v(q_1+q_2)$ is measured at the same PZT sweep location as $v(x_n)$. A half period away we collect $v(p_1+p_2)$. The last type of mask we collect has both pixels on, but with a phase difference. Fig. 7.6c illustrates pixel 1 on and pixel 2 on with a $\frac{\pi}{2}$ phase mask placed via the SLM such that we measure $v(q_1+p_2)$ at the same start point as $v(x_n)$. Then the $\frac{\pi}{2}$ phase mask is placed on pixel 1 compared to pixel 2 permitting us to collect $v(q_2+p_1)$.

Once all variance measurements are made, they are combined into an experimental covariance matrix shown in Fig. 7.8a. The elements of the covariance follow Eq. 2.14 and combine as

$$c(q_m,p_m)=\frac{1}{2}[v(q_m+p_m)-v(q_m)-v(p_m)] \tag{7.5a}$$

$$c(q_m,q_n)=\frac{1}{2}[v(q_m+q_n)-v(q_m)-v(q_n)] \tag{7.5b}$$

$$c(p_m,p_n)=\frac{1}{2}[v(p_m+q_n)-v(p_m)-v(p_n)] \tag{7.5c}$$

$$c(q_m,p_n)=\frac{1}{2}[v(q_m+p_n)-v(q_m)-v(p_n)] \tag{7.5d}$$

for two pixels m and n.

Fig. 7.7 shows a few examples of quadrature noise traces for $n=4$ pixels. Physically,

in the single pixel mask measurements we collect $v(\frac{q_m+p_m}{\sqrt{2}})$ and must multiply by a factor of 2 to find $v(q_m+p_m)$. The reconstruction results of the noise traces are shown in Fig. 7.8. Each mask trace is again fitted with Eq. 6.2. The dark blue trace shows the data of single pixel 4, its fit, $v(q_4)$, $v(p_4)$, and $v(q_4+p_4)$. The black trace comes from single pixel 3, where we similarly find its fit, $v(q_3)$, $v(p_3)$, and $v(q_3+p_3)$. The point where $v(q_3)$ is taken is offset by a period for visual convenience, but is actually taken at the same PZT sweep as $v(q_4+q_2)$, $v(q_4+p_2)$, and $v(q_4)$. The light blue trace comes from the double pixel mask of pixel 2 and 4. Here we find the fit of 2 and 4, $v(q_4+q_2)$ and $v(p_4+p_2)$. Lastly, we have the data and fit of double pixel mask 2 and 4 but where pixel 2 has a $\frac{\pi}{2}$ so we can collect $v(q_4+p_2)$. As expected, the red trace with its partial $\frac{\pi}{2}$ phase shift is almost half a period off from the light blue trace of double pixels 2 and 4. As it is highly unlikely that the LO and signal are perfectly centered on the four pixels, we can only approximate this effect from our raw data fits.

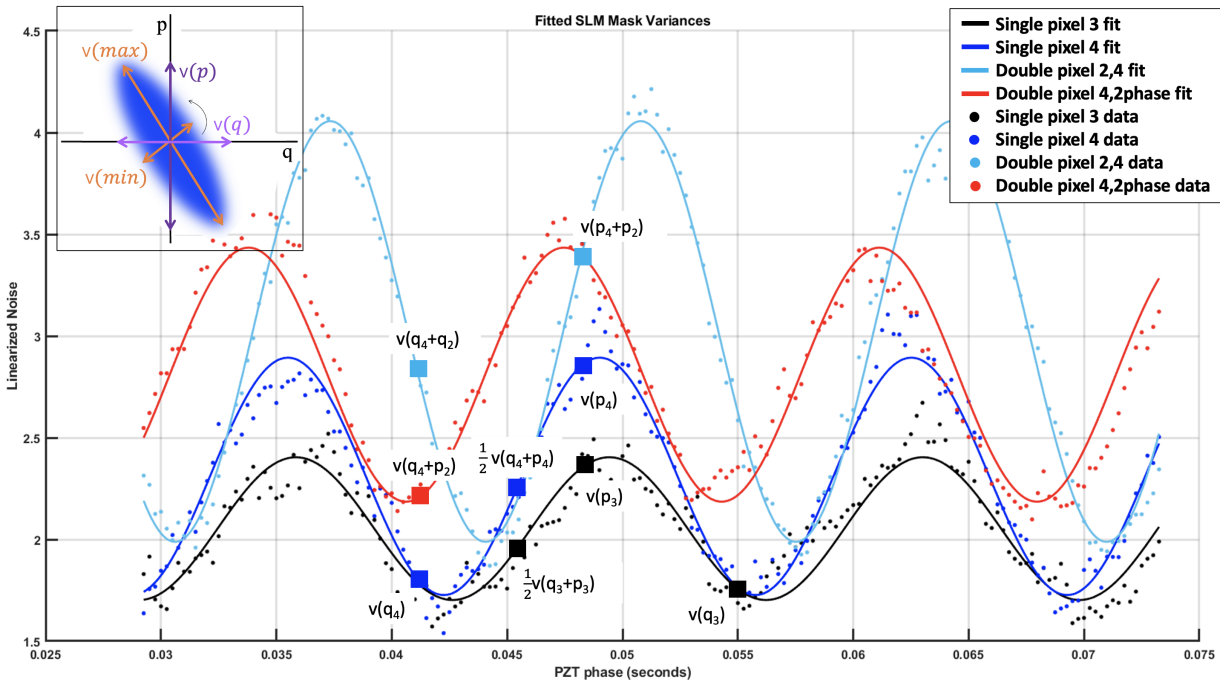

FIG. 7.7: The raw data and fits of single pixel 4 (dark blue), single pixel 3 (black), double pixels 4 and 2 (light blue), and double pixels 4 and 2 with a $\frac{\pi}{2}$ phase mask (red). Single pixel 3 traces collect $v(q_3)$, $v(p_3)$, and $\frac{1}{2}v(q_3+p_3)$ values. Single pixel 4 traces collect $v(q_4)$, $v(p_4)$, and $\frac{1}{2}v(q_4+p_4)$ values. Double pixels 4 and 2 collect $v(q_4+q_2)$ and $v(q_4+q_2)$ values. Double pixels 4 and 2 with a phase mask collect $v(q_4+p_2)$. The inlay shows the noiseball of the m^{th} mask at some arbitrary rotation.

7.3 Generalized Reconstruction

Although Fig. 7.6 demonstrated quadrature variance measurements with $n = 2$ pixels, this process can be expanded to more pixels. However, as we must now collect measurements from one pixel at a time, the measured light power will be significantly limited. Experimentally, we have only been able to reconstruct modes with a resolution of $n = 4$ pixels as that already limits the LO power to 25% and we are brought close to dark noise in several measurements. Further reducing single pixel measurements to a high pixel count will require more laser power.

We show our general reconstruction results in Fig. 7.8 for a $n = 4$ pixel mask in a 2×2 form. Fig. 7.8a is the covariance made out of the traces described in Sec. 7.2 and with a select few displayed in Fig. 7.8b. Note the raw data traces are a copy of Fig. 7.7, but placed next to the covariance matrix for convenience. Looking at the covariance diagonal, we see $v(q_3) = 1.72$, $v(p_3) = 2.39$, $v(q_4) = 1.79$, and $v(p_4) = 2.83$, which align with the black and dark blue fit traces in Fig. 7.8b, respectively.

By following Eq. 7.2, we can verify the covariance matrix element $c(q_3, p_3)$ as $c(q_3, p_3) = \frac{1}{2}[2v(\frac{q_3+p_3}{\sqrt{2}}) - v(q_3) - v(p_3)] \approx \frac{1}{2}[2(2.04) - 1.72 - 2.39] \approx -0.1$, aligning with what we see in the covariance matrix, in Fig. 7.8a. Note, as the covariance matrix is symmetric, we also see $c(p_3, q_3) \approx -0.1$.

Once the covariance matrix (Σ_o) is created, and verified, we send it through our decomposition process Sec. 4.2. Note the decomposition processes do not maintain pixel order, but display in order from the strongest mode to the weakest mode. Fig. 7.8c displays the Williamson Decomposition results, matrix D, where we see the first strongest mode is zero, or holds no thermal information, the second strongest mode holds some thermal information, $D(2) = 1.5$, and the weakest two modes have thermal information $D(3) = 2.13$ and $D(4) = 3.60$, respectively. Recall Williamson Decomposition produces matrix S, which we send through Bloch-Messiah Decomposition. Matrix Z from Bloch-Messiah Decomposition is shown in Fig. 7.8d and holds the squeezing information of each reconstructed mode. We see the most squeezed mode has $r_{Z(1)} = 0.63$ and squeezing lessens as the modes weaken such that we see $r_{Z(2)} = 0.80$, $r_{Z(3)} = 0.87$, and $r_{Z(4)} = 0.91$. The corresponding antisqueezing values are not displayed as they are simply values of $\frac{1}{r}$. Bloch-Messiah Decomposition also produces matrix O_1, which holds the spatial shape structures of the modes. By following the process outlined in Subsec. 4.2.2 we reconstruct four spatial modes, shown in Fig. 7.8e-h. Unlike in our simulation example, Sec. 4.3) our system has complex modes where we show the phase reconstruction portion of the modes in

Fig. 7.8 e.2-h.2. The amplitudes of the mode reconstructions are shown in Fig. 7.8 e.1-h.1.

As our reconstructions are limited to $n = 4$ pixels, the spatial mode reconstructions are uninteresting in this square 2×2 form. We will later demonstrate a more interesting case of striped pixels, taking a 4×1 form.

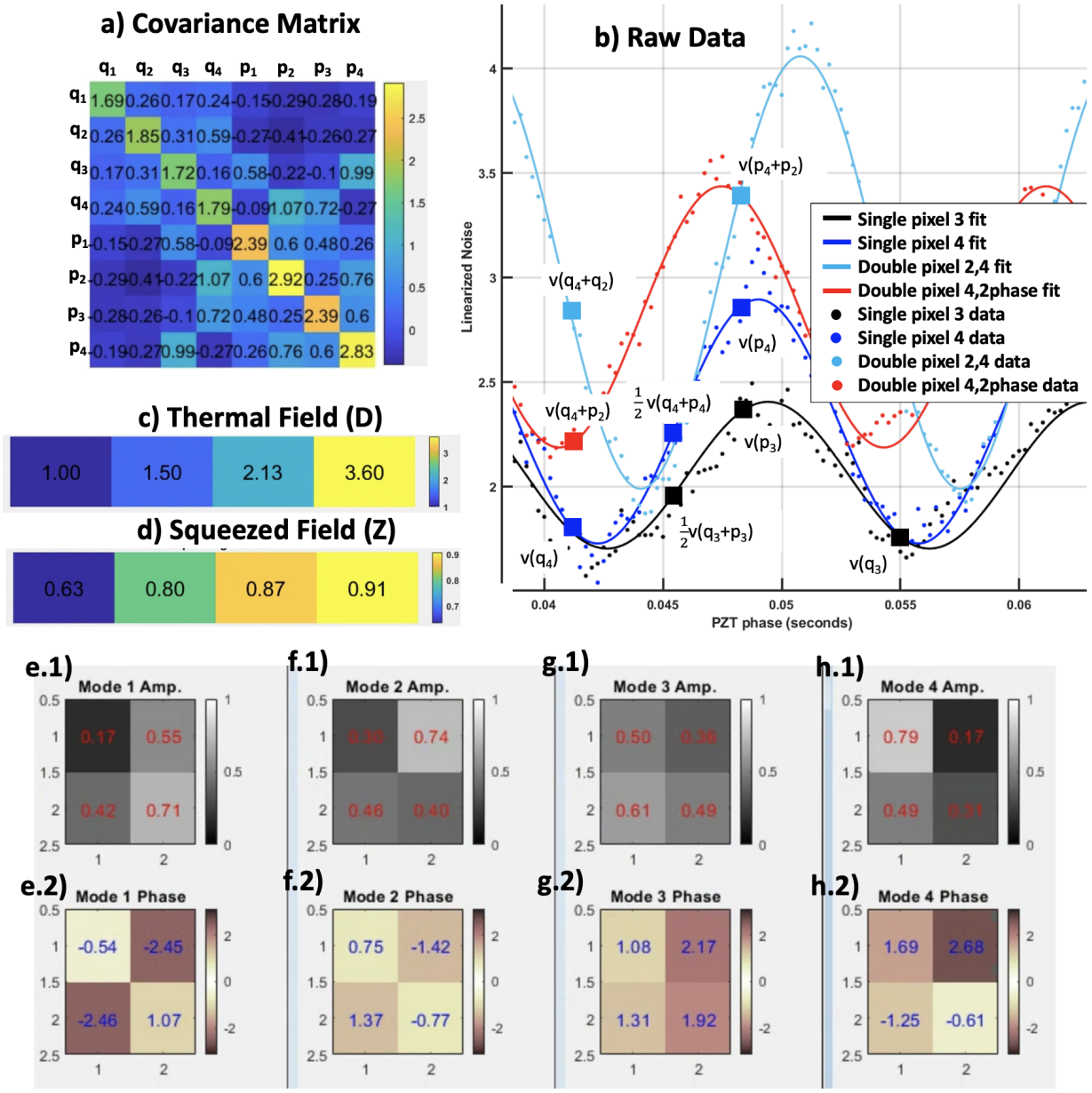

FIG. 7.8: A 2x2 pixel reconstruction run. a) The measured covariance matrix in $(q_1, q_2, q_3, q_4, p_1, p_2, p_3, p_4)$ order. b) Select mask traces plotted in PZT phase sweep verse linearized noise levels. c) Thermal field amplitude values of each reconstruction mode. d) Squeezed field parameter values of each reconstructed mode. e.1) Reconstructed amplitude of the first mode. e.2)Reconstructed phase of the first mode.f.1) Reconstructed amplitude of the second mode. f.2)Reconstructed phase of the second mode. g.1) Reconstructed amplitude of the third mode. g.2)Reconstructed phase of the third mode. h.1) Reconstructed amplitude of the fourth mode. h.2)Reconstructed phase of the fourth mode.

7.4 Shake Out of Covariance Matrix

As we move on from square masking techniques and reduce laser power per mask, compromised covariance matrices quickly emerge when approaching dark noise thresholds. This proximity to dark noise levels degrades the signal-to-noise ratio (SNR), causing matrix decomposition processes to yield non-physical results due to the corrupted covariance structure.

To address this, we have developed a "shake out" method that adjusts the measured covariance matrix to preserve the physicality of the parameters. The Shake Out modifies Σ_o to Σ_h Specifically, this approach aims to make minimal alterations to the original measured covariance so that minimal changes are made to Σ_o. The modified covariance from the shake out method is identified as h_{shape} (Eq. 7.6). We additionally need to uphold unitary propagation transformations h_{transf} (Eq. 7.7), and to ensure that any thermal states retain a realistic photon count.

We first ensure that the adjusted covariance matrix remains as faithful as possible to the actual experimental outcomes, thereby minimizing the introduction of artificial artifacts. This principle is essential because any unnecessary alteration to the measured data could obscure or distort the underlying physical phenomena we aim to study. The difference of the shake out covariance matrix is weighted as

$$h_{shape} = \frac{\sqrt{(\Sigma_o - \Sigma_h)^2}}{|\Sigma_o \Sigma_s|}. \tag{7.6}$$

The second shake out parameter still looks at the covariance matrix (Σ_o) directly and ensures that any linear transformations it underwent are physical. Recall any transformations should be unitary. We check this by verifying that all eigenvalues of the covariance

matrix are positive. Should there be one or more negative eigenvalues we collect them as

$$h_{transf} = \sum_{n} (eigenvalues < 0) \tag{7.7}$$

The shake-out process initially iterates through the first two criteria until both are satisfied. If the covariance matrix contains any negative eigenvalues, the decomposition will not succeed, and no results will be produced. This also results in the first two criteria being weighted equally as $\lambda_{shape} = 1$ and $\lambda_{transf} = 1$.

The last shake out parameter collects the diagonalized Williamson Decomposition thermal field values (D) as

$$h_w = (\sum_{n} [(D - 1) < 0])^2 \tag{7.8}$$

as thermal fields cannot have an average photon number less than 1 (Subsec. 2.8.4). Williamson Decomposition is weighted for a smooth first derivative and from trial and error is required to be larger than the weights from our first two criteria. H_w is weighted at least three times as much via $\lambda_w = 3$.

All three shake out criteria are summed together to create a total score for the shake out covariance Σ_h as

$$score_h = \lambda_{shape} h_{shape} + \lambda_{transf} h_{transf} + \lambda_w h_w \tag{7.9}$$

The shake out minimizes the score and repeats until a value of $score_h \approx 0$ is achieved.

An example of an optimization plot is shown in Fig. 7.9 where in this particular instance we sent a noisy mode made of $n = 16$ pixels with a squeezing parameter of $r = \sqrt{0.5} \approx 0.71$ into our simulator. The shake out method was able to reduce the score to 0.75, but it took over 10^5 iterations, revealing the process's considerable demands in terms of labor and time.

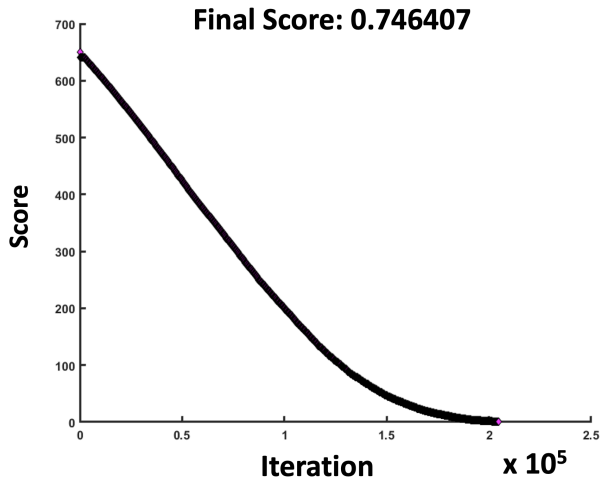

FIG. 7.9: An example of how many iterations needed to reach $score_h \approx 0$ via our shake out method.

As an example, Fig. 7.10a displays an experimentally measured covariance matrix and its shake out companion Σ_h in Fig. 7.10b. Note that although the element values have been shifted, the overall pattern of the covariances remains the same.

We will discuss this shake out example further as it appears again in Fig. 7.18.

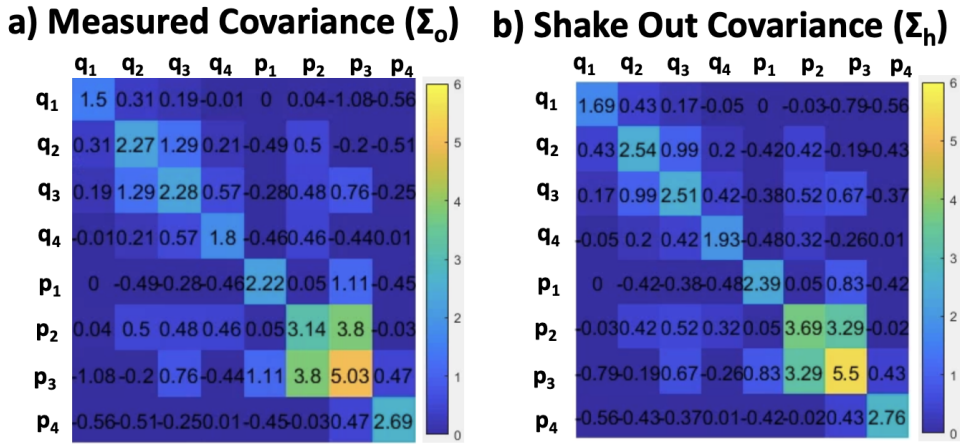

FIG. 7.10: a) An experimental covariance matrix. b) The resulting covariance matrix from the shake out method.

7.5 Spatial Reconstructions

Using the simulation discussed in Sec. 4.3, we estimate how much noise our decomposition process can handle before significantly altering mode structures and their squeezing parameters. Arbitrarily using ($n = 4$) pixels for the reconstruction, we simulate one squeezed mode with a varying squeezing parameter r with various amounts of noise added to the covariance.

Fig. 7.11a shows how reconstructed squeezing changes as more and more noise is added to the covariance matrix. A random noise matrix (Π) normally distributed with a spread of $\pm\eta$ added to the measured covariance as

$$\Sigma'_{o_{2n\times 2n}} = \Sigma_{o_{2n\times 2n}} + \Pi_{2n\times 2n}. \tag{7.10}$$

From there, Σ'_o takes the place of a measured covariance and we decompose it with our standard process and using the shake out method as needed when η becomes too contaminating.

We run several cases of squeezing; $r = 1,\ 0.71,\ 0.45,\ 0.32,\ 0.26$. Note $r = 1$ indicates there is no squeezing present in the system and the value of 1 has been normalized to represent shot noise. Thus, reconstructed squeezing values closer to 0 indicate more squeezing.

Fig. 7.11a shows the squeezing parameter of the strongest reconstructed mode for various input squeezing parameters, r, and added noise values, η. Fig. 7.11b shows the thermal field value of the strongest reconstructed mode for various input squeezing parameters, r, and added noise values, η. As only one mode was used in the simulation, any excess noise correlates to $\frac{1}{r}$. Fig. 7.11c shows the squeezing parameter of the second strongest reconstructed mode for various input squeezing parameters. But note, as we only

sent in one mode, this reconstruction should yield vacuum. Similarly, Fig. 7.11d shows the thermal field value of the second strongest reconstructed mode, which again is vacuum.

In Fig. 7.11a where no noise is added ($\eta = 0$) we see a squeezing value that matches our original input. As noise increases, we see an increase of the squeezing value for cases of $r < 1$ (blue trace) as the added noise increases. This tells us that any excess noise will hallucinate squeezing in a true vacuum mode! In our other reconstructed squeezing parameters, where squeezing actually exists, we see a slow degradation of r as added noise is increased. This trend continues until around $\eta = 0.27$ where results become inconsistent, informing us that this is likely the maximum amount of noise our system can handle while producing reasonable results. Our covariances with added noises of $\eta \leq 0.27$, although not pictured, do not have elements that exceed a value of 1.5, meaning we can handle noise uncertainties of approximately 17% and still reconstruct within the general regime our system is in.

The thermal parameters of the strongest mode are shown in Fig. 7.11b where each color trace corresponds to its match in Fig. 7.11a. When $\eta = 0$, we reconstruct no thermal contributions, or 1 as expected. However, once the system becomes noisy, we see thermal contributions grow. Where in Fig. 7.11a we saw a general trend of degraded squeezing, on the other side, we see thermal contamination grow similarly and more quickly the more squeezing there is (recall the light blue simulation is the most squeezed).

We next show the second mode squeezing parameter reconstruction (Fig. 7.11c) and thermal reconstruction (Fig. 7.11d), where we sent in vacuum. As we saw in the $r = 1$ vacuum case in Fig. 7.11a (dark blue trace), our decomposition scheme hallucinates squeezing in cases of vacuum. This is true, regardless of the squeezing parameter of other modes. We similarly see that thermal noise grows as our system noise (η) increases, solidifying our understanding of how noise affects the system.

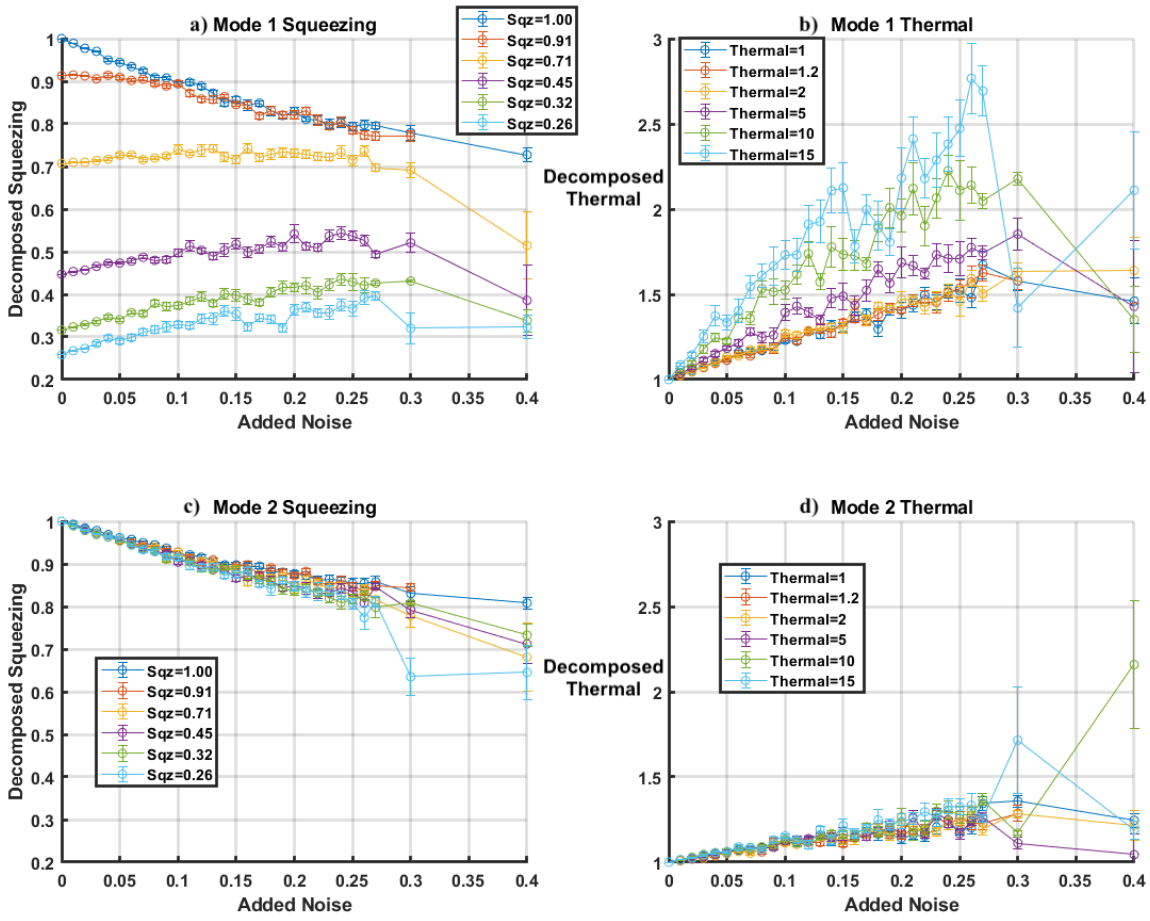

FIG. 7.11: Reconstructed squeezing level for various amounts of added noise where a) is the reconstructed squeezing parameter of the strongest mode, b) is the reconstructed thermal parameter of the strongest mode, c) is the reconstructed squeezing parameter of the next strongest mode, and d) is the reconstructed thermal parameter of the second strongest mode.

For completeness, we display the unwrapped strongest mode reconstruction amplitude for $r = 0.71$ and $r = 0.26$ in Fig. 7.12a,b respectively. Each mode is shown under varying noise conditions, $\eta = 0,\ 0.2\ 0.4$. Fig. 7.12a shows the actual amplitude in blue when there is no noise added to the system, an increase in noise to $\eta = 0.2$ still reconstructs a fairly flat phase that is not far off from the input mode. Even $\eta = 0.4$ produces a reasonable amplitude reconstruction, though it is unreliable and not repeatable. Fig. 7.12b shows the

same added noise, simply for $r = 0.26$ instead. Here it is apparent that the amplitude reconstruct of the $\eta = 0.4$ case is unreliable, but the $\eta = 0.2$ case is repeatable and very close to the flat amplitude input.

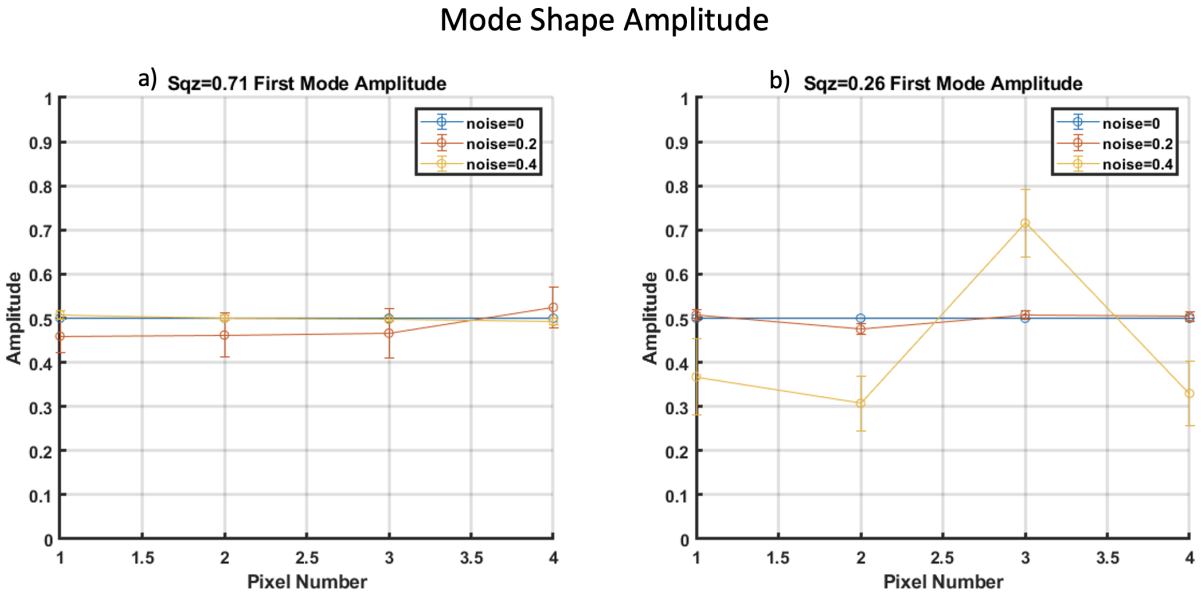

FIG. 7.12: a) Unwrapped reconstructed mode amplitudes for a $r = 0.71$ mode with added noise $\eta = 0, 0.2, 0.4$. b) Unwrapped reconstructed mode amplitudes for a $r = 0.26$ mode with added noise $\eta = 0, 0.2, 0.4$.

Our noise study concludes with the understanding that noise can make fake squeezing appear in a vacuum, but we can get reasonably close to the actual squeezing value until there is a noise contamination of $\eta = 0.27$.

7.6 Stripe Mask Simulation

Thus far we have only used square mask reconstruction, or $n = 4$ in a 2×2 setup. As we are experimentally power starved and cannot increase pixel resolution, we move to 4×1 masks and move the signal probe across the pixels to make a demonstration

of how the mode reconstructions will change. We anticipate that the mode amplitude strength will correlate to whichever pixel the signal best overlaps with. Experimental results are conducted thus that the signal probe is centered, moved upward, and downward. Experimental results will be discussed in Sec. 7.7.

We first use our simulation process, as done in our noise study, to move the 'signal' into each one of the $n = 4$ pixels with perfect overlap one at a time, under different noise conditions. We set the input signal mode to have a squeezing parameter of $r = \sqrt{2} \approx 0.71$.

Fig. 7.13 shows the covariance (top row), reconstructed mode amplitude (middle row), and reconstructed mode phase (bottom row) of $\eta = 0$ cases. The first column shows the 'signal' perfectly overlapped with the top mask stripe, the second column shows the 'signal' perfectly overlapped with the top mask stripe, the third column shows the 'signal' perfectly overlapped with the third mask stripe, and lastly the fourth column shows the 'signal' perfectly overlapped with the bottom mask stripe. The second row, reconstructed mode amplitudes, clearly shows which striped pixel the 'signal' overlaps with while the reconstructed phases in the third row remain flat, aligning with the input mode. Each reconstruction squeezing parameter is $r = 0.71$, also aligning with our input mode.

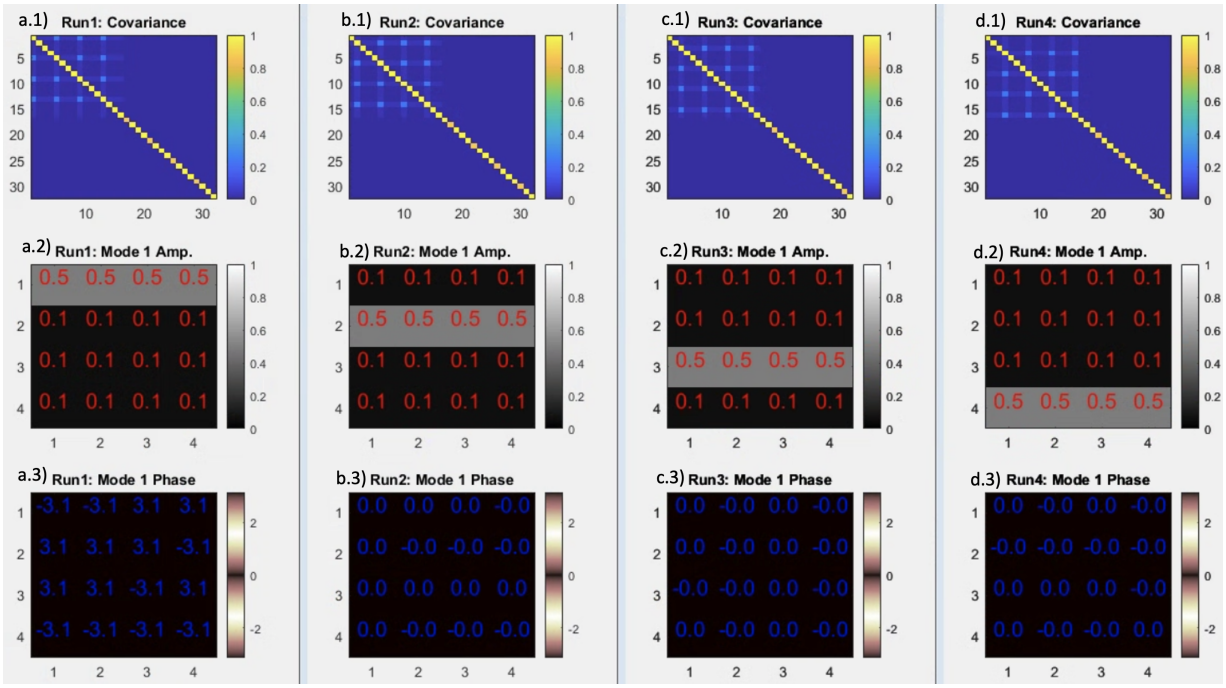

FIG. 7.13: Simulation of how mode shapes change as the signal probe spatially moved across different mask stripes without noise. a.1) The covariance matrix, in $(q_1, \ldots, q_n, p_1, \ldots, p_n)$ order, where the signal has perfect overlap with the top striped pixel, a squeezing parameter $r = 0.71$. b.1) The covariance matrix where the signal has perfect overlap with the second from the top striped pixel, a squeezing parameter $r = 0.71$. c.1) The covariance matrix where the signal has perfect overlap with the third from the top striped pixel, a squeezing parameter $r = 0.71$. d.1) The covariance matrix where the signal has perfect overlap with the bottom striped pixel, a squeezing parameter $r = 0.71$. a.2) Amplitude reconstruction of the mode when the signal is perfectly overlapped with the top striped pixel. b.2) Amplitude reconstruction of the mode when the signal is perfectly overlapped with the second from the top striped pixel. c.2) Amplitude reconstruction of the mode when the signal is perfectly overlapped with the third from the top striped pixel. d.2) Amplitude reconstruction of the mode when the signal is perfectly overlapped with the bottom striped pixel. a.3) Phase reconstruction of the mode when the signal is perfectly overlapped with the top striped pixel. b.3) Phase reconstruction of the mode when the signal is perfectly overlapped with the second from the top striped pixel. c.3) Phase reconstruction of the mode when the signal is perfectly overlapped with the third from the top striped pixel. d.3) Phase reconstruction of the mode when the signal is perfectly overlapped with the bottom striped pixel.

Fig. 7.14 repeats the same process as Fig. 7.13, but with a noise matrix with $\eta = 0.05$ added to each covariance matrix. Although the amplitude reconstructions of the second row are still able to successfully track which pixel the signal overlaps with, there is an uncertainty of 0.5 ± 0.1 in amplitudes. As some noise was added, this is expected. $\eta = 0.05$

is within our noise tolerance and the results are repeatable and valid.

However, once we look at the mode phase reconstructions in the third row, we see the added noise induces unpredictable phase jumps, which is expected. At the time of publication, this is still a problem to be resolved, but we will continue on with amplitude reconstructions.

The reconstructed squeezing parameters have the values $r = 0.75, 0.73, 0.72, 0.74$ for Fig. 7.14a,b,c,d respectively. The reconstructed squeezing parameters are comparable to our input mode's squeezing parameter. Our simulation does not account for the difference in illumination of the pixels. In the experimental results, it is predicted that the upward and downward signal positions will yield less squeezing due to a decrease in overlap.

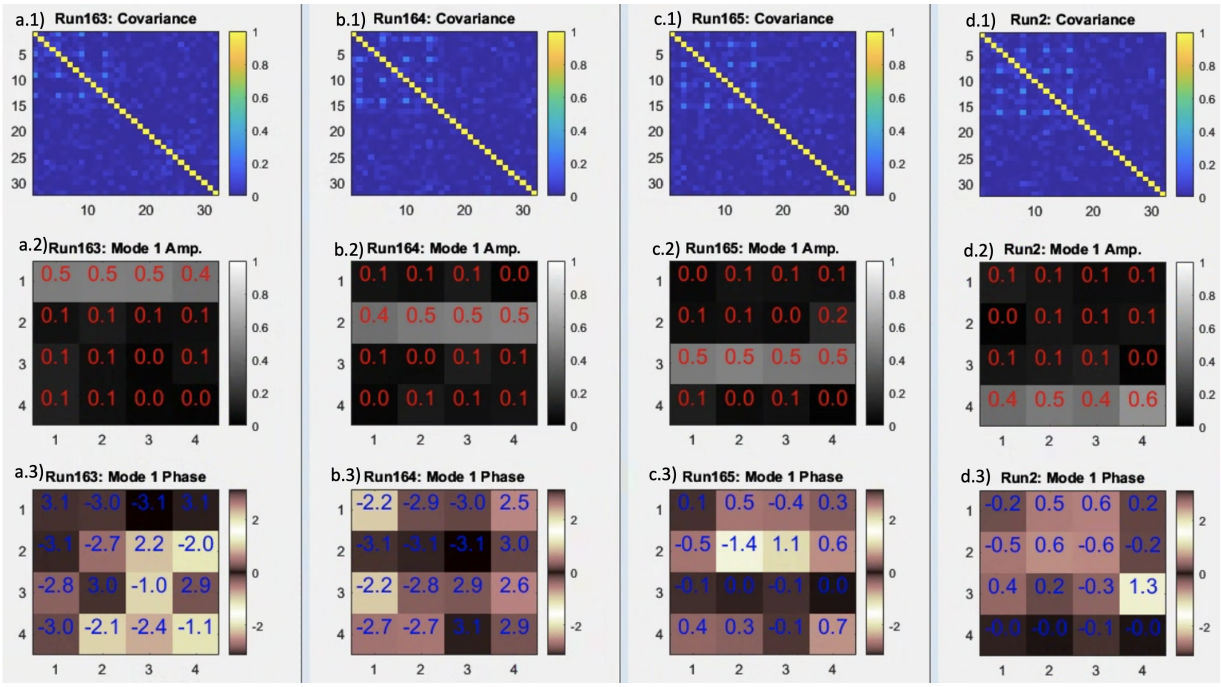

FIG. 7.14: Simulation of how mode shapes change as the signal probe spatially moved across different mask stripes with added noise $\eta = 0.05$. a.1) The covariance matrix, in $(q_1, \ldots, q_n, p_1, \ldots, p_n)$ order, where the signal has perfect overlap with the top striped pixel, a squeezing parameter $r = 0.71$. b.1) The covariance matrix where the signal has perfect overlap with the second from the top striped pixel, a squeezing parameter $r = 0.71$. c.1) The covariance matrix where the signal has perfect overlap with the third from the top striped pixel, a squeezing parameter $r = 0.71$. d.1) The covariance matrix where the signal has perfect overlap with the bottom striped pixel, a squeezing parameter $r = 0.71$. a.2) Amplitude reconstruction of the mode when the signal is perfectly overlapped with the top striped pixel. b.2) Amplitude reconstruction of the mode when the signal is perfectly overlapped with the second from the top striped pixel. c.2) Amplitude reconstruction of the mode when the signal is perfectly overlapped with the third from the top striped pixel. d.2) Amplitude reconstruction of the mode when the signal is perfectly overlapped with the bottom striped pixel. a.3) Phase reconstruction of the mode when the signal is perfectly overlapped with the top striped pixel. b.3) Phase reconstruction of the mode when the signal is perfectly overlapped with the second from the top striped pixel. c.3) Phase reconstruction of the mode when the signal is perfectly overlapped with the third from the top striped pixel. d.3) Phase reconstruction of the mode when the signal is perfectly overlapped with the bottom striped pixel.

Fig. 7.15 again repeats the same process as Fig. 7.13, but with a noise matrix with $\eta = 0.1$ added to each covariance matrix. As anticipated, there is some uncertainty in the middle row of amplitude reconstructions, but the general trend of highlighting the correct pixel can be seen. As there was already phase instability in the $\eta = 0.05$

reconstruction case, we again see phase instability. Each reconstruction case found $r = 0.73, 0.74, 0.77, 0.76$ for Fig. 7.15a,b,c,d respectively, which is still within our expected tolerance.

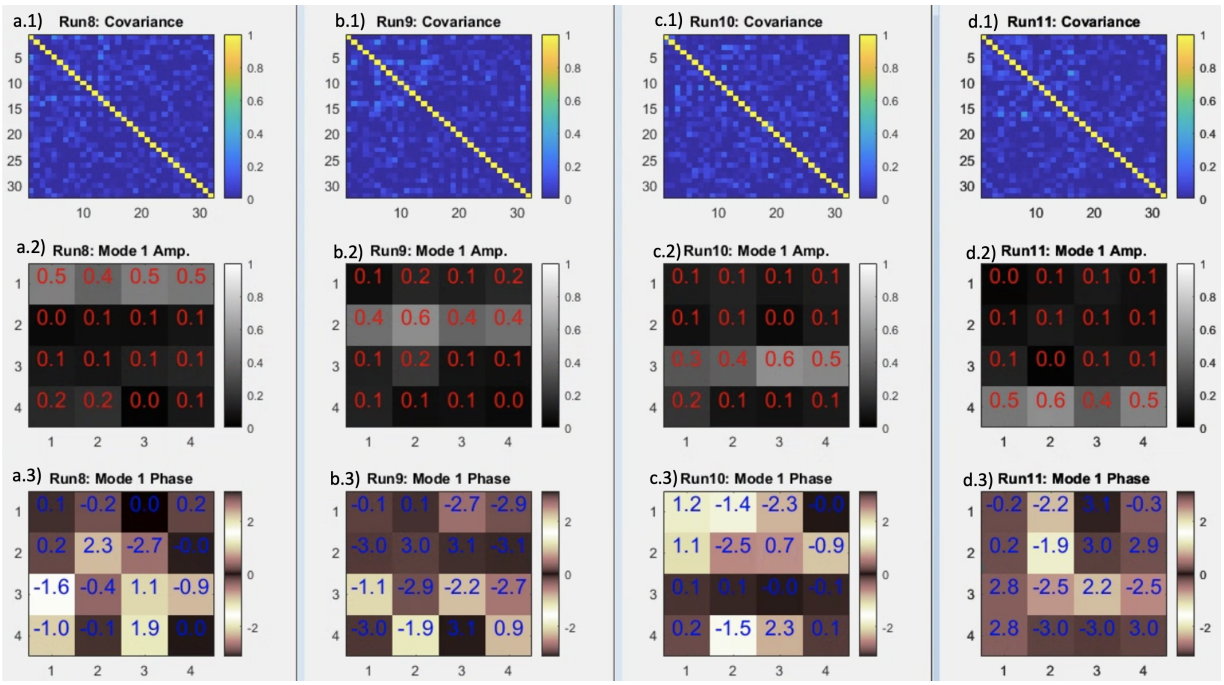

FIG. 7.15: Simulation of how mode shapes change as the signal probe spatially moved across different mask stripes with added noise $\eta = 0.1$. a.1) The covariance matrix, in $(q_1, \ldots, q_n, p_1, \ldots, p_n)$ order, where the signal has perfect overlap with the top striped pixel, a squeezing parameter $r = 0.71$. b.1) The covariance matrix where the signal has perfect overlap with the second from the top striped pixel, a squeezing parameter $r = 0.71$. c.1) The covariance matrix where the signal has perfect overlap with the third from the top striped pixel, a squeezing parameter $r = 0.71$. d.1) The covariance matrix where the signal has perfect overlap with the bottom striped pixel, a squeezing parameter $r = 0.71$. a.2) Amplitude reconstruction of the mode when the signal is perfectly overlapped with the top striped pixel. b.2) Amplitude reconstruction of the mode when the signal is perfectly overlapped with the second from the top striped pixel. c.2) Amplitude reconstruction of the mode when the signal is perfectly overlapped with the third from the top striped pixel. d.2) Amplitude reconstruction of the mode when the signal is perfectly overlapped with the bottom striped pixel. a.3) Phase reconstruction of the mode when the signal is perfectly overlapped with the top striped pixel. b.3) Phase reconstruction of the mode when the signal is perfectly overlapped with the second from the top striped pixel. c.3) Phase reconstruction of the mode when the signal is perfectly overlapped with the third from the top striped pixel. d.3) Phase reconstruction of the mode when the signal is perfectly overlapped with the bottom striped pixel.

The presence of extra noise near dark noise thresholds systematically modifies re-

constructed mode shapes through its impact on covariance matrix structures. As the signal-to-noise ratio degrades, noise contaminates inter-pixel correlations in the measured covariance matrix (Σ_o), blurring spatial features (Fig. 7.10). The shake out method addresses this by minimizing deviations through h_{shape} (Eq. 7.6) while enforcing physical constraints like positive eigenvalues via h_{transf} (Eq. 7.7). However, these corrections cannot fully recover lost spatial resolution. The iterative optimization (Eq. 7.9) necessarily prioritizes matrix physicality over fine structural fidelity, leading to homogenized mode patterns.

This noise-induced smearing arises from fundamental trade-offs in covariance matrix correction. While the weighted score optimization (Eq. 7.9) preserves covariance patterns, local element shifts during shake out processing (Fig. 7.10b) accumulate as spatial averaging effects in mode reconstructions. The method's convergence requirement ($score_h \approx 0$) forces compromises between suppressing negative eigenvalues and retaining genuine modal features. This is exemplified by the extensive iterations needed even for modest noise levels (Fig. 7.9). Consequently, reconstructed modes exhibit a smeared modification due to the excess noise.

7.7 Experimental Demonstration of Stripe Reconstructions

We experimentally show a reconstruction demonstration in which a $4x1$ horizontally striped mask is used. Similarly to the simulations conducted in Sec. 7.6, we first reconstruct the signal overlapped near the top of the masked horizontal stripes, then centered on the middle two stripes, and lastly lower down on the striped mask. We focus on the reconstruction of the mode's amplitude and squeezing parameter, as our simulations con-

cluded there are further efforts needed for phase reconstructions. One note to make: we increase the averaging and automating processes in the data acquisition scheme to compensate for traces that are near dark noise. Thus, there were frequent pauses between runs, leaving enough time for laser drifts and other experimental inconsistencies discussed in Ch. 5. Additionally, due to the longer acquisition time, several runs failed in communication protocols requiring the run to restart. Luckily, we can utilize the shake out method for completed runs.

The signal is first in an 'upward location' as shown in Fig. 7.16a. The first row shows a camera display for reference where the stripes are shown with purple dividing lines, the LO is circled in green, and the probe is circled in red. The second row shows the covariance, shake out covariance, thermal field reconstructions, and squeezed parameter reconstructions of the first run. The third row shows the same information as the second row, but for run#2 and the bottom row has the repeated information for a third run.

Fig. 7.16b,f,j displays the measured covariances (Σ_o) of the experimental setup. However, as none of the measured covariances were decomposable, we utilize the shake out method to produce Σ_h as shown in Fig. 7.16c,g,k. From there each runs' thermal (Fig. 7.16d,h,m) and squeezing parameters (Fig. 7.16e,i,n) are shown.

Runs 1 and 2 were taken back to back while runs between 2 and 3 initially failed, causing a much longer time delay and is likely why the covariance matrices of run 3 yield a different shape. However, in all cases, the third pixel is clearly highlighted. It was expected that one pixel be stronger than the others. The squeezing parameters of the strongest mode from runs 1 and 2 are similar as $r_{run1_1} = 0.45$ and $r_{run2_1} = 0.48$. We suspect run 3's different squeezing parameter again highlights the change in experimental settings.

As we were using $n = 4$ pixels, there are four modes reconstructed in total per run, where each mode reconstruction is shown in a column of Fig. 7.17. The first mode is

the strongest and we see a consistent amplitude reconstruction between all three runs, as expected. Phase reconstruction has been π wrapped and is included for completeness. There is similarity between the phase reconstruction of runs 1 and 2, but it is overall inconsistent. As we move down the columns of Fig. 7.17 we reconstruct weaker and weaker modes, but as a vacuum mode is never reconstructed, it is likely there are more than four modes in the system. This is also supported by the amplitude reconstruction of the weakest mode in each run. There is a clear relation, but as all modes must be orthogonal, it is likely that the remaining components of the runs are similar, yielding a repeatable weakest mode amplitude.

The signal is next (somewhat) centered between the two most illuminated stripe pixels and Fig. 7.18 follows the same structure as Fig. 7.16. Here each runs' covariance highlights pixels 2 and 3, as expected. Again the first two runs are most similar, suggesting experimental changes in the third run. This is again highlighted by each run's strongest mode squeezing parameter where $r_{run1_1} = 0.74$ and $r_{run2_1} = 0.72$ are fairly similar. As expected we see more squeezing in the signal center case than in the signal upward position, as we are better overlapped, or more centered, with the LO and are utilizing the more illuminated pixels.

The unwrapped mode amplitude and phase reconstructions are shown in Fig. 7.19, following the same ordering patter as in Fig. 7.17. We see reasonable agreement in the strongest mode's amplitude reconstruction and as the modes weaken as we move down the rows, there is again remaining components that artificially permit the weakest mode amplitude reconstruction to be similar amounts all runs.

We discuss our last run-type: a downward aligned signal. The downward signal runs were all done back to back, thus they had the shorted acquisition time between them. Recall that the upward signal highlighted pixel 3, the centered signal highlighted pixels 2 and 3. Should logic prevail, we expect the downward signal to highlight pixel 2. From

the covariances displayed in Fig. 7.20, we see that indeed pixel 2 is strongest. The third run highlights q_2 rather than p_2, suggesting some noiseball rotation between runs, but regardless, the squeezing parameters of the strongest mode from each run are similar as $r_{run1_1} = 0.48$, $r_{run2_1} = 0.49$, and $r_{run3_1} = 0.49$. Recall this is approximately the squeezing value found for the upward signal, but less than the centered signal, as expected.

The mode reconstruction amplitudes and phases are shown in Fig. 7.21 where we again see the amplitude reconstructions of the strongest modes agree and the weakest mode amplitude reconstructions likely agree due to the orthogonality of the reconstructed modes. Even here were our runs were most closely done back to back, there is no repeatable phase reconstruction agreement.

We conclude that, experimentally, we can achieve representative runs that are within our simulated noise tolerance, suggesting this reconstruction method is valid for separating out individual modes from a multimode scheme.

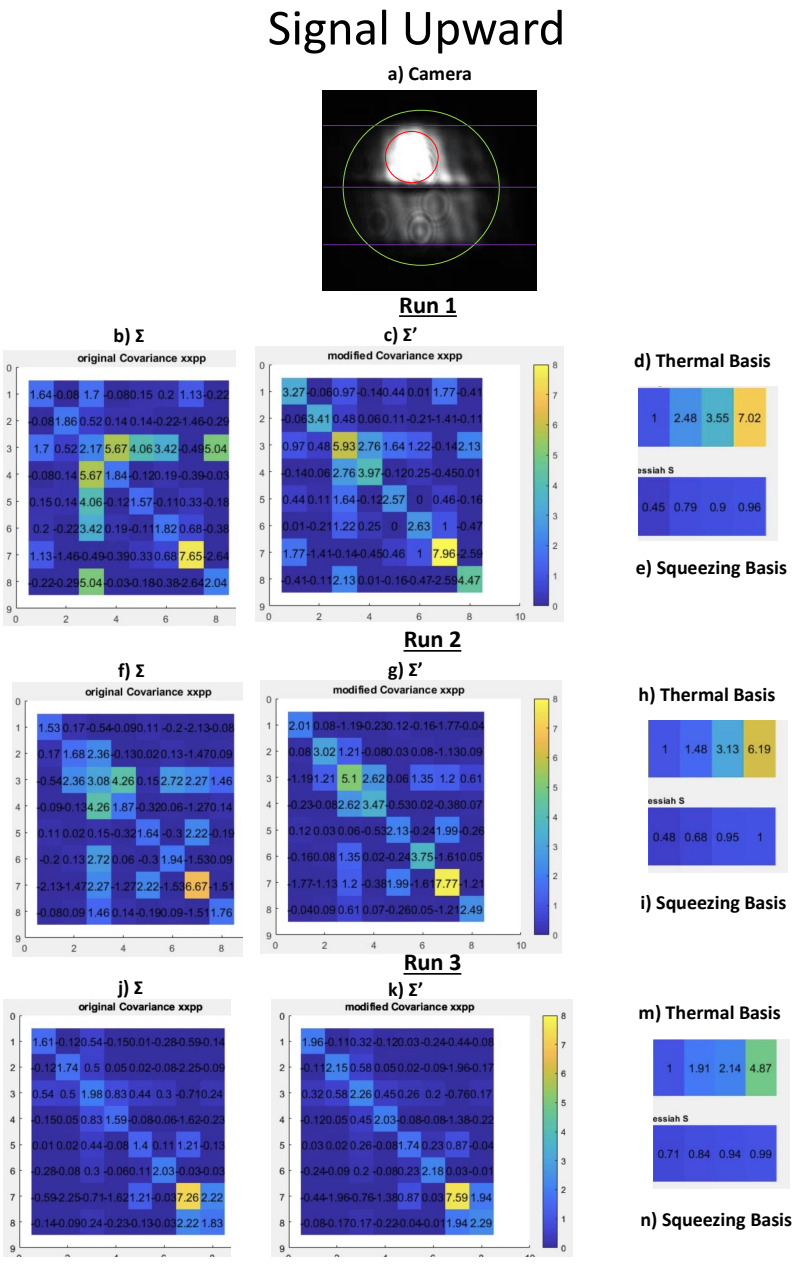

FIG. 7.16: The signal is most overlapped with pixel 3 such that a) the camera reference image of the signal's (red circle) overlaps with the LO (green circle) which is masked by four striped pixels (divided by the purple lines). b) The measured covariance Σ_o of run 1. c) The shake out covariance Σ_h of run 1. d) Thermal reconstruction from Williamson Decomposition where the strongest mode's thermal parameter is $D(1) = 1$ for run 1. e) The squeezing parameters reconstructed in run 1 where the strongest mode has a parameter of $r(1) = 0.45$. f)The measured covariance Σ_o of run 2. g) The shake out covariance Σ_h of run 2. h) Thermal reconstruction from Williamson Decomposition where the strongest mode's thermal parameter is $D(1) = 1$ for run 2. i) The squeezing parameters reconstructed in run 2 where the strongest mode has a parameter of $r(1) = 0.48$. j) The measured covariance Σ_o of run 3. k) The shake out covariance Σ_h of run 2. m) Thermal reconstruction from Williamson Decomposition where the strongest mode's thermal parameter is $D(1) = 1$ for run 3. n) The squeezing parameters reconstructed in run 3 where the strongest mode has a parameter of $r(1) = 0.71$.

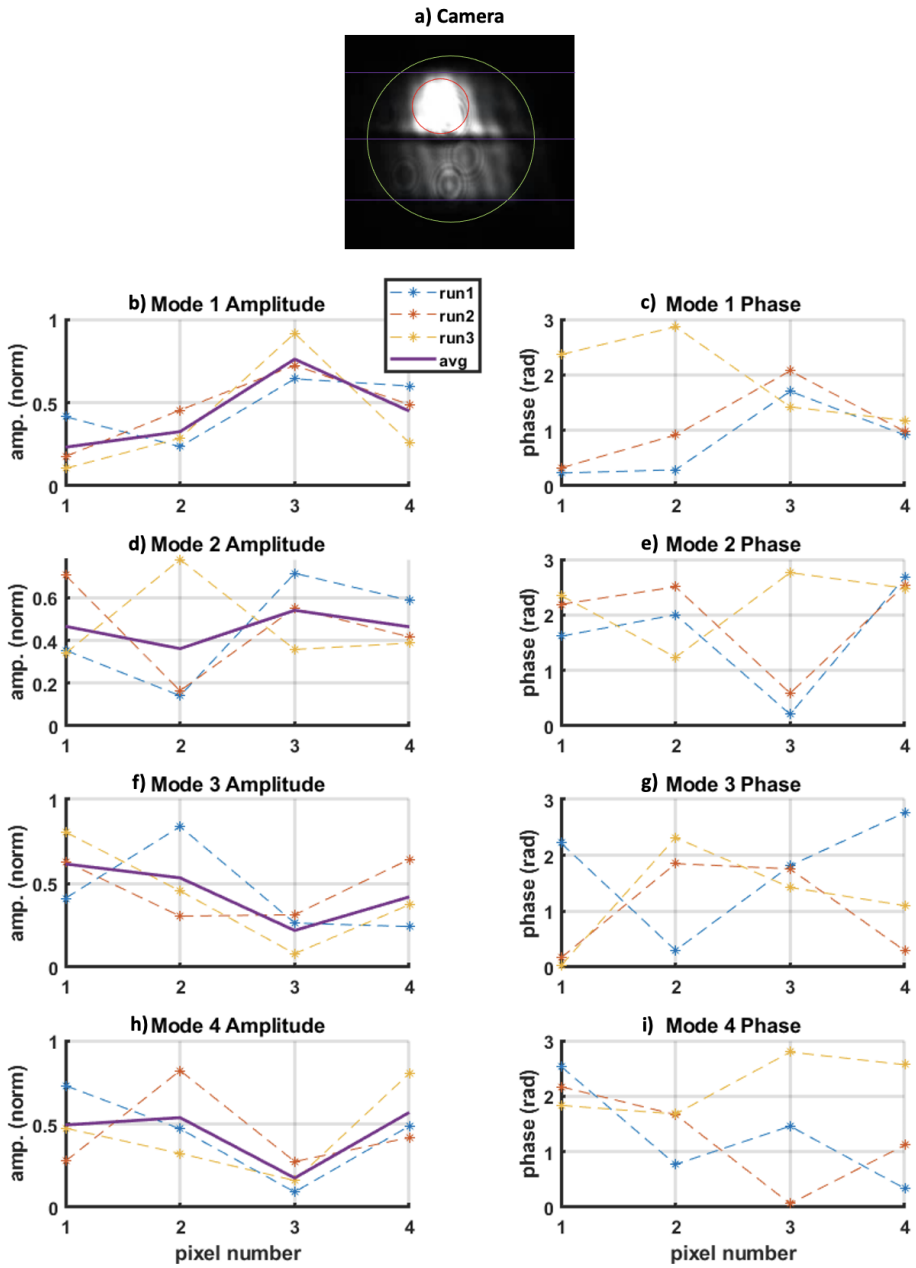

FIG. 7.17: The signal is most overlapped with pixel 3 such that a) the camera reference image of the signal's (red circle) overlaps with the LO (green circle) which is masked by four striped pixels (divided by the purple lines). b) The unwrapped amplitude reconstructions of the strongest mode from all runs and their average. c) The unwrapped phase reconstructions of the strongest mode from all runs d) The unwrapped amplitude reconstructions of the second strongest mode from all runs and their average. e) The unwrapped phase reconstructions of the second strongest mode from all runs f) The unwrapped amplitude reconstructions of the third strongest mode from all runs and their average. g) The unwrapped phase reconstructions of the third strongest mode from all runs h) The unwrapped amplitude reconstructions of the weakest mode from all runs and their average. i) The unwrapped phase reconstructions of the weakest mode from all runs.

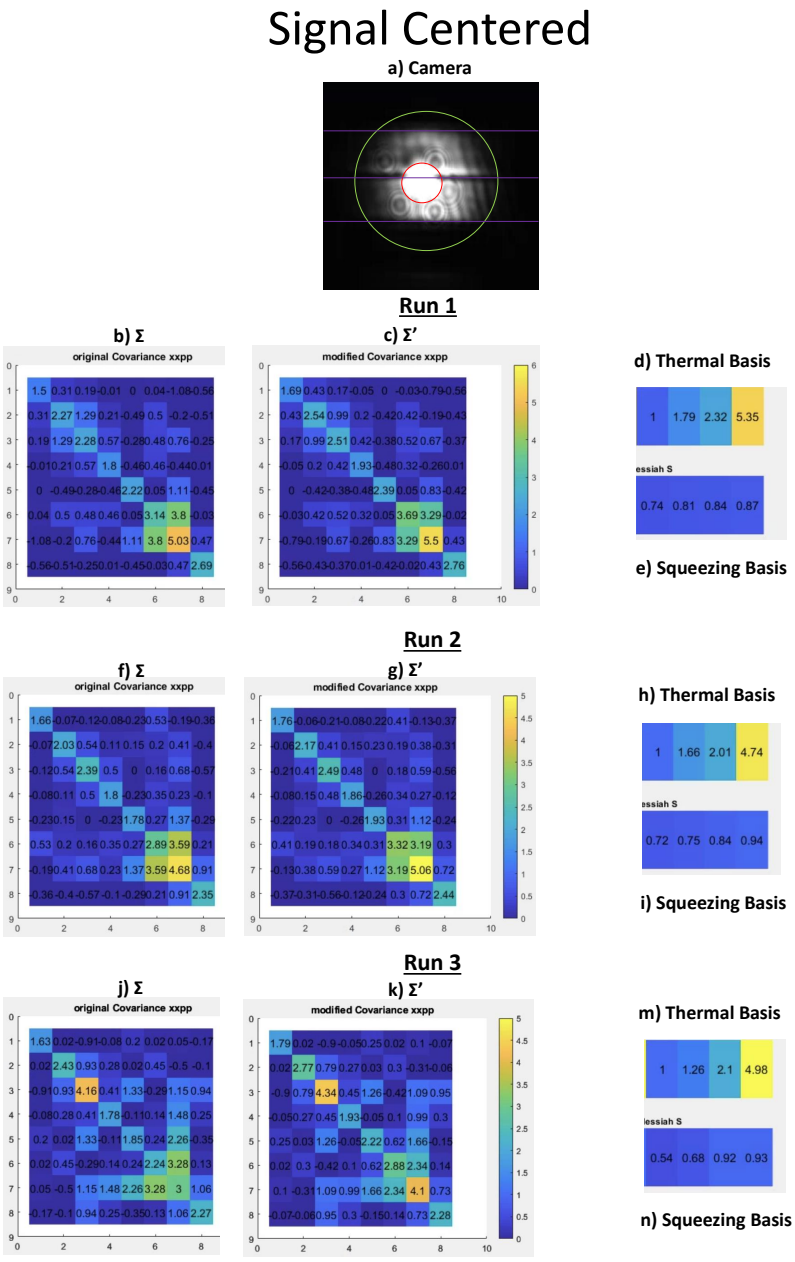

FIG. 7.18: The signal is overlapped with pixels 2 and 3 such that a) the camera reference image of the signal's (red circle) overlaps with the LO (green circle) which is masked by four striped pixels (divided by the purple lines). b) The measured covariance Σ_o of run 1. c) The shake out covariance Σ_h of run 1. d) Thermal reconstruction from Williamson Decomposition where the strongest mode's thermal parameter is $D(1) = 1$ for run 1. e) The squeezing parameters reconstructed in run 1 where the strongest mode has a parameter of $r(1) = 0.74$. f)The measured covariance Σ_o of run 2. g) The shake out covariance Σ_h of run 2. h) Thermal reconstruction from Williamson Decomposition where the strongest mode's thermal parameter is $D(1) = 1$ for run 2. i) The squeezing parameters reconstructed in run 2 where the strongest mode has a parameter of $r(1) = 0.72$. j) The measured covariance Σ_o of run 3. k) The shake out covariance Σ_h of run 2. m) Thermal reconstruction from Williamson Decomposition where the strongest mode's thermal parameter is $D(1) = 1$ for run 3. n) The squeezing parameters reconstructed in run 3 where the strongest mode has a parameter of $r(1) = 0.54$.

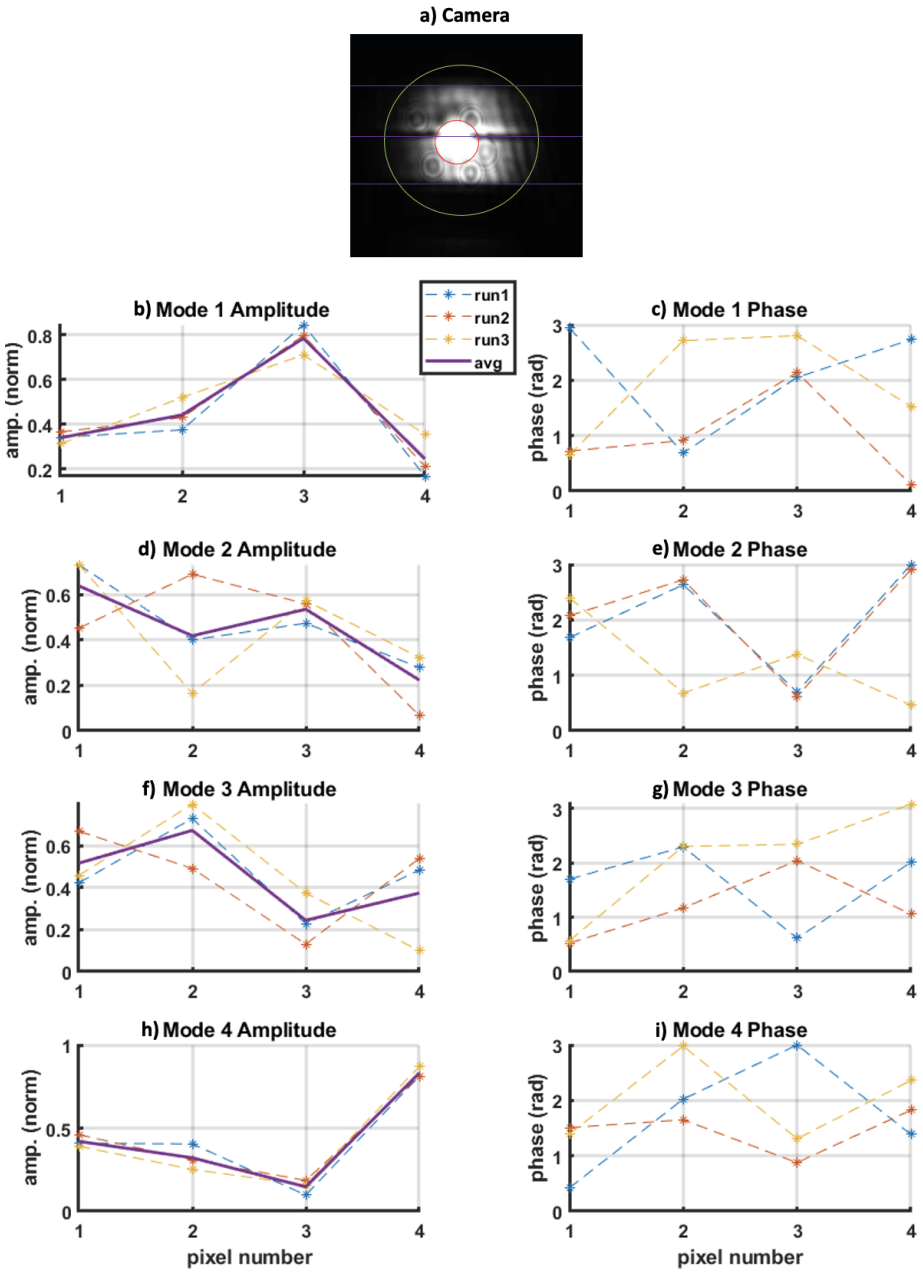

FIG. 7.19: The signal is overlapped with pixels 2 and 3 such that a) the camera reference image of the signal's (red circle) overlaps with the LO (green circle) which is masked by four striped pixels (divided by the purple lines). b) The unwrapped amplitude reconstructions of the strongest mode from all runs and their average. c) The unwrapped phase reconstructions of the strongest mode from all runs d) The unwrapped amplitude reconstructions of the second strongest mode from all runs and their average. e) The unwrapped phase reconstructions of the second strongest mode from all runs f) The unwrapped amplitude reconstructions of the third strongest mode from all runs and their average. g) The unwrapped phase reconstructions of the third strongest mode from all runs h) The unwrapped amplitude reconstructions of the weakest mode from all runs and their average. i) The unwrapped phase reconstructions of the weakest mode from all runs.

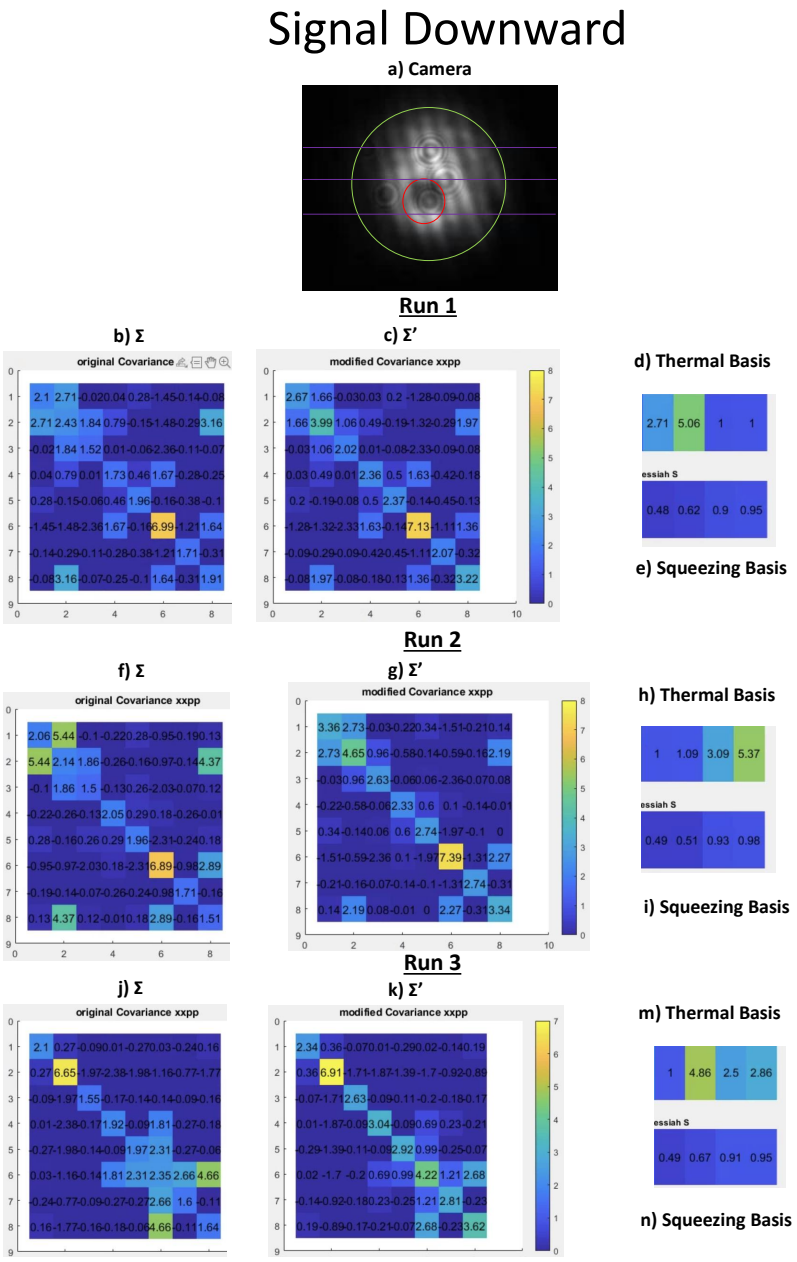

FIG. 7.20: The signal is most overlapped with pixel 2 such that a) the camera reference image of the signal's (red circle) overlaps with the LO (green circle) which is masked by four striped pixels (divided by the purple lines). b) The measured covariance Σ_o of run 1. c) The shake out covariance Σ_h of run 1. d) Thermal reconstruction from Williamson Decomposition where the strongest mode's thermal parameter is $D(1) = 2.71$ for run 1. e) The squeezing parameters reconstructed in run 1 where the strongest mode has a parameter of $r(1) = 0.48$. f)The measured covariance Σ_o of run 2. g) The shake out covariance Σ_h of run 2. h) Thermal reconstruction from Williamson Decomposition where the strongest mode's thermal parameter is $D(1) = 1$ for run 2. i) The squeezing parameters reconstructed in run 2 where the strongest mode has a parameter of $r(1) = 0.72$. j) The measured covariance Σ_o of run 3. k) The shake out covariance Σ_h of run 2. m) Thermal reconstruction from Williamson Decomposition where the strongest mode's thermal parameter is $D(1) = 1$ for run 3. n) The squeezing parameters reconstructed in run 3 where the strongest mode has a parameter of $r(1) = 0.49$.

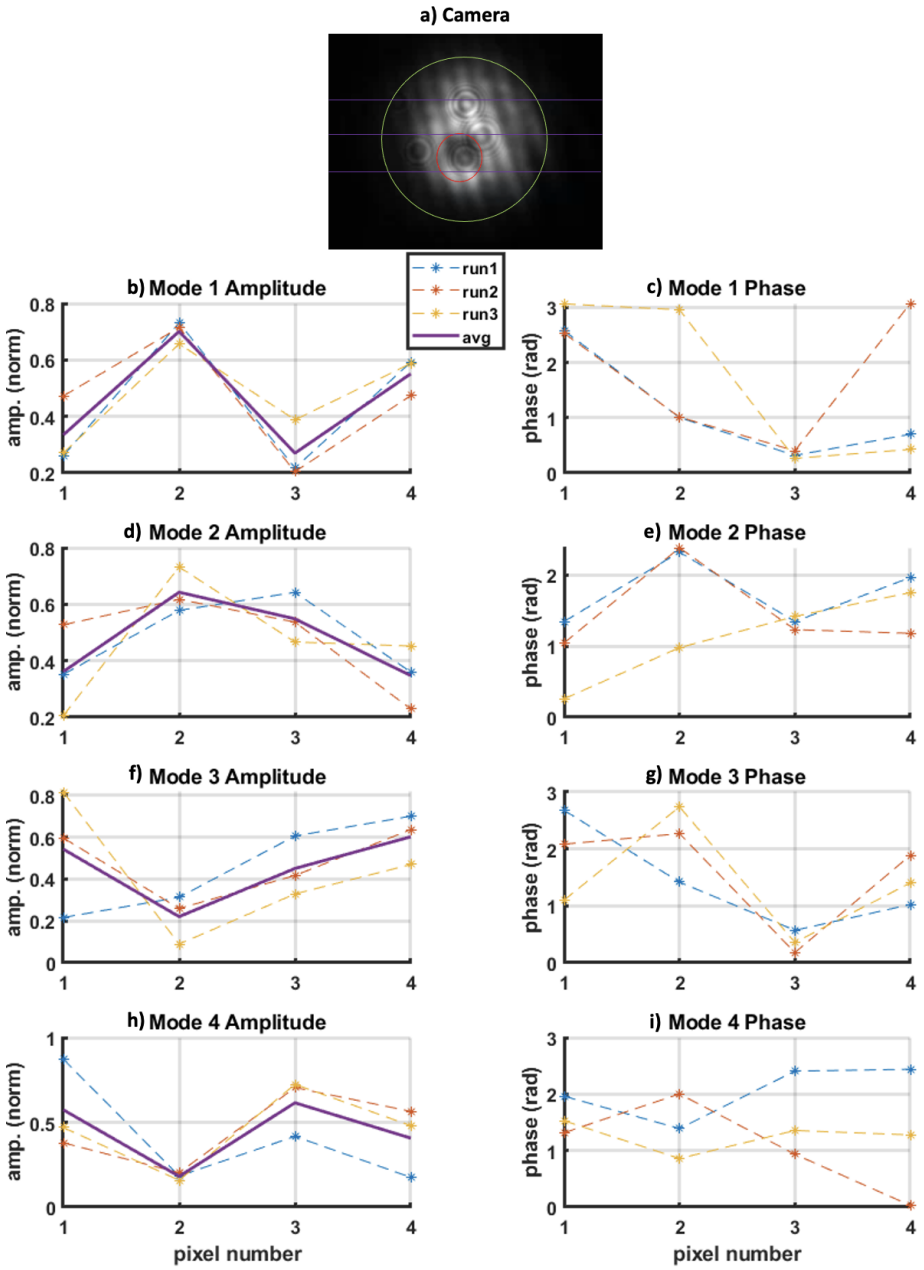

FIG. 7.21: The signal is most overlapped with pixel 2 such that a) the camera reference image of the signal's (red circle) overlaps with the LO (green circle) which is masked by four striped pixels (divided by the purple lines). b) The unwrapped amplitude reconstructions of the strongest mode from all runs and their average. c) The unwrapped phase reconstructions of the strongest mode from all runs d) The unwrapped amplitude reconstructions of the second strongest mode from all runs and their average. e) The unwrapped phase reconstructions of the second strongest mode from all runs f) The unwrapped amplitude reconstructions of the third strongest mode from all runs and their average. g) The unwrapped phase reconstructions of the third strongest mode from all runs h) The unwrapped amplitude reconstructions of the weakest mode from all runs and their average. i) The unwrapped phase reconstructions of the weakest mode from all runs.

CHAPTER 8

Conclusion and Outlook

In this dissertation, the spatial reconstruction of quantum states of light has been explored in depth, with particular attention to the identification and separation of individual squeezed modes within complex multimode quantum optical fields. By constructing and applying a generalized reconstruction framework, this work has shown that squeezed states, which are essential for quantum-enhanced measurement and imaging, can be isolated even when they are spatially overlapped and affected by noise. Through the combined use of theoretical modeling, numerical simulations, and experimental validation, the approach enables the retrieval of both squeezing parameters and spatial mode profiles from intricate covariance measurements.

The integration of concepts from classical imaging with quantum measurement protocols made it possible to reconstruct not only classical objects but also the distributions of quantum noise, though the current experimental setup is limited to four pixels due to laser power constraints. The method has proven robust in the presence of technical noise and has established clear benchmarks for noise tolerance and resolution, as confirmed by both simulation and experiment, though further development is needed for comprehensive

phase reconstruction.

Altogether, this dissertation delivers a comprehensive framework for resolving quantum states of light in realistic scenarios where noise and mode mixing are present. The techniques developed here pave the way for new advances in quantum-enhanced imaging, precision metrology, and the study of complex quantum systems. Looking ahead, the methods described offer a route to further improvements in spatial resolution, noise mitigation, and the practical deployment of quantum resources in measurement, with the potential to impact quantum information science and advanced sensing technologies.

BIBLIOGRAPHY

[1] T. S. Horrom, *Experimental Generation and Manipulation of Quantum Squeezed Vacuum via Polarization Self-Rotation in Rb Vapor*, Ph.D. thesis, College of William&Mary, Williamsburg (2013).

[2] S. L. Cuozzo, C. Gabaldon, P. J. Barge, Z. Niu, H. Lee, L. Cohen, I. Novikova, and E. E. Mikhailov, Optics Express **30**, 37938 (2022).

[3] J. J. Sakurai and J. Napolitano, *Modern Quantum Mechanics*, 3rd ed. (Cambridge University Press, Cambridge, United Kingdom, 2020).

[4] H.-A. Bachor and T. C. Ralph, *A Guide to Experiments in Quantum Optics*, 2nd ed. (Wiley-VCH, USA, 2004).

[5] W. Heisenberg, Zeitschrift für Physik **43**, 172 (1927), in German; introduces the uncertainty principle.

[6] R. J. Glauber, Phys. Rev. **130**, 2529 (1963).

[7] J. R. Klauder, Journal of Mathematical Physics **4**, 1058 (1963).

[8] E. C. G. Sudarshan, Physical Review Letters **10**, 277 (1963).

[9] C. Gerry and P. Knight, *Introductory Quantum Optics* (Cambridge University Press, 2005) pp. 152,153.

[10] H. J. Carmichael and D. F. Walls, Journal of Physics B: Atomic and Molecular Physics **9**, L43 (1976).

[11] H. J. Kimble, M. Dagenais, and L. Mandel, Phys. Rev. Lett. **39**, 691 (1977).

[12] D. Stoler, Phys. Rev. D **1**, 3217 (1970).

[13] D. Stoler, Phys. Rev. D **4**, 1925 (1971).

[14] D. C. Burnham and D. L. Weinberg, Phys. Rev. Lett. **25**, 84 (1970).

[15] H. P. Yuen and J. H. Shapiro, Opt. Lett. **4**, 334 (1979).

[16] C. M. Caves, Phys. Rev. D **23**, 1693 (1981).

[17] D. F. Walls, Nature **306**, 141 (1983).

[18] S. Cuozzo, *Quantum Sensing For Low-Light Imaging*, Dissertation, William & Mary (2022), doctor of Philosophy (Ph.D.) in Physics.

[19] R. E. Slusher, L. W. Hollberg, B. Yurke, J. C. Mertz, and J. F. Valley, Phys. Rev. Lett. **55**, 2409 (1985).

[20] R. M. Shelby, M. D. Levenson, S. H. Perlmutter, R. G. DeVoe, and D. F. Walls, Phys. Rev. Lett. **57**, 691 (1986).

[21] L.-A. Wu, M. Xiao, and H. J. Kimble, J. Opt. Soc. Am. B **4**, 1465 (1987).

[22] S. F. Pereira, M. Xiao, H. J. Kimble, and J. L. Hall, Phys. Rev. A **38**, 4931 (1988).

[23] R. E. Slusher, B. Yurke, P. Grangier, A. LaPorta, D. F. Walls, and M. Reid, J. Opt. Soc. Am. B **4**, 1453 (1987).

[24] M. Mehmet, S. Ast, T. Eberle, S. Steinlechner, H. Vahlbruch, and R. Schnabel, Opt. Express **19**, 25763 (2011).

[25] Y. qing Li and M. Xiao, Opt. Express **2**, 110 (1998).

[26] U. L. Andersen, T. Gehring, C. Marquardt, and G. Leuchs, Phys. Scr. **91** (2016).

[27] Y. Zhang, M. Menotti, K. Tan, and et al., Nat COmmmun **12** (2021), 10.1038/s41467-021-22540-2.

[28] H. Vahlbruch, M. Mehmet, K. Danzmann, and R. Schnabel, Phys. Rev. Lett. **117**, 110801 (2016).

[29] C. F. McCormick, V. Boyer, E. Arimondo, and P. D. Lett, Opt. Lett. **32**, 178 (2007).

[30] V. Boyer, A. M. Marino, and P. D. Lett, Phys. Rev. Lett. **100**, 143601 (2008).

[31] I. Novikova, A. B. Matsko, and G. R. Welch, Opt. Lett. **26**, 1016 (2001).

[32] I. Novikova, A. B. Matsko, and G. R. Welch, Journal of Modern Optics **49**, 2565 (2002).

[33] I. Novikova, A. B. Matsko, and G. R. Welch, J. Mod. Opt. **49**, 2565 (2002).

[34] A. B. Matsko, I. Novikova, G. R. Welch, D. Budker, D. F. Kimball, and S. M. Rochester, Phys. Rev. A **66**, 043815 (2002).

[35] I. Novikova, A. B. Matsko, and G. R. Welch, Journal of Modern Optics **49**, 2565 (2002).

[36] E. E. Mikhailov, A. Lezama, T. W. Noel, and I. Novikova, Journal of Modern Optics **56**, 1985 (2009), arXiv:0903.3156 .

[37] T. Horrom, S. Balik, A. Lezama, M. D. Havey, and E. E. Mikhailov, Physical Review A **83**, 053850 (2011).

[38] T. Horrom, R. Singh, J. P. Dowling, and E. E. Mikhailov, Phys. Rev. A **86**, 023803 (2012), arXiv:1202.3831 .

[39] J. Kong, R. Jiménez-Martínez, C. Troullinou, V. G. Lucivero, G. Tóth, and M. W. Mitchell, Nature Communications **11**, 2415 (2020).

[40] C. Troullinou, *Squeezed-Light-Enhanced Magnetometry in a High Density Atomic Vapor*, Phd thesis, ICFO - The Institute of Photonic Sciences, UPC - Universitat Politècnica de Catalunya, Barcelona, Spain (2022).

[41] A. M. Marino and C. R. Stroud, Phys. Rev. A **74**, 022315 (2006).

[42] J. Aasi and *et al.*, Nature Photonics **7**, 613–619 (2013).

[43] T. L. S. Collaboration, the Virgo Collaboration, and the KAGRA Collaboration, Physical Review X **13**, 041021 (2023).

[44] J. Zhao, Z. Yuan, X. Liu, Y. Wang, W. Huang, C.-H. Yu, X. Chen, K. Zhang, and L. Q. Chen, Science Advances **11**, eadu4888 (2025).

[45] Z. Yu, S. Liu, J. Guo, G. Bao, Y. Wu, and L. Chen, Opt. Express **30**, 17106 (2022).

[46] M. Zhang, *Study of Spatial Structure of Squeezed Vacuum Field*, Ph.D. thesis, College of William&Mary, Williamsburg (2017).

[47] R. N. Lanning, Z. Xiao, M. Zhang, I. Novikova, E. E. Mikhailov, and J. P. Dowling, Phys. Rev. A (2018), arXiv:1806.04201 .

[48] J. Li and I. Novikova, J. Opt. Soc. Am. B **39**, 2998 (2022).

[49] P. Valente, A. Auyuanet, S. Barreiro, H. Failache, and A. Lezama, (2015), arXiv:1504.03904 [quant-ph], arXiv:1504.03904 [quant-ph] .

[50] A. Serafini, *Quantum Continuous Variables: A Primer of Theoretical Methods*, 1st ed. (CRC Press, 2017).

[51] J. Williamson, American Journal of Mathematics **58**, 141 (1936).

[52] W. M. M. Houde and N. Quesada, arXiv preprint arXiv:2403.04596 (2024).

[53] C. Bloch and A. Messiah, Nuclear Physics **39**, 95 (1962).

[54] S. L. Braunstein, Physical Review A **71**, 055801 (2005).

[55] G. Cariolaro and G. Pierobon, Physical Review A **94**, 062109 (2016).

[56] G. P. Tobias Lipfert, Dmitri B. Horoshko and M. I. Kolobov, Physical Review A **98**, 013815 (2018).

[57] W. McCutcheon, arXiv preprint arXiv:1809.02544 (2018), arXiv:1809.02544 [quant-ph] .

[58] V. Devanathan, *Nuclear Physics* (Narosa Publishing House and Alpha Science International, New Delhi, India and U.K., 2011) Chap. 2.1.

[59] V. Devanathan, Journal of Chennai Academy of Sciences **2**, 26 (2020).

[60] B. Gard, *Advances in Quantum Metrology: Continuous Variables in Phase Space*, Ph.D. thesis, Louisiana State University, Baton Rouge, LA (2016).

[61] E. Wigner, Physical Review **40**, 749 (1932).

[62] A. K. Ekert and P. L. Knight, Phys. Rev. A **43**, 3934 (1991) (2016).

[63] M. Walschaers, PRX Quantum **2**, 030204 (2021).

[64] S. Olivares, The European Physical Journal Special Topics **203**, 3–24 (2012).

[65] C. Gabaldon, P. Barge, S. L. Cuozzo, I. Novikova, H. Lee, L. Cohen, and E. E. Mikhailov, AVS Quantum Science **5**, 025005 (2023).

[66] M. O. Scully and M. S. Zubairy, *Quantum Optics* (Cambridge University Press, Cambridge, UK, 1997).

[67] C.-H. Huang, Y.-H. Wen, and Y.-W. Liu, Opt. Express **24**, 4278 (2016).

[68] C. Cohen-Tannoudji, B. Diu, and F. Laloë, *Quantum Mechanics* (Wiley, New York, NY, 1977) trans. of: Mécanique quantique. Paris: Hermann, 1973.

[69] L. A. Zadeh, Information and Control **8**, 338 (1965).

[70] N. Killoran, J. Izaac, N. Quesada, V. Bergholm, M. Amy, and C. Weedbrook, Quantum **3**, 129 (2019).

[71] V. Bužek, G. Adam, and G. Drobný, Phys. Rev. A **54**, 804 (1996).

[72] E. Zayed, A. Daoud, M. AL-Laithy, and E. Naseem, Chaos, Solitons and Fractals **24**, 967 (2005).

[73] J. J. Sakurai and J. Napolitano, *Modern Quantum Mechanics*, 2nd ed. (Addison-Wesley, Boston, 2011).

[74] B. Yurke, S. L. McCall, and J. R. Klauder, Phys. Rev. A **33**, 4033 (1986).

[75] M. A. de Gosson, Journal of Mathematical Physics (2021), 10.1063/5.0054444.

[76] R. S. Bennink and R. W. Boyd, Phys. Rev. A **66**, 053815 (2002).

[77] G. Gibson, J. Courtial, M. Padgett, M. Vasnetsov, V. Pas'ko, S. Barnett, and S. Franke-Arnold, Opt. Express **12**, 5448 (2004).

[78] A. Christ, C. Lupo, and C. Silberhorn, New Journal of Physics **14**, 083007 (2012).

[79] G. Brida, M. Genovese, A. Meda, and I. R. Berchera, Phys. Rev. A **83**, 033811 (2011).

[80] L. Zhang, V. Boyer, and M. O. Scully, Phys. Rev. A **105**, 023725 (2022).

[81] S. Choudhary and R. W. Boyd, in *Proceedings of the International School of Physics "Enrico Fermi", Course 190: Frontiers in Modern Optics* (IOS Press, Amsterdam; SIF, Bologna, 2016) pp. 31–76.

[82] N. A. Proite, *Atomic State Localization in Rubidium*, Ph.d. dissertation, University of Wisconsin–Madison (2011).

[83] M. Dabbicco, A. M. Fox, G. von Plessen, and J. F. Ryan, Physical Review B **53**, 4479 (1996).

[84] E. E. Dyer, D. W. Redding, and T. M. Blackburn, Nature Communications **12**, 1 (2021).

[85] R. W. Boyd, *Nonlinear Optics* (Academic Press, 2003) pp. 2,208.

[86] M. O. Scully, Phys. Rev. Lett. **67**, 1855 (1991).

[87] R. R. Alfano, P. L. Baldeck, P. P. Ho, and G. P. Agrawal, J. Opt. Soc. Am. B **6**, 824 (1989).

[88] I. Novikova, A. B. Matsko, V. A. Sautenkov, V. L. Velichansky, G. R. Welch, and M. O. Scully, Opt. Lett. **25**, 1651 (2000).

[89] D. J. Griffiths and D. F. Schroeter, *Introduction to quantum mechanics*, third edition ed. (Cambridge University Press, Cambridge ; New York, NY, 2018).

[90] I. Novikova, A. B. Matsko, V. A. Sautenkov, V. L. Velichansky, G. R. Welch, and M. O. Scully, Opt. Lett. **25**, 1651 (2000).

[91] D. A. Steck, "Rubidium 87 d line data," `https://steck.us/alkalidata/rubidium87numbers.1.6.pdf` (2003), revision 1.6, 14 October 2003.

[92] J. B. Clark, Z. Zhou, Q. Glorieux, A. M. Marino, and P. D. Lett, Opt. Express **20**, 17050 (2012).

[93] G. M. Gibson, S. D. Johnson, and M. J. Padgett, Optics Express **28**, 28190 (2020).

[94] E. Bolduc, N. Bent, E. Santamato, E. Karimi, and R. W. Boyd, Opt. Lett. **38**, 3546 (2013).

[95] S. Mansha, P. Moitra, X. Xu, T. W. W. Ma, R. M. Vullers, X. Liu, S.-Q. Li, R. Paniagua-Domínguez, and A. I. Kuznetsov, Light: Science & Applications **11**, 141 (2022).

[96] S. L. Cuozzo, P. J. Barge, N. Prajapati, N. Bhusal, H. Lee, L. Cohen, I. Novikova, and E. E. Mikhailov, Advanced Quantum Technologies **5**, 2100147 (2022), arXiv:2106.00785 .

[97] E. J. Candes and T. Tao, IEEE Transactions on Information Theory **52**, 5406 (2006).

[98] M. F. Duarte, M. A. Davenport, D. Takhar, J. N. Laska, T. Sun, K. F. Kelly, and R. G. Baraniuk, IEEE Signal Processing Magazine **25**, 83 (2008).

[99] D. Donoho, IEEE Transactions on Information Theory **52**, 1289 (2006).

[100] K. Lee and J. Ahn, Applied Physics Letters **97** (2010), 10.1063/1.3525583.

[101] H.-Y. Hou, Y.-N. Zhao, J.-C. Han, S.-W. Cui, D.-Z. Cao, H.-C. Liu, S.-H. Zhang, and B.-L. Liang, Opt. Express **29**, 41827 (2021).

[102] R. N. Lanning, Z. Xiao, M. Zhang, I. Novikova, E. E. Mikhailov, and J. P. Dowling, Phys. Rev. A **96**, 013830 (2017), arXiv:1702.01095 .

[103] T. Horrom, G. Romanov, I. Novikova, and E. E. Mikhailov, J. Mod. Opt. **60**, 43 (2013), arXiv:1204.3967 .

[104] T. Horrom, I. Novikova, and E. E. Mikhailov, J. Phys. B **45**, 124015 (2012), arXiv:1201.4372 .

[105] M. Zhang, R. N. Lanning, Z. Xiao, J. P. Dowling, I. Novikova, and E. E. Mikhailov, Phys. Rev. A **93**, 013853 (2016).

[106] M. Zhang, M. A. Guidry, R. N. Lanning, Z. Xiao, J. P. Dowling, I. Novikova, and E. E. Mikhailov, Phys. Rev. A **96**, 013835 (2017).